AN ABSTRACT OF THE DISSERTATION OF

Emily L. Shroyer for the degree of Doctor of Philosophy in Oceanography presented on September 10, 2009.

Title: Nonlinear Internal Waves on the Continental Shelf,

Abstract approved: _____

James N. Moum

The properties and evolution of nonlinear internal waves (NLIWs) depend upon the background conditions within which waves form, propagate, and dissipate. As a result, the NLIW field on the New Jersey shelf displayed dramatic variability during the Shallow Water 2006 experiment. Wave variability was exhibited by 1) amplitudes that ranged from 5 m to over 20 m, 2) irregular wave arrival times, and 3) wave forms that were either mode-1 or mode-2 in vertical structure. Over the month-long experiment, a six-day time span, which was coincident with the neap tide, was distinguished by having the largest observed NLIWs. The change in character of the observed waves between this period and the remainder of the month resulted in wave energies that increased by a factor of 5-10. The wave energy budget also varied spatially, as waves propagated across the shelf. On the outer shelf, energy was supplied to the NLIWs by the internal tide; and, inshore the balance shifted so that the change in energy per unit time was balanced by dissipative loss in the waves. While at a particular location dissipation in the core of the waves had only a weak dependence on energy, the average dissipative loss scaled with the maximum energy of the waves. NLIW dissipation was dominated by shear-driven turbulence in the mixed layer; at the pycnocline depth, NLIW dissipation was on average 10

times larger than that observed in background profiles. Consequently, the passage of NLIWs resulted in large heat fluxes across the pycnocline, contributing as much as 50% to the total average heat flux on the shelf. These changes in energetics were accompanied by structural changes in the wave form, including changes induced by wave interactions and the polarity reversal of three large-amplitude wave groups.

# Nonlinear Internal Waves on the Continental Shelf

by

Emily L. Shroyer

A DISSERTATION

submitted to

Oregon State University

in partial fulfillment of
the requirements for the
degree of

Doctor of Philosophy

Presented September 10, 2009
Commencement June 2010

Doctor of Philosophy dissertation of Emily L. Shroyer presented on September 10, 2009

APPROVED:

---

Major Professor, representing Oceanography

---

Dean of the College of Oceanic and Atmospheric Sciences

---

Dean of the Graduate School

I understand that my dissertation will become part of the permanent collection of Oregon State University libraries. My signature below authorizes release of my dissertation to any reader upon request.

---

Emily L. Shroyer, Author

# ACKNOWLEDGMENTS

This work would not have been possible without the support and encouragement of my advisor, James Moum. Throughout my time here, he has served as a mentor, teacher, and friend. He has shown me, by example, how to develop and thoughtfully pursue research questions, giving me the freedom to explore on my own, but at the same time providing the guidance needed to complete this project. I am also indebted to Jonathan Nash, my co-advisor, who provided a seemingly endless supply of optimism and faith in my abilities. He made himself easily accessible for scientific discussion and provided a sounding board for ideas and techniques, many of which have found their way into this manuscript. He has worked with me in the classroom, lab, and field; and, in each venue his excitement and support were contagious.

I thank my committee members: Jim, Jonathan, Murray Levine, Bill Smyth, and William Hetherington. I feel very fortunate to have worked with such exceptional scientists, all of whom practiced "open-door" policies and provided me with easy-access to their knowledge. Thank you each for your advice and suggestions. I recognize my office mate, Alexander (Sasha) Perlin, and the rest of the OSU Mixing Group: Mike Neeley-Brown, Ray Kreth, Levi Kiltcher, Sam Kelly and Toshi Kimura. Sasha has vastly improved my Matlab skills over the years; and my co-students, Levi, Sam, and Toshi, have been wonderful colleagues with whom to work and learn. This work would not have been possible without the expertise and technical support provided by Mike and Ray. This work was sponsored by the Office of Naval Research, and in particular I thank the project coordinators, Terri Paluszkiewicz and Linwood Vincent, for their support.

I wish to thank my friends and family for their patience and encouragement

throughout this endeavor– to Jeffrey Early for all the research breaks and providing a much needed distraction, and to my parents, brothers, and sister for their love, support, and help with juggling academia and family. I also thank my children, for keeping me grounded in reality and reminding me of what is truly important. Finally and most importantly, I would like to recognize and thank my husband, Kevin, without whom I could not have done this...

## CONTRIBUTION OF AUTHORS

Dr. James N. Moum and Dr. Jonathan D. Nash were involved with the writing and analysis of each manuscript.

TABLE OF CONTENTS

TABLE OF CONTENTS (Continued)

TABLE OF CONTENTS (Continued)

TABLE OF CONTENTS (Continued)

LIST OF FIGURES

LIST OF FIGURES (Continued)

LIST OF FIGURES (Continued)

LIST OF FIGURES (Continued)

LIST OF TABLES

# NONLINEAR INTERNAL WAVES ON THE CONTINENTAL SHELF

## 1 INTRODUCTION

The coastal ocean, the region inshore of the continental shelf break, acts as a boundary layer between near-shore water and the open ocean, controlling exchange of water masses and influencing large scale circulation. The inherent proximity of the coastal ocean to land makes the region of vital importance to mankind. We depend upon the coastal ocean for resources (such as fisheries and fossil fuels), transportation, recreation, and waste disposal. Furthermore, the coastal ocean is characterized by high biological productivity, and circulation on the shelf influences essential aspects of the marine ecosystem, from nutrient supply to larval transport. Understanding the physics controlling the circulation on the continental shelves is thus important to not only ourselves, but to the ecosystem as a whole. A recognized, prominent feature of circulation in the coastal ocean is the nonlinear internal wave (NLIW) field. The physics governing the waves and their influence on the coastal environment is the focus of this work.

NLIWs represent an important link in the cascade of energy from large-scale tidal motions to ocean mixing. High values of turbulent dissipation, seen along wave interfaces, can intensify nutrient and heat fluxes across the pycnocline, thereby affecting the local environment. In addition, large density perturbations induced by wave trains alter the propagation of acoustic waves; and at the same time, increased water velocities influence the sediment and biota, through suspension and

transport. So that these effects may be more fully understood and quantified, this thesis combines ship- and mooring-based data to explore the dynamics of NLIW formation, evolution, and decay on the New Jersey continental shelf.

## 1.1 Characteristics of NLIWs in the Ocean

Beneath the ocean's surface, internal waves displace density interfaces in a manner analogous to the surface gravity wave field. However, as a consequence of a reduced restoring force, internal waves have longer periods and larger amplitudes than their surface counterparts. When particle speeds approach the propagation speed of the waves, nonlinear dynamics become important, and advection terms in the equations of motion must be included. A simplified schematic of a single, surface-trapped nonlinear wave is shown in Fig. 1.1.

For this wave, horizontal velocities in the core of the wave above the pycnocline are in the direction of propagation, and a compensating flow occurs at depth beneath the pycnocline. Unlike a sinusoidal, linear wave, the horizontal, particle velocities at a given depth do not alternate direction; and instead, a strong convergent region near the leading edge of the wave results in a downward pulse followed by an upward pulse at the back of the wave that is associated with a near-surface divergence. While NLIWs result in only very small (a few cms) perturbations of the sea surface, the strong convergent and divergent regions modulate the capillary and small gravity wave field at the air-sea boundary, resulting in clear surface signatures that are easily identified in remote imagery (e.g., Jackson, 2004). This characteristic of NLIWs has led to the realization of the proliferation of these features in the coastal ocean and marginal seas.

The depression wave illustrated in Fig. 1.1 is not the sole form of NLIWs. Near-bottom, elevation waves also exist. For a quiescent fluid, depression waves

occur when the pycnocline is located closer to the surface than the bottom, and elevation waves occur when the pycnocline is located closer to the bottom. The descriptors "depression" and "elevation" refer to the direction of isopycnal displacements and imply a mode-1 structure, in which all isopycnals are displaced in the same direction. NLIWs are not limited to this type, as mode-2 waves have also been recorded. Furthermore, observations typically consist of multiple waves grouped together in packets, sometimes referred to as solibores (Henyey and Hoering, 1997).

### 1.1.1 Formation of NLIWs

Formation of NLIWs has been linked to the interaction of tidal flow with topography. Thus, in some regions like the South China Sea (SCS), wave packets appear semi-regularly at tidal intervals, at least during the summer months when the stratification supports the establishment of near-surface depression waves. For the SCS waves, the generation appears to be related to tidal flow within the Luzon Straight at the eastern edge of the basin (Ramp et al., 2004). However, details of formation are in general not well isolated, and may differ depending not only on geographic region but the local conditions. For example, in Massachusetts Bay wave packets evolve from the steep, internal tidal front of relatively light water that is formed over the crest of Stellwagen Bank on the edge of the bay (Scotti et al., 2007). This mechanism is similar to a lee wave formation scenario, such as that proposed in the Sulu Sea (Apel et al., 1985), but differs from resonant forcing caused by the interaction of a constant background flow and topography (e.g., Stastna and Peltier, 2005). While still related to tidal flow over topography, an independent formation mechanism was proposed by New and Pingree (1990, 1992), in which NLIWs in the Bay of Biscay formed locally at a region far away from the shelf ($> 100$ km) where an internal tidal beam intersected the surface layer. Several other mechanisms have been proposed, including some that are not dependent upon topographic forcing,

such as generation associated with intrusions (e.g. Maxworthy, 1980) and gravity currents (Nash and Moum, 2005).

The formation problem benefits greatly from application of theory and modeling, since resolving the details of generation from observational data alone is exceedingly difficult, especially when considering waves in open shelf environments. Despite this difficulty, some field studies have been able to clearly, if not conclusively, link wave formation to larger scale phenomena, and these observational studies can then be supplemented with numerical and theoretical efforts in order to understand the details of generation. For example, the observations of New and Pingree (1990) mentioned above were the motivation behind the work of Gerkema (2001) and Akylas et al. (2007), who used theory and modeling to investigate the dynamics governing formation by tidal beams intersecting the mixed layer. As another example consider again the SCS; Ramp et al. (2004) showed that the character and timing of the NLIW packets were closely related to the nature of the barotropic tide in the Luzon Strait. However, despite multiple, large-scale observational efforts, the specifics of formation are still debated (Zheng et al., 2007). In this case, further work is still needed to understand the subtleties of NLIW generation. On the open shelf, multiple generation sites, time-varying background fields, and remotely generated internal tides further complicate the study of wave generation. For example, irregularity of NLIW arrival times with respect to the barotropic tide does not in itself exclude tidal origins of the waves, but instead may be a manifestation of the complexity of the relationship between barotropic and baroclinic tides.

### 1.1.2 Evolution of NLIWs on the Continental Shelf

As NLIWs propagate across the shelf, they encounter variable conditions associated with the shoaling bottom, as well as spatial and temporal variability in background density and shear. The evolution associated with changes in the am-

bient conditions is of particular interest, as the nature of the topographic slopeand background fluid conditions affect how and where wave energy is dissipated. For simplicity, consider only the effect of the shoaling bottom. Assuming that the pycnocline remains level across the shelf, we would expect there to be a point where the fluid shifts from depression- to elevation-wave favorable as the depth of the water column shallows. Wave evolution through the so-called critical point can be dramatically different depending on the shelf slope (Helfrich and Melville, 1986; Vlasenko and Hutter, 2002; Grimshaw, 2002). The location of the critical point and the nature of wave transition through the critical point can be predicted using the first- and second-order coefficients of nonlinearity in the Korteweg-de Vries (KdV) equation, which is introduced in section 1.2.

If the critical point is approached rapidly, i.e., for steep slopes, the depression wave may undergo a kinematic instability and develop into an elevated core of trapped fluid (e.g., Bourgault et al., 2007). However, if the critical point is approached slowly, the leading depression wave evolves into a very long asymmetric depression wave followed by an oscillating tail. As the wave passes the critical point, the leading depression wave amplitude tends to zero, and elevation waves emerge from the tail (Liu et al., 1998; Orr and Mignerey, 2003; Duda et al., 2004). Two examples are shown in Fig. 1.2. The Oregon coast is characterized by a short shelf with a steep slope, in contrast the New Jersey coast is broad with a mild slope. Consequently, wave evolution, as documented by observational tracking experiments, varies between these two cases. On the Oregon shelf, the leading depression wave changed form only slightly between Fig. 1.2a and b. Inshore of the transect shown in Fig. 1.2b the wave signal was suddenly, and completely lost, a result that may possibly be attributed to breaking, and consequent rapid dissipation of all wave energy. On the New Jersey shelf, wave evolution occurred more gradually, and both the elongation of the lead wave and polarity reversal were captured (1.2c-e). The

evolution of the New Jersey waves are considered in detail in Chapter 4.

## 1.2 Theory and Modeling Efforts

Weakly nonlinear theory has often been employed to study the generation, evolution and shoaling of NLIWs. An essential feature of these theories is the use of asymptotic expansion in terms of small parameters, $a \sim \eta_0/H$ and $\epsilon \sim H^2/L^2$, which are scalings for nonlinearity and dispersion, respectively. In these expressions, $\eta_0$ is the amplitude, H is an appropriate vertical scale, and $L$ is a horizontal scale of the wave. By neglecting terms that are larger than a selected order of $\epsilon$, the dependence on the vertical coordinate is removed and the equation of motion simplified. One of the most commonly employed theories is the KdV equation that relies on a balance between nonlinearity and dispersion, i.e., $\epsilon \sim a$. The KdV equation governs the horizontal structure of internal gravity waves, and is valid for waves with small amplitude that are long compared to the total water depth. In terms of the NLIW displacement, $\eta$, the KdV equation may be written as

$$\frac{\partial \eta}{\partial t} + (c + \alpha\eta)\frac{\partial \eta}{\partial x} + \beta\frac{\partial^3 \eta}{\partial x^3} = 0. \tag{1.1}$$

Here, the constants, $\alpha$ and $\beta$, are the coefficients of nonlinearity and dispersion. Inclusion of a quadratic nonlinear term,

$$\alpha_1 \eta^2 \frac{\partial \eta}{\partial x},$$

on the left hand side of Eq. 2.1 results in the extended KdV (eKdV) equation. The linear wave speed, $c$, and vertical displacement function, $\phi$, of the solution are solved for in the eigenvalue problem defined by the hydrostatic, Taylor Goldstein

equation:

$$\Big\{\big[c-u(z)\big]^2\phi_z\Big\}_z + N^2(z)\phi = 0, \qquad (1.2)$$
$$\phi(0) = \phi(-H) = 0,$$

where subscripts indicate derivatives, $u(z)$ is the background velocity, and $N^2 = -g\rho_z/\rho_0$ is the buoyancy frequency. The fluid's background density profile is $\rho$, and the average density is $\rho_0$.

For internal waves, the coefficients, $\alpha$ and $\beta$, depend upon $c$ and $\phi$. In addition, $\alpha_1$ depends on a second-order correction to $\phi$. The explicit form of these parameters is reviewed in the appendix. Together Eq. 2.1 and 1.2 can be solved for the familiar soliton solution of the KdV equation,

$$\eta = \eta_0 \mathrm{sech}^2\Big(\frac{x-c't}{\lambda}\Big)\phi. \qquad (1.3)$$

The phase speed, $c' = c + \eta_0\alpha/3$, includes a nonlinear correction to the linear phase speed that is proportional to the amplitude. The solution requires the following relation between the amplitude and quarter-wavelength ($\lambda$):

$$\eta_0\lambda^2 = \frac{12\beta}{\alpha}.$$

Apart from solitons, cnoidal and dnoidal solutions to the KdV equation have also been used to study packets of nonlinear waves and solibores.

Other weakly nonlinear formulations include the Benjamin Ono equation, valid for small amplitude waves that are long compared to the upper layer but short compared to the lower layer, the Intermediate Long Wave Equation that describes waves with length scales comparable to the depth, and the Kadomtsev-Petviashvili (KP) equation, which relaxes the one-dimensionality of the KdV equation to include

weak diffraction in the transverse direction. The basic eKdV equation has also been modified to include rotation, shoaling, and dissipation, and as such mathematical descriptions of this type have proven useful in studying the evolution of waves through changing background conditions. For further reading on weakly nonlinear descriptions of internal gravity waves refer to Grimshaw (1981, 1985); Stepanyants (1989); Grimshaw et al. (2004); Helfrich and Melville (2006)

Many observations of NLIWs are outside the parameter regime where weakly nonlinear (particularly first order) theories are valid. Attempts to relax this constraint include efforts by Choi and Camassa (1999) who allowed for strong nonlinearity but weak dispersion in a two fluid system. Ostrovsky and Grue (2003) expanded on their work by including nonlinear dispersive effects. Furthermore, the Dubriel-Jacotin-Long (DJL) equation (Long, 1953) allows for fully nonlinear solutions of the Euler equations in a stratified fluid, and computational solutions to this equation have been developed by Davis and Acrivos (1967); Tung et al. (1982); Turkington et al. (1991). The method used by Turkington et al. (1991) calls for the minimization of $E(\eta)$ subject to a constraint on $F(\eta)$, where

$$\begin{aligned} E(\eta) &= \int_D \frac{1}{2}|\nabla\eta|^2\rho(z-\eta)dxdz, \text{ and} \\ F(\eta) &= \int_D \frac{1}{h}\left\{ \int_0^\eta \rho(z-\eta) - \rho(z-\zeta)d\zeta \right\} dxdz. \end{aligned} \tag{1.4}$$

The above expressions are integrated over the domain, $D$. The solution for the unknown displacement, $\eta$, depends upon the undisturbed background density, $\rho$, and the fluid depth, $h$. Note that $c^2E(\eta)$ is the kinetic energy and $ghF(\eta)$ is the available potential energy; hence, the variation principle minimizes the kinetic energy while constraining the potential energy (or amplitude). Stastna and Lamb (2002) generalized the computational method developed by Turkington et al. (1991) to include background shear. Depending on the background stratification and shear,

the numerical solution is amplitude-limited in one of three ways (Lamb, 2002). Amplitudes may be constrained by the conjugate flow limit, in which the wavelength increases without bound once a certain amplitude is obtained. Wave amplitudes may also be limited by the stability threshold, defined by the divergence of the wave solution and characterized by low Richardson numbers. And finally, if the wave particle speeds reach the wave propagation speeds, streamlines become vertical, the wave breaks, and trapped cores of recirculating fluid may develop.

Primary limitations of these fully nonlinear models include the inability to explicitly incorporate variable topography, the exclusion of viscosity, especially that associated with turbulent mixing, and the assumption of two-dimensionality. Fortunately, the increased numerical capabilities of recent years have allowed for the resolution necessary to effectively and efficiently model NLIWs using the full fluid equations with mixing parametrizations. Such models are often employed to study the formation (e.g., Hibiya, 1988; Scotti et al., 2007) and shoaling evolution (e.g., Lamb, 2002; Vlasenko and Hutter, 2002; Lamb, 2003) of nonlinear waves, although even for these examples fluid flows were assumed to be two-dimensional.

## 1.3 Shallow Water 2006 and the Nonlinear Internal Wave Initiative

In the summer of 2006, a large-scale, multi-institutional, multidisciplinary experiment was conducted off the New Jersey coast. This experiment, dubbed Shallow Water 2006 (SW06), was funded by the Office of Naval Research and had three primary research components: the Littoral Environmental Acoustics Research (LEAR), the Acoustics Wide Area Coverage for Surveillance (AWACS), and the NonLinear Internal Wave Initiative (NLIWI). At various times from mid-July to mid-September, measurements were acquired via multiple ship surveys, satellite and aerial surveys, 62 acoustic and environmental moorings, and ten gliders. The first

two components, LEAR and AWACS, were aimed at understanding acoustic propagation and scattering over variable terrain and through a dynamic background fluid. LEAR was additionally tasked with furthering our understanding of sediments and stratigraphy, and AWACS was designed to utilize autonomous vehicles to diagnose background conditions. It is the third component, the NLIWI, that is the primary concern of this thesis. And while the NLIW field has implications to acoustic propagation, making the pairing of the NLIWI with LEAR and AWACS ideal, this work concerns the physical nature of the waves.

In Chapter 2, properties of the background fluid (i.e., the wave guide) and a general description of the observed NLIWs are presented. Both fields varied considerably over the month-long experiment. A six-day time span from 17-22 August 2006 was notable due to the occurrence of much larger NLIWs, whose arrival times were more closely phased with the barotropic tide. This time period was coincident with a shift of stratification on the slope and the neap barotropic tide, although onshore baroclinic tidal energy flux increased by over an order of magnitude. In addition to characterizing the response of the wave field to background conditions, this chapter addresses certain aspects of wave formation, including the modulation of NLIWs by near-inertial shear. The impact that the NLIWs have on the coastal environment is quantified with estimates of wave-driven heat fluxes and particle transport. Over the month, NLIWs contributed as much as 50% to the vertical heat flux across the pycnocline. While the mass transport distance was moderate ($\sim$ 1 km) for most wave groups, one particular amplitude-limited, highly nonlinear wave group was capable of transporting mass in excess of 10 km across the shelf.

Chapter 3 presents mooring- and ship-based observations of mode-2 waves. The high-resolution provided by the ship's instrumentation allowed for a detailed examination of the structural evolution and energetics of one mode-2 wave group. Observations suggest that these higher-mode features are likely short-lived compared

to the mode-1 waves, as neither the ship-tracked wave group nor mooring-observed waves could be tracked large distances through the array. The mode-2 waves, which were energetically an order of magnitude smaller than the mode-1 waves, were associated with large values of turbulent mixing, suggesting that these waves may also play a significant role in the flux of heat and nutrients across the pycnocline. The decay in the ship-tracked wave group is attributed to both energy loss to turbulence as well as radiation of a short, mode-1 wave tail. Mooring records show that mode-2 waves were often associated with salinity intrusions, which could possibly play a role in wave formation; although the link is not certain.

In contrast to mode-2 wave groups, mode-1 wave groups were often followed in excess of 30 km across the shelf. The shoaling evolution of mode-1 NLIWs is detailed in Chapter 4; and, the polarity conversion of three large-amplitude wave groups is documented. In each case, a clear trend emerged despite diverse background conditions. As a symmetric lead wave approached the critical point, the leading edge accelerated, and an asymmetry developed. The front face of the leading wave continued to flatten as the wave propagated further inshore, while the trailing face remained steep. This trend continued until the front face was unidentifiable and a near-bottom elevation wave emerged. In spite of the highly nonlinear nature of the observed waves, the transition point, which is diagnosed by the observed wave vorticity, is accurately predicted by weakly nonlinear theory.

The structural changes displayed by the NLIWs were accompanied by shifts in energetics and turbulent mixing, and, the analysis of the wave energy budget is the focus of Chapter 5. The change in the character of the observed waves between the spring and neap tides resulted in NLIW energies that increased an order of magnitude. As wave groups shoaled, the energy balance shifted so that, on the outer shelf, energy was supplied to the NLIWs by the internal tide, while inshore dissipative loss to turbulence resulted in wave decay. At a specific location dissipation in

the core of the waves had only a weak dependence on the local energy. However, the average of dissipative loss over the decay region scaled with the maximum energy in the waves. A decay length scale of 35 km was estimated; this value is consistent with the observed wave decay. Also documented in Chapter 5 are rapid, short-term energy exchanges associated with wave interactions and topographic interaction, in which one wave group impinged upon a small topographic bump. The eventual outcome of these events was the loss of energy to extreme, turbulent mixing.

## Bibliography

Akylas, T. R., R. H. J. Grimshaw, S. R. Clarke, and A. Tabaei, 2007: Reflecting tidal wave beams and local generation of solitary waves in the ocean thermocline. *J. Fluid Mech.*, **593**, 297–313.

Apel, J. R., J. R. Holbrook, A. K. Liu, and J. J. Tsai, 1985: The Sulu Sea Internal Soliton Experiment. *J. Phys. Ocean.*, **15**, 1625–1651.

Bourgault, D., M. D. Blokhina, R. Mirshak, and D. E. Kelley, 2007: Evolution of a shoaling internal solitary wavetrain. *Geophys. Res. Let.*, **34**, 3601–+.

Choi, W. and R. Camassa, 1999: Fully nonlinear internal waves in a two-fluid system. *J. Fluid Mech.*, **396**, 1–36.

Davis, R. E. and A. Acrivos, 1967: Solitary internal waves in deep water. *J. Fluid Mech.*, **29**, 593–607.

Duda, T. F., J. F. Lynch, J. D. Irish, R. C. Beardsley, S. R. Ramp, C.-S. Chiu, T. Y. Tang, and Y.-J. Yang, 2004: Internal tide and nonlinear internal wave behavior at the continental slope in the northern South China Sea. *IEEE J. Oceanic Engin.*, **29 (4)**, 1105–1130.

Farmer, D. M. and J. D. Smith, 1980: Tidal interaction of stratified flow with a sill in Knight Inlet. *Deep Sea Res.*, **27A**, 239–254.

Gerkema, T., 2001: Internal and interfacial tides: Beam scattering and local generation of solitary waves. *J. Marine Res.*, **59**, 227–255.

Grimshaw, R., 1981: A second-order theory for solitary waves in deep fluids. *Phys. Fluids*, **24 (9)**, 1611–1618.

Grimshaw, R., 1985: Evolution equations for weakly nonlinear, long internal waves in a rotating fluid. *Studies in Applied Mathematics*, **73**, 1–33.

Grimshaw, R., 2002: *Environmental Stratified Flows, Internal Solitary Waves*, Topics in Environmental Fluid Mechanics, Vol. 3. Springer US, 1–27 pp., doi: 10.1007/b100815.

Grimshaw, R., E. Pelinovsky, T. Talipova, and A. Kurkin, 2004: Simulation of the transformation of internal solitary waves on oceanic shelves. *J. Phys. Ocean.*, **34**, 2774–2791.

Helfrich, K. R. and W. K. Melville, 1986: On long nonlinear internal waves over slope-shelf topography. *J. Fluid Mech.*, **167**, 285–308.

Helfrich, K. R. and W. K. Melville, 2006: Long nonlinear internal waves. *Annual Rev. Fluid Mech.*, **38**, 395–425.

Henyey, F. S. and A. Hoering, 1997: Energetics of bore-like internal waves. *J. Geophys. Res.*, **102 (C2)**, 3323–3330.

Hibiya, T., 1988: The generation of internal waves by tidal flow over Stellwagen Bank. *J. Geophys. Res.*, **93**, 533–542.

Jackson, C. R., 2004: *An Atlas of Internal Solitary-like Waves and their Properties.* 2d ed., Global Ocean Associates, www.internalwaveatlas.com.

Lamb, K. G., 2002: A numerical investigation of solitary internal waves with trapped cores form via shoaling. *J. Fluid Mech.*, **451**, 109–144.

Lamb, K. G., 2003: Shoaling solitary internal waves: on a criterion for the formation of waves with trapped cores. *J. Fluid Mech.*, **478**, 81–100.

Liu, A. K., Y. S. Chang, M.-K. Hsu, and N. K. Liang, 1998: Evolution of nonlinear internal waves in the East and South China Seas. *J. Geophys. Res.*, **103 (C4)**, 7995–8008.

Long, R. R., 1953: Some aspects of the flow of stratified fluids: I. A theoretical investigation. *Tellus*, **5**, 42–58.

Maxworthy, T., 1980: On the formation of nonlinear internal waves from the gravitational collapse of mixed regions in two and three dimensions. *J. Fluid Mech.*, **96 (1)**, 47–64.

Nash, J. D. and J. N. Moum, 2005: River plumes as a source of large-amplitude internal waves in the coastal ocean. *Nature*, **437**, 400–403.

New, A. L. and R. D. Pingree, 1990: Large-amplitude internal soliton packets in the central Bay of Biscay. *Deep Sea Res.*, **37**, 513–524.

New, A. L. and R. D. Pingree, 1992: Local generation of internal soliton packets in the central Bay of Biscay. *Deep Sea Res.*, **39**, 1521–1534.

Orr, M. H. and P. C. Mignerey, 2003: Nonlinear internal waves in the South China Sea: Observation of the conversion of depression internal waves to elevation waves. *J. Geophys. Res.*, **108**, 3064–3079, doi:10.1029/2001JC001163.

Ostrovsky, L. A. and J. Grue, 2003: Evolution equations for strongly nonlinear internal waves. *Phys. Fluids*, **15 (10)**, 2934–2948.

Ramp, S. R., et al., 2004: Internal solitons in the northern South China Sea Part I: sources and deep water propagation. *IEEE J. Oceanic Engin.*, **29 (4)**, 1157–1181.

Scotti, A., R. Beardsley, and B. Butman, 2007: Generation and propagation of nonlinear internal waves in Massachusetts Bay. *J. Geophys. Res.*, **112 (C10001)**, doi:10.1029/2007JC004313.

Stastna, M. and K. Lamb, 2002: Large fully nonlinear internal solitary waves: The effect of background current. *Phys. Fluids*, **14 (9)**, 2987–2999.

Stastna, M. and W. Peltier, 2005: On the resonant generation of large-amplitude internal solitary waves and solitary-like waves. *J. Fluid Mech.*, **543**, 267–292.

Stepanyants, L. A. O. Y. A., 1989: Do internal solitons exist in the ocean? *Reviews of Geophysics*, **27**, 293–310.

Tung, K.-K., T. F. Chan, and T. Kubota, 1982: Large amplitude internal waves of permanent form. *Studies in Applied Mathematics*, **66**, 1–44.

Turkington, B., A. Eydeland, and S. Wang, 1991: A computational method for solitary internal waves in a continuously stratified fluid. *Studies in Applied Mathematics*, **85**, 93–127.

Vlasenko, V. and K. Hutter, 2002: Numerical experiments on the breaking of solitary internal waves over a slope-shelf topography. *J. Phys. Ocean.*, **32**, 1779–1793.

Zheng, Q., R. D. Susanto, C.-R. Ho, Y. T. Song, and Q. Xu, 2007: Statistical and dynamical analyses of generation mechanisms of solitary internal waves in the northern South China Sea. *J. Geophys. Res.*, **112**, 3021–+, doi:10.1029/2006JC003551.

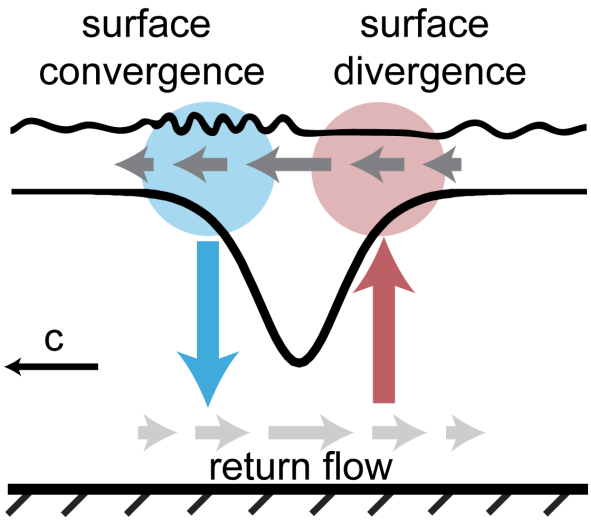


FIGURE 1.1: Schematic of a surface trapped nonlinear internal wave of depression. The wave is propagating to the left. The region of near-surface convergence at the leading edge of the NLIW enhances the enhances capillary and small gravity waves, and the opposite is true in the region of divergence at the back edge of the wave.

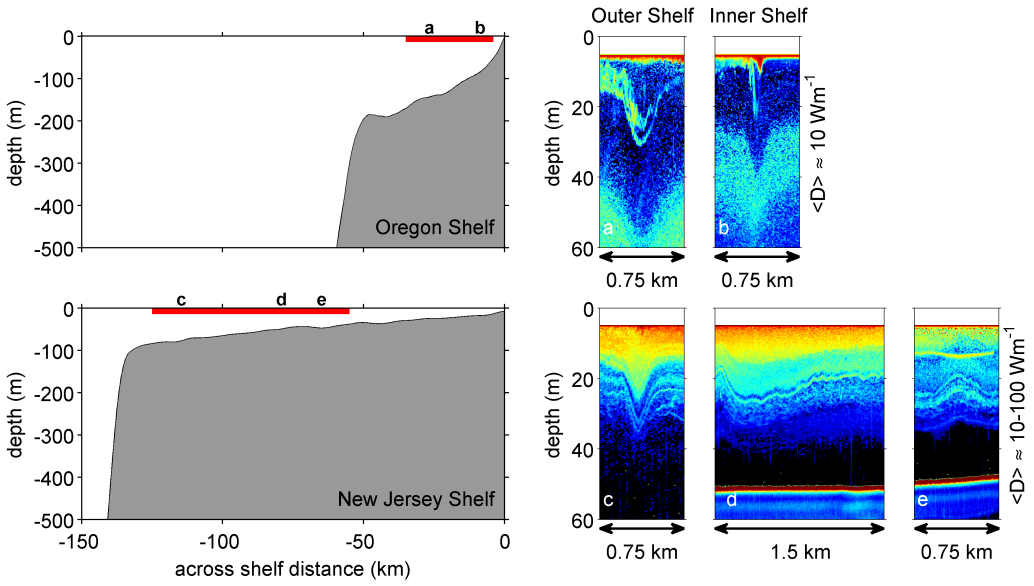


FIGURE 1.2: Evolution of NLIWs on the shelf. Top: Topographic section off the Oregon coast. Bottom: Topographic section off the New Jersey coast. Lettered panels show acoustic backscatter sections capturing lead wave evolution.

# 2 A DESCRIPTIVE ANALYSIS OF THE NONLINEAR INTERNAL WAVE FIELD OFF THE NEW JERSEY COAST

Emily L. Shroyer, James N. Moum, Jonathan D. Nash

## Abstract

The wave climate, properties, and variability of the nonlinear internal wave (NLIW) field on the New Jersey shelf are characterized using ship and mooring data collected during the Shallow Water 2006 Experiment. Background conditions were influenced by mesoscale shifts in stratification at the shelf break and an energetic shear environment across the shelf, particularly in the inertial band. Changes in the wave guide and forcing at the shelf break resulted in two distinct periods of NLIWs with markedly different wave amplitude. NLIWs of depression observed during the first period had typical displacements near 8 m, while waves in the second period were typically twice as large. Over most of the month, wave arrival times at moorings were irregular, and often more than one packet was observed per (M2) tidal period. However, from 17–21 August, NLIW arrival times were phase-locked to the barotropic tide. During this time, destructive/constructive modulation of the M2 internal tide by the inertial wave field at the shelf break corresponded to stronger/weaker NLIWs on the shelf. Vertical heat flux attributed to the waves was dominated by short, extreme mixing events; however, the NLIW contribution to the heat flux accounted for as much as 50% of the August 2006 time average. Particle transport distances were estimated for the ship-tracked waves. In general, particle transport distances by the waves were a few 100 meters; however, one wave group, which was amplitude-limited, transported mass several kilometers over a few hours.


## 2.1 Introduction

Nonlinear internal waves (NLIWs) have been documented throughout the world's coastal regions (Jackson, 2004). A majority of these sightings are captured by satellite based imagery, as near-surface depression waves often manifest a clear

surface signature of alternating bands of rough and smooth water (e.g., Apel et al., 1975; Alpers, 1985; Gasparovic et al., 1988; Liu et al., 1998). In some regions, intensive in-situ studies have further explored the physics of NLIWs and their impacts on the coastal environment. These endeavors have included both individual, small-scale studies in addition to large, multi-institutional, collaborative efforts. Due to the inherent variability of tidal forcing, mesoscale oceanic conditions, and the topography of individual geographic regions, NLIW fields may differ significantly from one another. In order to provide a global context to the observations presented here that were collected as part of the Office of Naval Research's NonLinear Internal Wave Initiative/Shallow Water '06 Experiment (NLIWI/SW06) on the New Jersey coast, we offer a brief, but by no means exhaustive, review of past experimental efforts.

Several studies have concentrated on marginal seas and other coastal regions that are partially isolated from the open ocean. For example, early efforts by Perry and Schimke (1965) in the Andaman Sea revealed the presence of 80-m amplitude waves in depths of approximately 1500 m. Osborne and Burch (1980) linked the generation of these waves to tidal interaction with topography to the west, near the Andaman and Nicobar Islands. In the western Pacific, the Sulu Sea was singled out as the location for a large-scale internal wave study in May 1980. The Sulu Sea Soliton experiment helped to characterize the nature of the NLIWs, which had amplitudes of 90m, wavelengths greater than 10 km, and wave speeds over 2 m $s^{-1}$. The generation of the waves was traced to a shallow sill at the southern end of the sea to the east of Borneo (Apel et al., 1985). The nearby South China Sea has also been the focus of several large-scale, collaborative studies. For example, the ASIAEX experiment (2000/2001) was designed to explore the evolution of very large ($>$ 100m) amplitude waves and their effect on acoustic propagation (e.g., Orr and Mignerey, 2003; Duda et al., 2004; Liu et al., 2004; Ramp et al., 2004).

In addition, as a follow up to ASIAEX, a portion of the NLIWI was devoted to understanding mesoscale influences on the formation and evolution of NLIWs in the South China Sea. Although smaller in scale, multiple data sets from Knight Inlet, British Columbia (Farmer and Armi, 1999) and Massachusetts Bay (Haury et al., 1979; Chereskin, 1983; Scotti et al., 2007), which are both isolated from the open ocean, have helped clarify generation mechanisms related to barotropic tidal interaction with topographic features.

While the details may differ, in all cases the generation of waves in these partially-enclosed regions is linked to tidal interaction with topographic sills or banks along their borders. Consequently waves in these regions are often phased with the barotropic tide, allowing for semi-accurate predictions of arrival times at a given location. Similarly, the formation of waves in open shelf areas are also often attributed to either barotropic or baroclinic tidal interaction with the shelf break. However, observations have shown that the arrival times of these open-shelf waves are not necessarily phase-locked with the barotropic tidal cycle (e.g., Jeans and Sherwin, 2001; Moum et al., 2007a; Moum and Nash, 2008). Differences in arrival times of waves in relation to the tide may be a consequence of multiple generation sites, subtidal changes in stratification, or advection by tidal, wind, and mesoscale currents. Complicating matters further is the fact that NLIWs on continental shelves may be attributed to either the locally generated internal tide, a remotely generated internal tide, or some combination of the two. A noteworthy exception to tidally generated nonlinear waves on shelves is described by Nash and Moum (2005). In that case, NLIWs are released as the tidally pulsed Columbia River plume decelerates to a subcritical state. Other examples of continental shelf studies are described below.

During the summers of 1995–1996, the Natural Environment Research Council conducted the Shelf Edge Study and Acoustic Measuring Experiment (SESAME) on the Malin Shelf off the coast of Scotland, a region noted for significant energy

loss from the barotropic tide (Egbert and Ray, 2000). From mooring and ship-based data collected during SESAME, Small et al. (1999) and Small (2003) describe the formation of a NLIW packet from a shoreward-propagating, remotely generated tidal bore. The amplitudes and number of waves in the packet increased across the slope region; once the shelf was reached, growth slowed and decay began. Inall et al. (2000) estimated that as much as 70% of the dissipative loss in these NLIWs occurred in the bottom boundary layer; and, as with the data presented here, the NLIWs were more energetic during the neap tidal period. In the western Atlantic on the Scotian Shelf, Sandstrom and Elliott (1984) used results from a multi-year study to estimate energy dissipation in NLIWs. Their analysis showed that elevated dissipation levels due to NLIWs were sufficient to provide enough nutrients (via turbulent mixing) to sustain the observed biological productivity in the region.

On New England's continental shelf, a highly variable nonlinear wave field was documented during the Shelf Break Primer study (Colosi et al., 2001). During this study, the steepening of the internal tide and consequent solibore formation was weakly correlated to the cross-axis, shelf-break jet velocity (i.e., the component parallel to the direction of wave propagation), so that when the jet consisted of an offshore component, steepening of the internal tide increased. In the same region, the Synthetic-Aperture Radar Internal Wave Signature Experiment (SARSEX) was conducted in the New York Bight in 1984. SAR imagery and in-situ observations were combined to investigate the interaction between the internal waves and surface waves in order to better understand the surface manifestations of NLIWs; the study found reasonable agreement between theoretical models and imaging when using weakly-nonlinear wave theory (Gasparovic et al., 1988). In 1995 on the western coast of the United States, the Coastal Ocean Probing Experiment (COPE) gathered measurements that were also aimed at exploring details of the response of radiation backscatter to NLIWs (Kropfli and Clifford, 1996). Stanton and Ostrovsky (1998)

show that during this time period second-order KdV theory captures the observed amplitude and wavelength of the NLIWs.

The current experiment, NLIWI/SW06, was conducted in the same region as the Shallow-Water Acoustics in Random Media Experiment (SWARM, 1995), southward of the study sites for the Shelf Break Primer Study and SARSEX. SW06 expanded the scope of SWARM by increasing the density of observations and extending the duration of measurements (Apel et al., 1997; Tang et al., 2007). Both experiments were designed with the intent of examining the effects of NLIW activity on acoustic propagation. However, SW06 benefited from detailed knowledge of the acoustical properties of the bottom topography, increased observational effort, and more refined instrumentation. As part of this experiment, a shipboard survey of NLIW activity was performed onboard the *R/V Oceanus* during August 2006. The observed waves were primarily mode-1 depression waves propagating shoreward. Departures from this norm included the transition to elevation waves in three different wave groups that were tracked far inshore (Shroyer et al., 2009d), as well as observations of mode-2 NLIWs (Shroyer et al., 2009b) and wave groups that propagated parallel to the shoreline. Other phenomena of interest include observations of wave interactions and large mixing events likely associated with shear instabilities (Shroyer et al., 2009a).

Here we present a description of the general properties of these waves and characterize the background fluid state that controlled wave shoaling. We address impacts of the waves on the broader coastal environment by estimating vertical heat flux and particle transport attributed to the waves. As far as we are aware, this is the first time that field measurements allow for direct estimates of NLIW-driven vertical heat flux across the shelf. This work is organized as follows. We begin by offering a brief description of the relevant experimental details (section 2.2). In sections 2.3 and 2.4 general properties of the background environment and observed

nonlinear waves are discussed. Aspects of NLIW formation are discussed in section 2.5. In section 2.6, we turn our attention to the effects of the NLIWs on the coastal region and present estimates of wave heat flux and particle transport. A summary is given in section 2.7.

## 2.2 Experimental Details

The SW06 site and bathymetry are shown in Fig. 3.1. The grey cloud indicates transects made by the *R/V Oceanus* as we tracked NLIWs. The ship was equipped with a 120 kHz echosounder, a side-mounted 1200 kHz ADCP, and a hull-mounted 300 kHz ADCP. Shipboard acoustics, X-band radar, and visual sightings were used to locate and track shoreward propagating wave groups perpendicular to fronts. Wave groups were transited through at 3–4 m $s^{-1}$ from the back to leading wave, here the ship was turned and held stationary as microstructure measurements were collected using the Chameleon profiler (Moum et al., 1995). After profiling through the leading few waves of a train, the process was repeated. Observations of 27 different ship-tracked wave packets were collected in this manner over the month of August.

While the majority of observations reported in this manuscript were obtained onboard the vessel, we also present data from 10 across-shelf, environmental moorings (SW 29, 30, 34, 37, 38, 40, 41, 42, 43, 47) that were located along the main wave transect path (Fig. 3.1, blue diamonds). These particular moorings were selected for use in this work because they offered significant water column coverage of either density or velocity measurements. The moorings were of two types: water column and bottom landers; instrumentation on these moorings is summarized in Table 2.1. Note that in subsequent figures all across-shelf distances are defined according to the axis shown in Fig. 3.1, with the origin located at the mooring array intersection

and offshore velocities being positive.

## 2.3 Background Conditions

Historically, shelf water in the Mid Atlantic Bight has origins extending from the Scotian Shelf and local river input (Chapman et al., 1986). In the winter, this relatively cool, fresh water is further cooled at the surface and then mixed by tides and storms into a near-homogeneous "pool" on the shelf. In contrast, slope water is warm and salty, resulting in the establishment of a shelf-break front and a equatorward jet with mean transport of approximately 0.2 Sv off the New Jersey coast (Linder and Gawarkiewicz, 1998). Summer heating and fresh-water runoff often obscure the surface signature of the front; however, temperature-salinity sections reveal the remnant of the cold "pool" at depth beneath the seasonal, stratified mixed layer (Fratantoni et al., 2001; Linder and Gawarkiewicz, 1998). The presence of the front forms a natural barrier of mass and heat exchange between the shelf and slope water. At the same time, other processes associated with the front (e.g., frontal intrusions, double diffusion and cabeling) enhance mixing of these two water masses (Houghton and Marra, 1983). Additionally, mesoscale variability associated with the front and jet may have a profound effect on the generation of the local internal tide, its subsequent steepening, and release of nonlinear internal waves. Below we document the sub-inertial and tidal circulation recorded during the SW06 experiment.

### 2.3.1 Sub-Inertial Circulation

Winds were light during the first part of the experiment (1–11 August 2006). Afterward, winds were directed toward the southwest for approximately five days; this period was followed by northeastward winds through the remainder of the month

(Fig. 2.2a). The shipboard tracking experiment began during the neap tide and continued through the following spring and neap tidal cycles (Fig. 2.2b). The average mooring temperature field interpolated across the shelf (Fig. 2.2c) reveals the subsurface signature of the shelf-break front, highlighted by the 12.5°C isotherm. The region is characterized by strong barotropic tidal velocities ($\sim 0.1$m s$^{-1}$, Moody and Butman (1984)), and therefore, velocity data were detided before averaging for the purpose of evaluating the larger scale flow. Month-long mean currents were primarily alongshore in a southward direction with estimated transport around 0.3 Sv (Fig. 2.2d); hence, the dominant component of the mean mesoscale coastal circulation is perpendicular to onshore wave propagation. Mooring temperature, salinity, and density data at the slope were averaged over three different time periods (vertical dotted lines Fig. 2.2 a-b) qualitatively chosen by the character of the barotropic tide and observed internal wave properties (discussed in Section 2.4). Each time period displayed a character change in the slope water, as the sub-surface cool, fresh shelf water was shifted farther offshore during downwelling winds, and warm, salty slope water moved farther onshore with the onset of upwelling (Fig. 2.2e-g).

The regime shift is also apparent in the temperature structure at both the offshore and inshore mooring (Fig. 2.3a-b). At the offshore mooring, colder water was observed at the uppermost thermistor (20 m depth) after 11 August 2006 as the shelf-break front presumably moved offshore. The temperature increased after 15 August 2006, corresponding to the onset of upwelling winds. Furthermore, the temperature inversion at $\sim 75$ m that was present intermittently during the first half of the record did not appear between 15–25 August 2006. The nature of the internal tide at the inshore mooring changed at approximately these sames times, perhaps in response to offshore, mesoscale stratification. In particular, tidal displacements of isotherms, and the power in the M2 tidal band, from 9–15 August 2006 were

much smaller than those observed at other times (Fig. 2.3c). The increased power at frequencies near $10^{-3}\mathrm{s}^{-1}$ after 16 August 2006 was a consequence of an increase in energy in the higher frequency NLIWs; during this time, a peak in the M4 tidal harmonic existed. The effect of these background conditions on the internal tide is considered by Nash et al. (2009).

### 2.3.2 Inertial and Tidal Circulation

Harmonic analysis was used to characterize inertial and tidal motions across the shelf. While these frequencies are greater than those discussed in the previous section, the associated time scales are long compared to those of the NLIWs. Thus these motions influence wave propagation through modulation of the background fluid fields. Velocity time series were first averaged into 30-minute bins, and then time series were decomposed at each depth using

$$u(t) = u_0 + \sum_{i=1}^{3} a_i \cos(2\pi f_i t) + b_i \sin(2\pi f_i t) + u_r,$$

where $f_{1-3}$ were comprised of M2, K1 and near-inertial frequencies. The coefficients $a_i$ and $b_i$ were solved for by minimizing the variance of the velocity residual, $u_r$, via least-squares analysis. The above expression was applied over a three-day-running interval shifted temporally every half an hour. Overlapping bins were averaged together. Barotropic components were assumed to be equivalent to depth-averaged quantities (Kelly et al., 2009), and baroclinic fields (Fig. 2.4) were calculated by subtracting the depth mean. NLIW packets undoubtedly have some effect on the harmonic decomposition; however, due to the sporadic arrival times at a particular mooring, the wave influence may not be as severe as might be expected in other regions such as the South China Sea (Duda et al., 2004).

The M2 barotropic tidal ellipses are oriented across isobaths with magnitudes

near 10 cm $s^{-1}$ on the shelf (Fig. 2.4b). Both the magnitudes and directions agree well with historic data (Moody and Butman, 1984) and fits from the TPXO tidal model (Egbert et al., 1994). The ratio of the across-shelf (major) to along-shelf (minor) amplitude of the shelf moorings is approximately 1.6; SW43 has a larger ratio of 2.2. The orientation and phase of K1 ellipses vary between the slope and the shelf. Similar to M2, K1 barotropic tidal ellipses on the slope are directed across-isobath. For these moorings, K1 amplitudes are small at less than 1 cm $s^{-1}$. On the shelf, K1 ellipses are oriented primarily in the along-isobath direction with amplitudes on the order of 5 cm $s^{-1}$ (Fig. 2.4c). On the shelf, the ratio of along-shelf (major) to across-shelf (minor) amplitude of the K1 component is on average 1.7.

The vertical structure of internal motions was diagnosed using empirical orthogonal functions (E.O.F.s), which were computed for $u_f$, $u_{K1}$, and $u_{M2}$ (shown in Fig. 2.4c-e). On the shelf, the baroclinic K1, M2, and inertial across-shelf velocity components are mode-1 in vertical structure (Fig. 2.4b-d, Fig. 2.5a), each with zero crossing near 30-m depth (between 0.35–0.40$H$). The first E.O.F. contains a majority of the total variance for each of these frequencies. On the slope, 80% of the total variance of the K1 component is equally spread over the first four modes, and the first E.O.F. is therefore not shown in Fig. 2.5b. The M2 baroclinic tide is primarily mode-1 at SW43 with 74% of the variance contained in the first E.O.F.; the zero crossing at this slope mooring is located near 180 m (0.38$H$). The baroclinic inertial input is relatively constant across the slope and shelf in the upper 60 m of the water column (Fig. 2.4d). While on the slope the vertical structure of the first E.O.F. has multiple zero-crossings; the sole crossing above 150 m occurs near 30 m (.07$H$; Fig. 2.5b).

The depth-averaged baroclinic kinetic energy ($KE$) in these three frequency bands varied across the shelf and slope, as well as over time (Fig. 2.5c-d). At the

shelf mooring (SW37), the $KE$ in the K1 component remained relatively constant over time. The inertial $KE$ began to increase with the onset of downwelling winds and continued to rise over the rest of the month; at its peak value the inertial $KE$ was more than 10 times the M2 energy. From 6–11 August, the energies in all three components were weak and near the same magnitude. The increase in the M2 component, apparent around 18 August, coincided with the arrival of larger-amplitude NLIWs but was not directly proportional to the barotropic forcing (Fig. 2.2b). In contrast to shelf conditions, the M2 energy at the slope mooring always exceeded the inertial and K1 components. A maximum of the M2 kinetic energy occurred near 11 August, in phase with the barotropic forcing, which was 2 (5) times greater than inertial (K1) energy.

Summarizing the above in a context relevant to the NLIWs, we recognize that during this experiment inertial waves and the M2 baroclinic tide were primary contributors to motions across the shelf. The internal tide was highly irregular with considerable energy spread across semidiurnal harmonics (Fig. 2.3). A significant amount of energy associated with these higher frequency motions, nonlinear effects as well as other possible contributors, is not accounted for in the harmonic fit and remains in the velocity residual (Fig. 2.4g). The variability of these internal motions undoubtedly contributed to the sporadic nature of wave arrivals at a given location (section 2.4).

### 2.3.3 Properties of the Wave Guide

The effect of the background density and velocity structure to NLIW evolution may be quantified using the coefficients of the extended Korteweg-de Vries (eKdV) equation,

$$\frac{\partial \eta}{\partial t} + (c_0 + \alpha\eta + \alpha_1\eta^2)\frac{\partial \eta}{\partial x} + \beta\frac{\partial^3 \eta}{\partial x^3} = 0. \tag{2.1}$$

Fig. 2.6a-d shows the coefficients governing dispersion ($\beta$), second-order nonlinearity ($\alpha_1$), first-order nonlinearity ($\alpha$), and linear long wave speeds ($c_0$) for all ship-tracked waves. These parameters depend on the background velocity, the linear vertical structure function, and the second-order correction to the vertical structure function. We do not define the values explicitly here; for a complete discussion on the eKdV equation, we refer to Grimshaw et al. (2004). The reader will note that our Fig. 2.6 is essentially a reproduction of their Figs. 3, 7, and 11. All values were computed using background estimates of local density and shear for ship-based observations. Background density profiles, $\sigma_0(z)$, were calculated using an average of profiles taken ahead of the waves (typically 2). Background velocity profiles, $u_0(z)$, were calculated by averaging approximately 5–10 minutes of data ahead of the wave; the exact value differed depending on the length of time between ship positioning and wave arrival. Both $\sigma_0$ and $u_0$ are low-pass filtered at 0.15 $\mathrm{m}^{-1}$ in the vertical.

The magnitude of the dispersive term decreases as the bottom depth shoals, while at the same time the magnitude of $\alpha_1$ steadily increases, so that in shallow water higher-order nonlinear effects are more important. Without background shear (dark grey diamonds), almost all values of $\alpha_1$ are less than zero. Inclusion of background shear yields some values of $\alpha_1$ on the outer shelf that are greater than zero, although the calculation of $\alpha_1$ is sensitive to the background shear and these values may be a consequence of the numerical calculation and the smoothness of $u_0$. Inshore were localized regions where $\alpha$ was greater than zero, corresponding to times when elevation waves were observed (Shroyer et al., 2009d). The background shear in these locations served to "push" the system towards a more elevation-friendly environment. Note that there is not an obvious dependence of the sign of $\alpha$ on the across-shelf distance; this spread is indicative of the large variability observed in background stratification and shear for each wave group. The range apparent in

the linear long wave speed (Fig. 2.6c) further illustrates the diverse climate of the background velocity field. Small-scale, localized effects have strong control; as an example, the offshoot of low $c_0$ at -42 km is associated with one wave group that encountered a topographic bump (Fig. 2.6e). While the resulting wave dynamics is the focus of a separate analysis (Shroyer et al., 2009a), examination of $\alpha_1$ and $\beta$ reveals the increased importance of higher-order nonlinearity and the diminished effect of dispersion for this wave group.

## 2.4 Wave Properties

Observed displacement amplitudes ($A$) of ship-tracked waves ranged from -24 m to 10 m with a mean magnitude of 8 m (Fig. 2.7a). $A$ is defined by the maximum isopycnal displacement and is positive/negative for elevation/depression waves. For the remainder of this manuscript the term amplitude will be used when referring to the magnitude of $A$, and displacement will refer to both the sign and magnitude of $A$. The half-width ($\lambda_{1/2}$), defined as the distance over which the amplitude decreased by half, ranged from a minimum of 80 m to over 900 m with a mean value of 230 m (Fig. 2.7b). The mean value of the average wave speeds ($c$), calculated by differencing time and position, was approximately 0.78 m $s^{-1}$ (Fig. 2.7c). All but one of the ship-tracked wave groups propagated shoreward (300° clockwise from North), the exception propagated parallel to the shoreline at 90° clockwise of other waves (Fig. 2.7d). While Fig. 2.7d was computed from shipboard data, measurements at SW30 give a similar result (not shown) with mean orientation at 310° (computed by minimizing across-axis velocity component). Mooring data from SW30 (0 km) were used to compute Fig. 2.7e-f. Wave arrival times at SW30 were not correlated with the local, barotropic tidal height (Fig. 2.7e), with both large and small waves (defined using the maximum, vertically integrated energy

flux) arriving at various stages of the barotropic tide (Fig. 2.7f).

For bookkeeping purposes, ship-tracked waves were named following the convention used for tropical storms. Fig. 2.8c gives the names of the various wave groups and their arrival time at SW30 (39°0′N, 73°1′W, 0 km), along with the arrival times of other mooring-observed NLIWs (closed markers). Ship-tracked wave groups were identified by using the sighting nearest SW30 and the average wave speed to project the wave arrival at the mooring either forward or backward in time. Six ship-tracked wave groups do not appear in the SW30 mooring record; however, these waves are included in Fig. 2.8 (open markers) using the projected arrival time. As mentioned, wave arrivals were not phase-locked with the barotropic M2 tide; the spread in arrival times hints at a complicated formation story. The period from the 17–21 August is notable in that wave arrival times are more closely correlated with the onshore, barotropic M2 tidal current at SW40.

For most wave groups the maximum amplitude was close to the mean value of $|A|$ near 8 m, with a clear departure from this trend during the period between 1800 UTC 17 August 2006 and 0000 UTC 22 August 2006 (Fig. 2.8). In this time range, waves *Rosey*, *Sonny*, *Tonya*, and *Wyatt* had displacements in excess of -15 m. Surprisingly, these larger amplitude waves were not associated with the spring tide, which has been linked to larger internal waves in other studies (e.g., New and Pingree, 1990; Ramp et al., 2004; Scotti et al., 2007). However, the period of larger-amplitude NLIWs coincided with the change in stratification at the shelf break (Fig. 2.2f), an increase in internal tide energy onto the shelf (Nash et al., 2009), and the period of near-uniform NLIW arrival times (Fig. 2.8c).

Average wave speeds are shown in Figs. 2.7c and 2.8b; in reality wave speeds were not constant and were clearly modulated by the background velocity. For wave groups that were tracked large distances across the shelf (in excess of 30 km), there exists a significant correlation (not shown) between changes in the phase speed,

$\Delta c$, and the across-shelf, barotropic velocity; on average, there existed a one-to-one relationship between $\Delta c$ and the barotropic velocity. In addition to simple advection, the baroclinic velocity field may influence other aspects of the waves, from the half-width length to the nature of the limiting amplitude (Stastna and Lamb, 2002).

## 2.5 Wave Formation

### 2.5.1 Steepening of the internal tide

Wave arrival times at SW30 did not consistently and directly correspond to the barotropic, semidiurnal tide. Despite the lack of predictability, the development of NLIWs from the internal tide was elucidated from ship observations (Fig. 2.9). As an example, the tidal front, *Peggy B*, was first transited near 0510 UTC 17 August 2006 (Fig. 2.9a). The front traveled at 1 m $s^{-1}$ shoreward and was tracked for approximately 3 hours as the front edge steepened (e.g., Fig. 2.9d-e), after which a leading NLIW emerged from the front in between 0–5 km as the barotropic tide ebbed. Phase speeds, calculated by differencing time and locations indicated by black triangles, decreased from 1 m $s^{-1}$ to 0.9 m $s^{-1}$ between Fig. 2.9e and f. Note that a second wave packet (*Peggy A*) is also visible in Fig. 2.9a. This packet led *Peggy B* by approximately 6 hours, and displayed a similar propagation direction (300°). *Wave Sonny* was also tracked from an early stage and reveals a similar story to that detailed above for *Peggy B*. Both *Peggy* and *Sonny* occurred near the start of the period characterized by NLIW arrival times that were phased with $u_{M2}$.

The generation of *Peggy B* seems to conform to the perhaps more common, and well-studied problem of NLIW evolution from a linear internal tide (Lee and Beardsley, 1974; Holloway, 1987; Smyth and Holloway, 1988; Holloway et al., 1997; Scotti et al., 2007). To assess why wave generation occurs at the observed loca-

tion, we consider the simple, first-order KdV equation (Eq. 2.1 with $\alpha_1 = 0$), in which wave evolution depends upon the balance between nonlinear advection, $(c + \alpha\eta)\partial\eta/\partial x$, and dispersion, $\beta\partial^3\eta/\partial x^3$. In order to approximate the roles of these two competing influences for the NJ waves, we solve Eq. 2.1 with $\alpha_1 = 0$ initialized with a sinusoidal M2 tidal wave, $\eta^0 = a \sin 2\pi f_{M2} t$, where $a$ is the amplitude.

The initial value problem is solved via a finite difference method outlined by Pelinovskiy et al. (1994). The coefficients, $c_0$, $\alpha$, and $\beta$, are allowed to vary across the shelf and are defined using a 12-hour time series of profiles taken across the shelf break starting at 0230 UTC 11 August 2006. The shelf break series extends the range presented in Fig. 2.6 out to 22 km. For modeling purposes, coefficients were calculated neglecting shear, and values were bin-averaged and then fit to empirical functions (Fig. 2.10a, solid lines). The variable-coefficient KdV equation requires an additional term,

$$\frac{c_0}{2Q}\frac{dQ}{dx}\eta,$$

where $Q$ is an amplification factor that is introduced to account for spatial variations in background conditions. As with Eq. 2.1 the reader is referred to Grimshaw et al. (2004) for the explicit form of $Q$.

Figure 2.10b shows the modeled displacements with dispersion (black) and without dispersion (grey). Initially, nonlinearity dominates the balance and the modeled displacements with dispersion agree almost identically to the non-dispersive case (12 km and 7 km). However, when the tide has steepened to a point that higher-order derivatives are no longer small, dispersion becomes important and the shock created by nonlinear steepening begins to form a wave packet (5 km). Our interest in using this simplified model is not to accurately describe the evolution of the consequent NLIWs, but instead to approximate where on the shelf the balance

between dispersion and nonlinearity is reached, thus providing a comparison point for the observed wave formation. Indeed the modeled NLIW formation point (near 5 km) is in agreement with the observed NLIW formation location for *Peggy B* and *Sonny* (not shown), suggesting that steepening of the internal tide is at least one generation mechanism. Initializing the model with slightly larger/smaller amplitudes results in earlier/later NLIW formation. Since the modeled coefficients are based on one, short time series, we also expect some variation ($\pm$ a few km) in the modeled formation point due to changes in $\alpha$ associated with variable stratification and shear at the shelf break.

### 2.5.2 A more complicated scenario

Observations of another wave group, *Florence*, show a more elaborate, convoluted example of wave formation (Fig. 2.11). Here, a wave group forms from a sub-surface onshore pulse first observed near the beginning of the flood tidal phase near 10 km, further offshore than the formation location of *Peggy B* and at a different phase of the barotropic tide. As in the previous example, the first transect clearly shows a wave group preceding *Florence* by approximately 6 hours (Fig. 2.11, right panel at -6 km), which also propagated in the same direction as *Florence* at 300°. While these observations were recorded earlier in the month than those discussed above for *Peggy B*, both series show the generation of multiple wave groups per M2 tidal cycle.

Obviously, the simple KdV model presented above does not account for the differences in wave formation between *Peggy B* and *Florence*, and in particular does not address the formation of multiple wave packets per tidal cycle. Preliminary efforts with a fully nonlinear, three-dimensional model, which are forced only by the M2 barotropic tide, have shown that multiple packets per tidal cycle sometimes emerge from a canyon to the south of the SW06 study site (Alberto Scotti, personal

communication). The formation of multiple packets per tidal cycle would explain a large portion of the arrival time variability, particularly during certain periods when two wave groups per M2 tidal cycle were observed, e.g., 1–2 August and 13–14 August.

### 2.5.3 Internal Tide and NLIW Modulation by Inertial Waves

Since both the arrival times and amplitudes of the NLIWs observed between approximately the 17–21 August were anomalous, we examine the mooring records of across-shelf velocity during this time period in greater detail (Fig. 2.12). Interestingly, onshore pulses at the shelf break did not always result in large onshore velocity pulses (Fig. 2.12c) or large NLIWs (Fig. 2.12d) on the shelf. For example, consider the near-surface, onshore pulses that are labeled in red in Fig. 2.12a. Following the corresponding arrows through the mooring array, we find that the resultant onshore pulses at the outer- and mid-shelf mooring were reduced in duration and magnitude (Fig. 2.12b-c). The opposite effect was also apparent with relatively weak, onshore pulses at the shelf break resulting in strong pulses on the shelf (refer to waves labeled in blue).

Recall from section 2.3b, that the variability and energy in near-inertial motions were of the same magnitude as the M2 internal tide, particular on the shelf. A closer inspection of Fig. 2.4 shows that while the M2 tide propagated across the shelf, inertial motions were relatively coherent. The phasing of these two components, one of which was essentially a function only of time (inertial) and the other which depended on location as well as time (M2), necessarily impacted NLIW development by altering the ambient velocity through which waves propagated. Furthermore, the interaction of the standing near-inertial wave with a propagating M2 wave can account for the modulation of the onshore velocity pulses apparent in Fig. 2.12a-c.

The interference between the near-surface M2 and the inertial series at SW30 is quantified by the normalized product,

$$\Phi \equiv \frac{u_{M2} \times u_f}{max(u_{M2} \times u_f)},$$

where only regions in which near-surface $u_{M2} < 0$ are plotted in Fig. 2.12d. When $\Phi$ is positive (blue) the two series constructively interfere; the opposite is true when $\Phi$ is negative (red). In general, weak pulses that turned into strong pulses (and large internal waves) correspond to $\Phi > 0$, while strong pulses that became weaker on the shelf correspond to $\Phi < 0$. In order to understand this response, we proceed by first considering the superposition of a linear, propagating M2 wave with standing inertial wave, and we will attempt to address the influence on the formation of NLIWs afterward.

Distance-time plots of near-surface, across-shelf velocity components, $u_{M2}$, $u_f$, and $u_f + u_{M2}$, are shown in Fig. 2.13 for harmonic fits calculated from the mooring data (panels a–c) and for modeled linear waves (panels e–g). Harmonic fits to the observed time series were first averaged between 10–25 m, and then interpolated across the shelf between moorings: SW30, Gawarkiewicz's mooring, and SW42. $u_{M2}$ was interpolated linearly along M2 characteristics calculated using the fit to $c_0$ shown in Fig. 2.10a; and, $u_f$ was linearly interpolated across the shelf between SW30 and SW42. Bottom panels (e–g) show time series created using a propagating, M2 wave of the form $u_{M2} = a_{M2} \sin(f_{M2}x/\overline{c_0} + f_{M2}t + \phi_{M2})$ and a standing inertial wave, $u_f = a_f \sin(f_f t + \phi_f)$. The amplitudes ($a_i$) and phases ($\phi_i$) were selected to agree with observed time series. Through the remainder of this section, use of $u_{M2}$ and $u_f$ refer to the near-surface averages and not to the full depth field.

The time required for the M2 wave to propagate from the shelf break to SW30

was slightly over 6 hours, corresponding to approximately half of the M2 tidal period and a third of the inertial period. As a result, the phasing between $u_{M2}$ and $u_f$ at the slope mooring differs from the phasing of the two signals on the shelf. For waves B, D, E, G, H, and K (i.e., blue waves), near-surface $u_f$ was directed offshore, opposing $u_{M2}$, at the shelf break. The combination of $u_{M2}$ and $u_f$ thus produced a smaller, onshore velocity pulse at the shelf break. However, on the shelf, these same M2 waves propagated through a $u_f$ directed onshore (Fig. 2.12d and Fig. 2.13b), producing a larger onshore, velocity. The reverse was true for waves C, F, and I (i.e., red waves). For these waves, $u_f$ was directed onshore at the shelf break, creating a large, onshore pulse, and, $u_f$ was directed offshore on the slope, adding to produce a smaller onshore pulse. Waves A and J do not fit the pattern as well, although we note that while these waves are designated red the magnitudes of the near-surface, onshore pulses did not change much between the slope and shelf.

The strong beating that emerges in Fig. 2.13c results partially because of the relation between the M2 tidal period and the inertial period at this latitude, $3\tau_{M2} = 2\tau_f$, producing a pattern that repeats every 37 hours. While this does not account for all the variability, the observations (Fig. 2.13a–c) agree well with the modeled time series (Fig. 2.13e–g), although a constant phase speed was assumed for the modeled M2 waves. The pattern created by the superposition of $u_f$ and $u_{M2}$ is clearly evident in Fig. 2.13g. Arrival times of the M2 baroclinic tide at 18 km with respect to the across-shelf average of near-surface $u_f$ (Fig. 2.13d,h) further emphasize the phase pattern, in which one onshore, M2 pulse occurs near peak, onshore $u_f$ followed by a series of two M2 pulses occurring slightly offset from peak offshore $u_f$.

While the simple addition of linear, $u_f$ and $u_{M2}$ seems to explain the variation in the onshore pulses, the effect on the NLIW field is perhaps more subtle. Specifically, why did larger amplitude waves form when $u_f$ was in phase with $u_{M2}$

at SW30 (Fig. 2.12d, e)? One possible explanation is that near-inertial shear on the outer shelf and slope influences the coefficient of nonlinearity, $\alpha$, and hence will effect tidal steepening and consequent NLIW formation. As mentioned, the time required for an M2 wave to propagate between the shelf break and SW30 ($> 6$ hrs) is a significant portion of both the M2 and inertial period. As such, the near-inertial shear changed significantly between the slope and the shelf, and, waves associated with a positive/negative $\Phi$ at SW30 were associated with a negative/positive $\Phi$ near the shelf break. For waves color-coded blue in Figs. 2.12 and 2.13, the inertial shear on the outer shelf/slope was positive (i.e., the upper layer opposed the direction of wave propagation). Positive shear decreases $\alpha$, thus increasing nonlinearity. (That is, $\alpha$ becomes more negative.) Linear, tidal steepening would happen earlier for these waves, and as a result we would expect to see larger amplitude NLIWs at SW30. The opposite is true for negative inertial shear near the shelf break, which was present for most red waves. In this case, nonlinearity is decreased as $\alpha$ becomes less negative, and shock formation would be delayed. The phasing between $u_f$ and $u_{M2}$ at the shelf break is summarized in Fig. 2.13d, h.

## 2.6 Fluxes and Transport

### 2.6.1 Vertical Heat Flux

Elevated values of dissipation were typically observed in the leading waves of each group. As discussed in Shroyer et al. (2009a), these large values were often confined to the trailing edge of the wave interface. In the leading wave of *Mika*, for example, billows of increased backscatter and accompanying high dissipation rates were observed in lee of the trough (Fig. 2.14a). The increased mixing attributed to these occurrences naturally gives way to localized regions of enhanced vertical heat flux, $J_q$ (Fig. 2.14b). $J_q$ may be calculated from the measured dissipation ($\epsilon$),

stratification ($N^2$), and temperature gradient ($dT/dz$) by assuming that a turbulent eddy diffusivity can be written as

$$K_\rho = \frac{\Gamma \epsilon}{N^2},$$

where $\Gamma$, the mixing efficiency, is assumed to be 0.2 (Osborn, 1980). The heat flux may then be calculated as

$$J_q = \overline{\rho} C_p K_\rho \frac{dT}{dz},$$

using an average density, $\overline{\rho} = 1024$ kg m$^{-3}$, and the heat capacity of seawater, $C_p$.

For *Wave Mika* (Fig. 2.14), $J_q$ averaged between 10–30 m ($J_{q(10-30)}$) peaked at over 1000 times greater in the leading wave than in the profiles made just prior to wave arrival. On average in the leading three waves, $J_{q(10-30)}$ is about 300 times greater than background levels. While reduced in magnitude, the bore-like tail of *Mika* continued to exhibit elevated vertical heat fluxes. $J_{q(10-30)}$ averaged through the extended wave train is 100 times greater than background levels. We note that while this example displayed large values of dissipation and heat flux, it was not extreme.

In order to provide an order of magnitude estimate for the contribution of wave groups to heat flux on the entire shelf, average profiles of heat flux in 1) waves and 2) background profiles were calculated for all observations (Fig. 2.15). Values above ten meters depth were discarded, as turbulence measurements are unreliable near the surface, due to the presence of the ship from which they were made. Furthermore, when $N^2$ was small unreliable estimates of $K_\rho$ resulted, and samples where $N^2 < 5 \times 10^{-4}$ s$^2$ were excluded. Fluxes were first averaged in isopycnal coordinates to account for wave perturbations, and then re-mapped onto the depth coordinate (Fig. 2.15b). Heat fluxes calculated in waves are designated $J_q^w$, and heat fluxes calculated

from background profiles are designated $J_q^0$. The average downward surface heat flux (black arrow, Fig. 2.15) was estimated as 120 W m$^{-2}$ using bulk parametrizations based on Dorrestein (1979).

Across the pycnocline, the average $J_q^w$ was an order of magnitude greater than background fluxes (840 W m$^{-2}$ compared to 70 W m$^{-2}$). This difference is attributed to a slightly larger temperature gradient in the waves ($\sim$ 10%, Fig. 2.16a) and eddy diffusivities that are on average (over the entire water column) three times as large in the waves (Fig. 2.16b). These short episodes of wave activity were highly effective in redistributing surface heat below the thermocline, but these events were sporadic in time.

Mooring data offers a means of estimating the amount of time in which NLIWs were present at a particular place. Using velocity data from SW37 (-10 km) and SW29 (-21 km), we assume NLIWs are present when the square of the depth-averaged vertical velocity ($w^2$) exceeds a certain magnitude. The velocity was first filtered to include signals with periods between 2 and 10 minutes, and then three cut-off values ($w_c^2$ = [2, 4, 8] $\times$ 10$^{-4}$ m$^2$s$^{-2}$) were selected based on the ship measurements of the magnitude of vertical velocity in the waves, which had a median value of 0.02 m s$^{-1}$, corresponding to $w_c^2 = 4 \times 10^{-4}$ m$^2$s$^{-2}$. This method estimates that waves were present [11.0%, 5.3%, 2.7%] of time at SW29 and [22.8%, 8.5%, 3.3%] at SW37. Independent, qualitative analysis of the velocity and temperature record at SW29 resulted in an estimate of NLIW activity during 10% of the total time.

Assuming that $w_c^2 = 4 \times 10^{-4}$ m$^2$s$^{-2}$ is the most reasonable indicator of NLIW activity, a time-weighted average can be calculated using

$$\% \text{ Heat Flux by Waves} = \frac{P^w J_q^w}{P^w J_q^w + (1 - P^w) J_q^0} \times 100,$$

where $P^w$ is the fraction of time NLIWs were present. Accordingly, we estimate that NLIWs contributed as much as 40–50% of the heat flux across the thermocline. (We use $J_q^w = 840$ W m$^{-2}$ and $J_q^0 = 70$ W m$^{-2}$ in the above expression.) The time-weighted total heat flux, $P^w J_H^w + (1 - P^w) J_q^0$, is approximately equal to the average surface heat flux. In fact, using the average percentile between SW29 and SW37, i.e., mean$(5.3\%, 8.5\%) = 6.75\%$, the time-weighted total heat flux (122 W m$^{-2}$) is almost identical to the estimated surface heat flux. The agreement between these two values provides independent support for our estimates of the $J_q^w$ and $J_q^0$. However, this result is obviously highly dependent on ambient conditions. For example, the response of the shelf to a large storm event would shift this result considerably as a consequence of not only increased wind-driven mixing but also the likely reduction of NLIWs associated with the destruction of the stratification. Furthermore, depending on the pycnocline depth our estimates of $J_q^0$ may be biased to values in the lower pycnocline (see Fig. 2.14), although the average maximum stratification does occur beneath 10-m depth as indicated in Fig. 2.15.

### 2.6.2 Particle Transport

NLIWs have been attributed with the transport of plankton, larvae, and small fish (e.g., Shanks and Wright, 1987; Pineda, 1991; Lamb, 1997). In particular, waves with trapped cores of recirculating fluid would provide a highly effective means of shoreward transport for oceanic biota. While our observations do not present evidence for such trapped cores, these waves can still result in significant transport distance, particularly as the particle speeds begin to approach the wave propagation speed. Particle transport distances were evaluated using

$$\text{transport} = \int_{x'_R}^{x'_L} \frac{u_w(x', \rho_0)}{c - u_w(x', \rho_0)} dx',$$

following Lamb (1997). Here, $u_w$ is a function of $x' = x - ct$ and the background density, $\rho_0(z)$. With the assumption that streamlines follow isopycnals, the above expression may be integrated for a constant density surface to find transport distances. Note in the limit $u_w \rightarrow c$, the transport becomes infinite corresponding to the case of a trapped core.

Typically, maximum transports were located at the surface in agreement with theoretical representations of NLIWs (Fig. 2.17a and c); however, a handful of occurrences had a maximum in wave velocity beneath the surface (e.g., Fig. 2.17b). The wave velocity is calculated by subtracting the background velocity profile interpolated along streamlines. While care was taken to ensure the proper background velocity was subtracted, it is possible that a near-surface (within a few meters), offshore current would not be resolved by ship-based measurements. Failing to account for such a signal would result in a sub-surface maximum in horizontal wave velocity. In such cases, the calculated surface transport is likely an underestimate of the true surface transport. Surface transports for the leading three waves in each NLIW group were on average a few hundred meters (Fig. 2.18a), with a maximum near a half kilometer occurring at -15 km (Fig. 2.18b, solid line). Transport distances of larger-amplitude waves (e.g., *Sonny* and *Wyatt*) would often exceed 1 km at a given location. *Rosey* was an anomaly with local transport distances exceeding 2 km at multiple locations and an average transport of almost 1.5 km (Fig. 2.18b, dashed line).

These values represent only the leading three waves in each group, although wave groups were typically comprised of more than ten waves on the shelf. For example, *Mika*/*Rosey* consisted of 13/16 well-formed waves at SW30 (0 km); these numbers increased to 20 and 30, respectively, at SW29 (-21 km). For most wave packets we can assume total transports on the order of one kilometer. However, for *Rosey*, expected transports are near 10 km (in the mid-shelf region). We note that

the above analysis is extremely sensitive to the estimated wave speed and includes many assumptions. In particular, we have ignored any contributions due to the particle's horizontal speed (i.e., swimming fish). As a test on sensitivity associated with either error in our estimate of wave speed or the presence of swimmers, the above calculation was repeated using a constant swimming speed of 0.1 m $s^{-1}$, which is equivalent to reducing $c$ by 0.1 m $s^{-1}$. The result increased average transport distances by 100 m for most waves, but more than doubled those of *Rosey*.

### 2.6.3 *Rosey*: An Amplitude-Limited Wave Group

Depending on the stratification and background shear, nonlinear waves may be bounded in amplitude such that increased energy input results in an increase in wavelength. As the wavelength increases, a region of flat isopycnals develops at the wave's center. In this region, the velocity of the so-called "table" solitons, which have also been termed thick or flat solitons, is horizontally uniform and is referred to as the conjugate of the upstream flow (Lamb and Wang, 1998). *Wave Rosey* was the most energetic, largest amplitude wave train that was observed from the ship. Consequently, above average heat fluxes and transport distances were attributed to this wave group. High-resolution measurements from the ship reveal a unique shoaling story for *Rosey*, in which the leading wave became thick as the limiting amplitude was reached.

Inshore of the transect presented in Fig. 2.17c, the leading wave grew by close to 5 m in amplitude and took on a "squarish" nature reminiscent of a table soliton (Fig. 2.19). At this location horizontal velocities exceeded 0.75 m $s^{-1}$ and vertical velocities reached 0.25 m $s^{-1}$. The downward velocity pulse at the leading edge was separated by over 100 m from the upward return at the trailing edge of the wave, further emphasizing the square-like nature of the wave. Backscatter images across the shelf clearly show the increase in amplitude and wavelength of the leading

wave (Fig. 2.20b). Using the eKdV equation, the weakly nonlinear (WNL) limiting amplitude was calculated as

$$A_{limit} = -\frac{\alpha}{\alpha_1}$$

(e.g., Grimshaw et al., 2004; Stanton and Ostrovsky, 1998). Comparison of the measured displacement amplitude to the WNL limit shows that the two converged as *Rosey* traveled shoreward, hinting that the wave form approached a conjugate flow state.

## 2.7 Summary

During the Shallow Water 2006 experiment on New Jersey's continental shelf, nonlinear internal waves experienced a highly variable environment and were influenced by a variety of field and forcing conditions, including mesoscale shifts in stratification at the shelf break, changing wind conditions, and energetic near-inertial shear. The resultant NLIWs were characterized by two regimes. Over a large portion of the month NLIW displacements were on average -8m, with wave arrival times at a given location occurring irregularly with respect to the barotropic tide. However, from approximately 17–22 August NLIW displacements exceeded 15m; and, during approximately the same period, wave arrival times were more clearly phased with the barotropic tide.

NLIW formation from the larger scale, tidal flow was documented for a few wave groups. In one case, formation seems to be relatively straightforward with waves likely developing as the linear internal tidal front first steepens into a shock and then disperses into a wave train. However, the second example is not straightforward with a highly-sheared, background state. In this case, NLIWs emerge from a subsurface, onshore velocity pulse. In both cases, there is evidence that NLIWs

are created at $\sim$ 6-hour intervals as opposed to only once a semidiurnal tidal period. During the time period of large-amplitude waves, the incoming internal tide appears to have been modulated by the near-inertial wave field. When the two were out of phase with each other on the slope, initially weak, onshore pulses at the shelf break were stronger on the shelf and were accompanied by larger NLIWs.

In an attempt to quantify some effects that these NLIWs had on the shelf environment, estimates of heat flux and mass transport by the waves are provided. Heat fluxes attributed to the NLIWs were dominated by short, intense mixing events. When averaged over the shelf and over time, NLIW driven heat flux accounted for as much as 40-50% of the average total heat flux through the pycnocline during the month of August 2006. Mass transport by the waves was in most cases less than a kilometer per wave group; however, at least one wave group was capable of transporting mass on the order of 10 km across the shelf. This anomalous wave group was likely amplitude-limited as it approached the conjugate flow limit.

Possibly, the most useful result of this work is simply the documentation of the short-term variability inherent in the shelf NLIW field. The variability is expressed not only in the character (e.g., amplitude and arrival times) of the waves, but also in the wave formation and shoaling. For example, consider the polarity conversion of some wave groups (albeit all large-amplitude waves) that was observed at the locations where $\alpha > 0$ (Fig. 2.6c), while for other groups depression waves continued to persist inshore for 10s of kilometers. Such details suggest that the applicability of modeling studies initialized with climatology, or highly averaged data, must to some extent be limited when considering wave evolution, since the time and space scales that influence the NLIWs are not well-represented by long-term averages.

## 2.8 Acknowledgments

This work was funded by the Office of Naval Research. We thank the Captains and crews of the R/V Oceanus, which performed the tracking experiment, and the R/V Knorr, which deployed and recovered moorings. Mike Neeley-Brown, Ray Kreth, Alexander Perlin, Greg Avicola, and Sam Kelly helped obtain the data during the wave tracking experiment. John Kemp, James Lynch, and James Irish were responsible for the mooring deployment and recovery. We also thank Glen Gawarkiewicz for sharing data.

## Bibliography

Alpers, W., 1985: Theory of radar imaging internal waves. *Nature*, **314**, 245–247.

Apel, J., H. Byrne, J. Proni, and R. Charnell, 1975: Observations of oceanic internal and surface waves from the Earth Resources Technology Satellite. *J. Geophys. Res.*, **80**, 865–881.

Apel, J. R., M. Badiey, C.-S. Chiu, S. Finette, R. Headrick, J. Kemp, J. F. Lynch, A. Newhall, M. H. Orr, B. H. Pasewark, D. Tielbuerger, A. Turgut, K. von der Heydt, and S. Wolf, 1997: An overview of the 1995 SWARM shallow-water internal wave acoustic scattering experiment. *J. Oceanic Engin.*, **22**, 465–500.

Apel, J. R., J. R. Holbrook, A. K. Liu, and J. J. Tsai, 1985: The Sulu Sea Internal Soliton Experiment. *J. Phys. Ocean.*, **15**, 1625–1651.

Chapman, D., J. Barth, R. Beardsley, and R. Fairbanks, 1986: On the continuity of mean flow between the Scotian Shelf and the Middle Atlantic Bight. *J. Phys. Ocean.*, **16**, 758–772.

Chereskin, T. K., 1983: Generation of internal waves in Massachusetts bay. *J. Geophys. Res.*, **88**, 2649–2661.

Colosi, J. A., R. C. Beardsley, J. F. Lynch, G. Gawarkiewicz, C.-S. Chiu, and A. Scotti, 2001: Observations of nonlinear internal waves on the outer New England continental shelf during the summer Shelfbreak Primer study. *J. Geophys. Res.*, **106**, 9587–9601.

Dorrestein, R., 1979: On the vertical buoyancy flux below the sea surface as induced by atmospheric factors. *J. Phys. Ocean.*, **9**, 229–231.

Duda, T. F., J. F. Lynch, J. D. Irish, R. C. Beardsley, S. R. Ramp, C.-S. Chiu, T. Y. Tang, and Y.-J. Yang, 2004: Internal tide and nonlinear internal wave behavior at the continental slope in the northern South China Sea. *IEEE J. Oceanic Engin.*, **29**, 1105–1130.

Egbert, G. D., A. Bennett, and M. Foreman, 1994: Topex/Poseidon tides estimated using a global inverse model. *J. Geophys. Res.*, **99**, 24821–24852.

Egbert, G. D., and R. D. Ray, 2000: Significant dissipation of tidal energy in the deep ocean inferred from satellite altimeter data. *Nature*, **405**, 775–778.

Farmer, D. M., and L. Armi, 1999: The generation and trapping of internal solitary waves over topography. *Science*, **283**, 188–190.

Fratantoni, P., R. Pickart, D. Torres, and A. Scotti, 2001: Mean structure and dynamics of the shelfbreak jet in the Middle Atlantic Bight during Fall and Winter. *J. Phys. Ocean.*, **31**, 2135–2156.

Gasparovic, R., J. Apel, and E. Kasischke, 1988: An overview of the SAR Internal Wave Signature Experiment. *J. Geophys. Res.*, **93**, 12304–12316.

Grimshaw, R., E. Pelinovsky, T. Talipova, and A. Kurkin, 2004: Simulation of the transformation of internal solitary waves on oceanic shelves. *J. Phys. Ocean.*, **34**, 2774–2791.

Haury, L. R., M. G. Briscoe, and M. H. Orr, 1979: Tidally generated internal wave packets in Massachusetts Bay. *Nature*, **278**, 312–317.

Holloway, P. E., 1987: Internal hydraulic jumps and solitons at a shelf break region on the Australian North West shelf. *J. Geophys. Res.*, **92**, doi:10.1029/JC092iC05p05405, 5405–5416.

Holloway, P. E., E. Pelinovsky, T. Talipova, and B. Barnes, 1997: A nonlinear model of internal tide transformation on the Australian North West shelf. *J. Phys. Ocean.*, **27**, 871–896.

Houghton, R., and J. Marra, 1983: Physical/biological structure and exchange across the thermohaline shelf/slope front in the new york bight. *J. Geophys. Res.*, **88**, 4467–4481.

Inall, M. E., T. P. Rippeth, and T. J. Sherwin, 2000: Impact of nonlinear waves on the dissipation of the internal tidal energy at a shelf break. *J. Geophys. Res.*, **105**, 8687–8705.

Jackson, C. R., 2004: *An Atlas of Internal Solitary-like Waves and their Properties*. Global Ocean Associates, www.internalwaveatlas.com, second edition.

Jeans, D. R. G., and T. J. Sherwin, 2001: The variability of strongly non-linear solitary internal waves observed during an upwelling season on the Portuguese shelf. *Cont. Shelf Res.*, **21**, doi:10.1016/S0278-4343(01)00026-7, 1855–1878.

Kelly, S. M., J. D. Nash, and E. Kunze, 2009: Internal tide energy over topography. *J. Geophys. Res.*, submitted.

Kropfli, R., and S. Clifford, 1996: The Coastal Ocean Probing Experiment: further studies of air-sea interactions with remote and in-situ sensors. *Geoscience and Remote Sensing Symposium, 1996. IGARSS '96. 'Remote Sensing for a Sustainable Future.', International*, **3**, 1739–1741.

Lamb, K. G., 1997: Particle transport by nonbreaking internal solitary waves. *J. Geophys. Res.*, **102**, 18,641–18,660.

Lamb, K. G., and B. Wang, 1998: Conjugate flows and flat solitary waves for a continuously stratified fluid. *Phys. Fluids*, **10**, 2061–2079.

Lee, C.-Y., and R. C. Beardsley, 1974: The generation of long nonlinear internal waves in a weakly stratified shear flow. *J. Geophys. Res.*, **79**, 453–462.

Linder, C. A., and G. Gawarkiewicz, 1998: A climatology of the shelfbreak front in the Middle Atlantic Bight. *J. Geophys. Res.*, **103**, 18405–18423.

Liu, A. K., Y. S. Chang, M.-K. Hsu, and N. K. Liang, 1998: Evolution of nonlinear internal waves in the East and South China Seas. *J. Geophys. Res.*, **103**, 7995–8008.

Liu, A. K., Y. Zhao, T. Y. Tang, and S. R. Ramp, 2004: Model-data assimilation of internal waves in ASIAEX 2001. *IEEE J. Oceanic Engin.*, **29**, 1144–1156.

Moody, J., and B. Butman, 1984: American continental shelf, bulletin 1611. *U.S. Geological Society*.

Moum, J., J. Klymak, J. Nash, A. Perlin, and W. Smyth, 2007: Energy transport in nonlinear internal waves: Experimental determination. *J. Phys. Ocean.*, **37**, 1968–1988.

Moum, J. N., M. C. Gregg, R. C. Lien, and M. E. Carr, 1995: Comparison of turbulence kinetic energy dissipation rate estimates from two ocean microstructure profilers. *J. Atmos. Ocean. Tech.*, **12**, 346–366.

Moum, J. N., and J. D. Nash, 2008: Seafloor pressure measurements of nonlinear internal waves. *J. Phys. Ocean.*, **38**, 481–491.

Nash, J. D., and J. N. Moum, 2005: River plumes as a source of large-amplitude internal waves in the coastal ocean. *Nature*, **437**, 400–403.

Nash, J. D., E. Shroyer, J. Moum, T. Duda, H. Graber, J. Irish, and J. Lynch, 2009: Mesoscale influences on the generation of the internal tide and nonlinear internal waves over new jerseys continental shelf, in preparation.

New, A. L., and R. D. Pingree, 1990: Large-amplitude internal soliton packets in the central Bay of Biscay. *Deep Sea Res.*, **37**, 513–524.

Orr, M. H., and P. C. Mignerey, 2003: Nonlinear internal waves in the South China Sea: Observation of the conversion of depression internal waves to elevation waves. *J. Geophys. Res.*, **108**, doi:10.1029/2001JC001163, 3064–3079.

Osborn, T. R., 1980: Estimates of the local rate of vertical diffusion from dissipation measurements. *J. Phys. Ocean.*, **10**, 83–89.

Osborne, A. R., and T. L. Burch, 1980: Internal solitons in the Adaman Sea. *Science*, **208**, 451–460.

Pelinovskiy, E. N., Y. A. Stepanyants, and T. G. Talipova, 1994: Simulation of nonlinear internal wave propagation in horizontally inhomogeneous ocean. *Atmospheric and Oceanic Physics*, **30**, 77–83.

Perry, R., and G. Schimke, 1965: Large amplitude internal waves observed off the northwest coast of Sumatra. *J. Geophys. Res.*, **70**, 2319–2324.

Pineda, J., 1991: Predictable upwelling and the shoreward transport of planktonic larvae by internal tidal bores. *Science*, **253**, 548–549.

Ramp, S. R., T.-Y. Tang, T. F. Duda, J. F. Lynch, A. K. Liu, C.-S. Chiu, F. Bahr, H.-R. Kim, and Y. J. Yang, 2004: Internal solitons in the northern South China Sea Part I: sources and deep water propagation. *IEEE J. Oceanic Engin.*, **29**, 1157–1181.

Sandstrom, H., and J. A. Elliott, 1984: Internal tide and solitons on the Scotian Shelf: A nutrient pump at work. *J. Geophys. Res.*, **89**, 6415–6426.

Scotti, A., R. Beardsley, and B. Butman, 2007: Generation and propagation of nonlinear internal waves in Massachusetts Bay. *J. Geophys. Res.*, **112**, doi:10.1029/2007JC004313.

Shanks, A. L., and W. G. Wright, 1987: Internal-wave-mediated shoreward transport of cyprids, megalopae, and gammarids and correlated longshore differences in the settling rate of intertidal barnacles. *J. Exper. Mar. Biol. Ecol.*, **114**, 1–13.

Shroyer, E., J. Moum, and J. Nash, 2009a: Energy transformation and dissipation in the evolving NLIW field over New Jersey's continental shelf, in preparation.

— 2009b: Mode-2 waves on the continental shelf: ephemeral components of the nonlinear internal wave field. *Geophys. Res. Let.*, submitted.

— 2009c: Observations of polarity reversal in shoaling nonlinear internal waves. *J. Phys. Ocean.*, **39**, 691–701.

Small, J., 2003: Refraction and shoaling of nonlinear internal waves at the Malin shelf break. *J. Phys. Ocean.*, **33**, 2657–2674.

Small, J., T. C. Sawyer, and J. C. Scott, 1999: The evolution of an internal bore at the Malin shelf break. *Ann. Geophys.*, **17**, 547–565.

Smyth, N. F., and P. E. Holloway, 1988: Hydraulic jump and undular bore form on a shelf break. *J. Phys. Ocean.*, **18**, 947–962.

Stanton, T. P., and L. A. Ostrovsky, 1998: Observations of highly nonlinear internal solitons over the continental shelf. *Geophys. Res. Let.*, **25**, 26952698.

Stastna, M., and K. Lamb, 2002: Large fully nonlinear internal solitary waves: The effect of background current. *Phys. Fluids*, **14**, 2987–2999.

Tang, D. J., J. N. Moum, J. F. Lynch, P. Abbot, R. Chapman, P. Dahl, T. Duda, G. Gawarkiewicz, S. Glenn, J. A. Goff, H. Graber, J. Kemp, A. Maffei, J. Nash, and A. Newhall, 2007: Shallow Water '06. *Oceanography*, **20**.

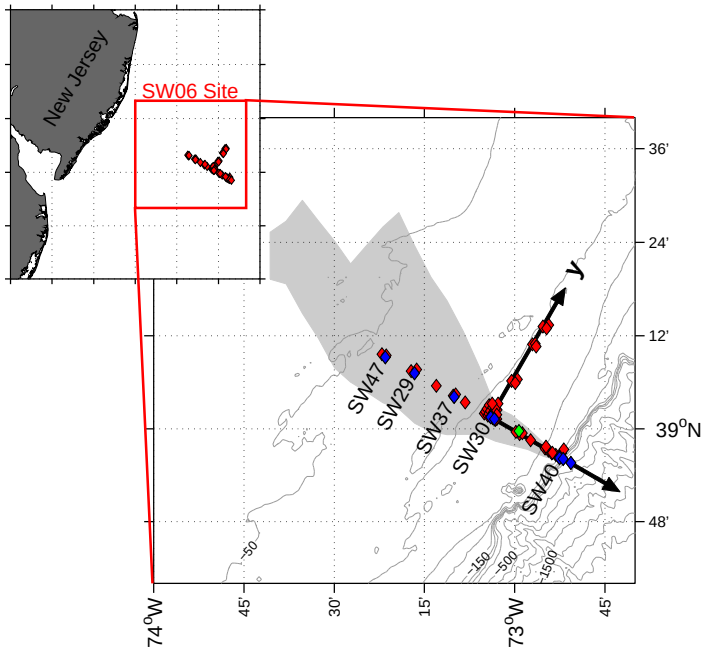


FIGURE 2.1: Site bathymetry, mooring location (diamonds) and wave transect boundary (grey cloud). Blue diamonds show environmental moorings used in this analysis. For reference, environmental moorings separated by large distances are labeled. Isobaths less the 250-m depth are plotted every 25 m, and isobaths greater than this depth are plotted every 250 m.

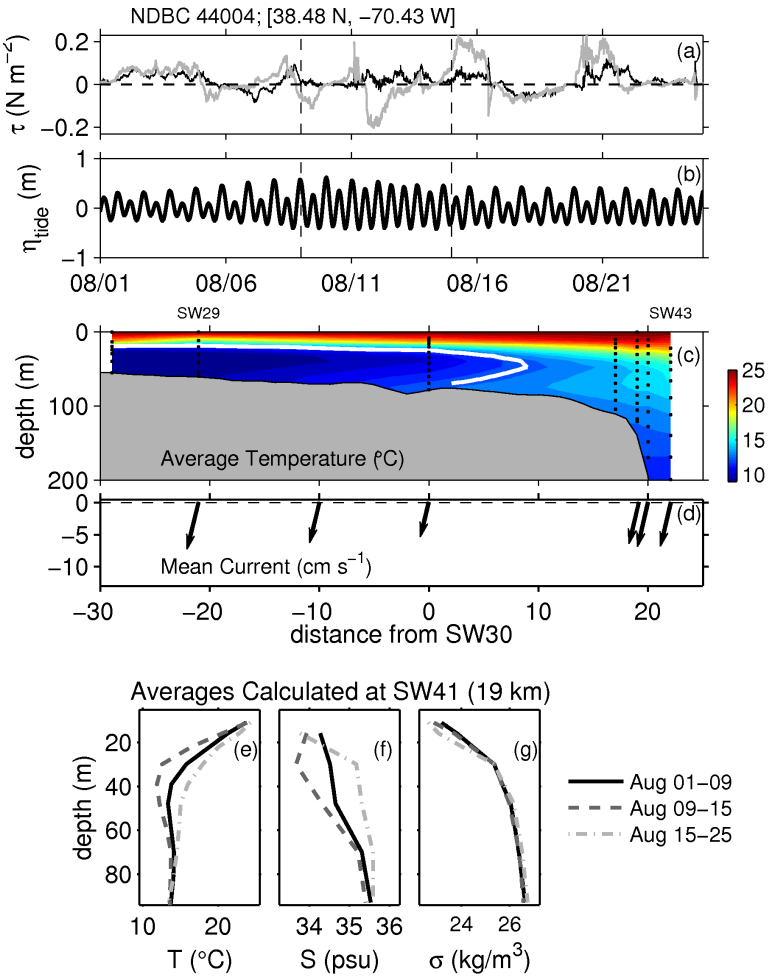


FIGURE 2.2: Summary of mesoscale conditions. (a) Across- and along-shore wind stress (black/grey) from NDBC buoy 44004 (38°29′N, 70°26′W). (b) Tidal height computed from a bottom pressure sensor on mooring SW38 (1 km). (c) Average across-shelf temperature during the month of August. The 12.5° C isotherm is shown in white. Actual mooring locations are at [22, 20, 19, 17, 0, -21, -29] km; temperature sensor depths are indicated by black dots. (d) Detided mean current over the month of August. Arrow locations show positions of moorings equipped with acoustic Doppler profilers with the exception of SW38. Time-averages of (e) temperature, (f) salinity, and (g) density for periods separated by vertical dashed lines in panels (a) and (b).

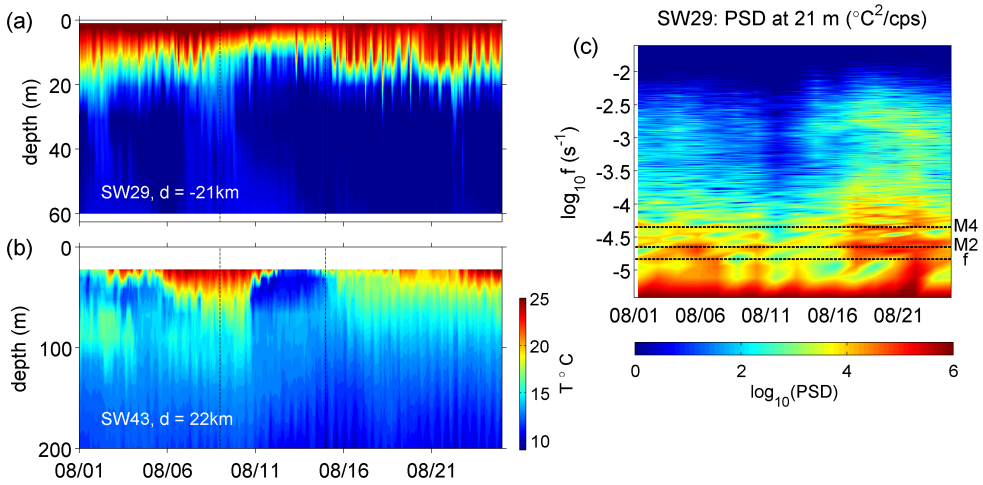


FIGURE 2.3: Slope and shelf temperature record. Temperature binned in hour blocks at an (a) inshore mooring and (b) offshore mooring. (c) Spectrogram of temperature at 21 m depth on SW29.

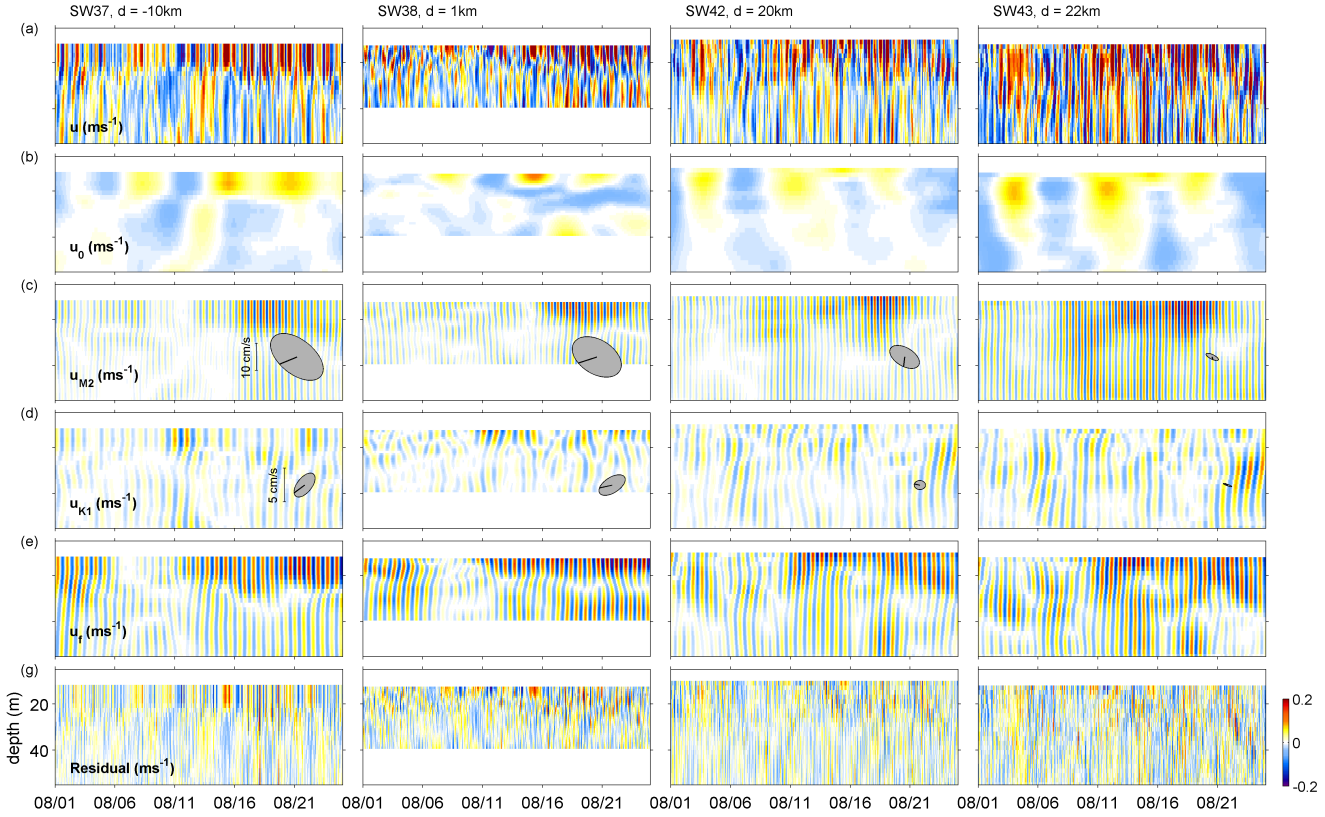


FIGURE 2.4: Harmonic fits to mooring baroclinic velocity records. Across-shelf, baroclinic velocity data from SW37, SW38, SW42, and SW43 arranged with the furthest inshore mooring to the left. Shown are (a) the total across-shelf velocity, (b-d) harmonic fits to M2, K1, and near-inertial frequency, (e) the sum, $u_0 + u_{M2} + u_{K1} + u_f$, and (f) the residual velocity. The color scale for all axes are the same, and for all moorings only the upper 60 m are shown. Barotropic tidal ellipses for the M2 and K1 components are shown in (b) and (c), respectively; note M2 and K1 ellipses have different scales. Phase lines show the tidal velocity at 0000 UTC 1 August 2006. For ellipses, north is vertical.

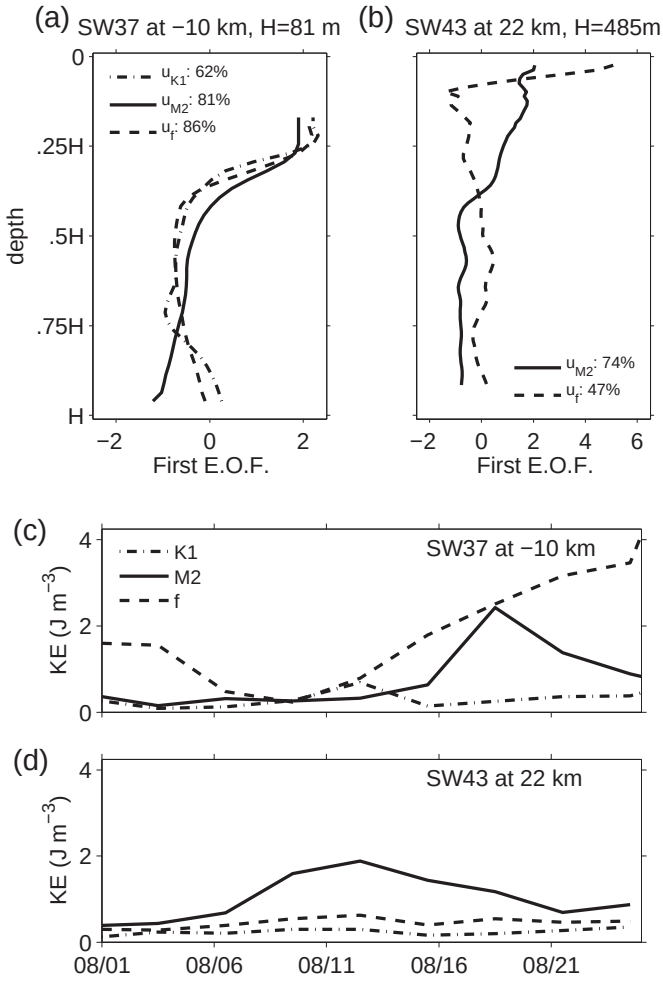


FIGURE 2.5: Vertical structure and energetics of inertial and tidal data. First E.O.F. calculated from harmonic fits of $u_{K1}$, $u_f$, and $u_{M2}$ on (a) the shelf and (b) the slope. Three day averages of the kinetic energy in the K1, M2, and inertial baroclinic fields at a (c) shelf and (d) slope mooring.

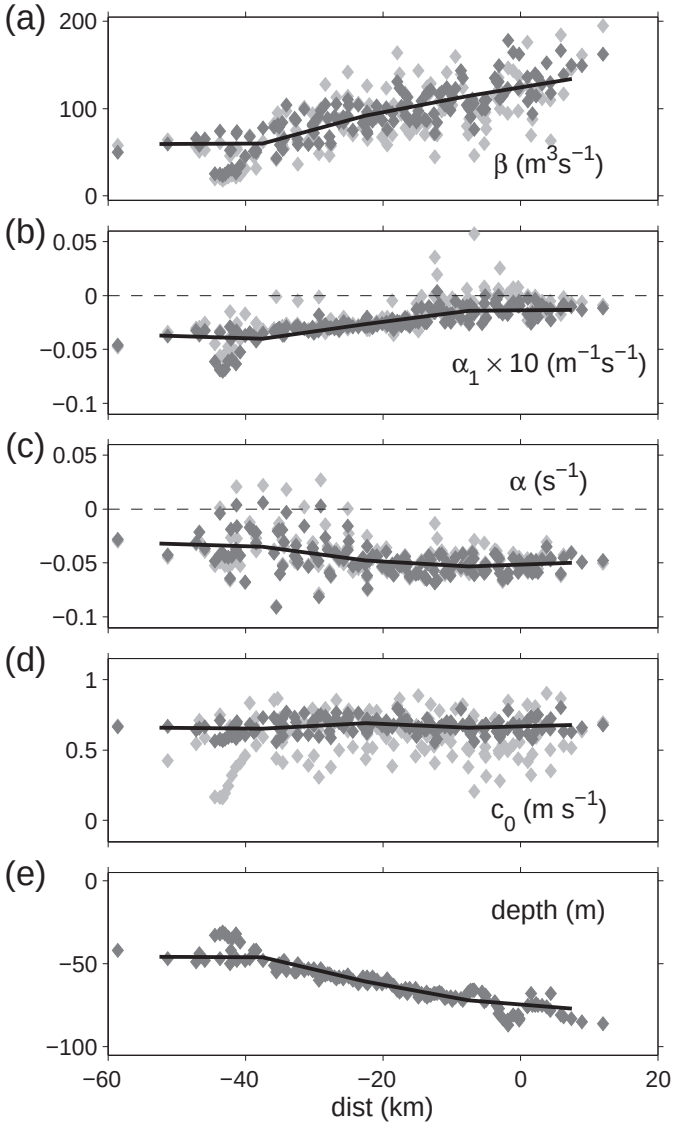


FIGURE 2.6: Summary of KdV parameters. From top to bottom, panels show (a) dispersion coefficients, (b) second-order nonlinear coefficients, (c) first-order nonlinear coefficients, (d) shoreward linear long wave speeds, and (e) bottom depth ahead of each wave profiling series. Calculations were made with/without background shear (dark/light grey diamonds. Variations in $c_0$ calculated with the background velocity include advection by the barotropic, background flow. Black lines show 15 km bin averages of parameters calculated without shear.

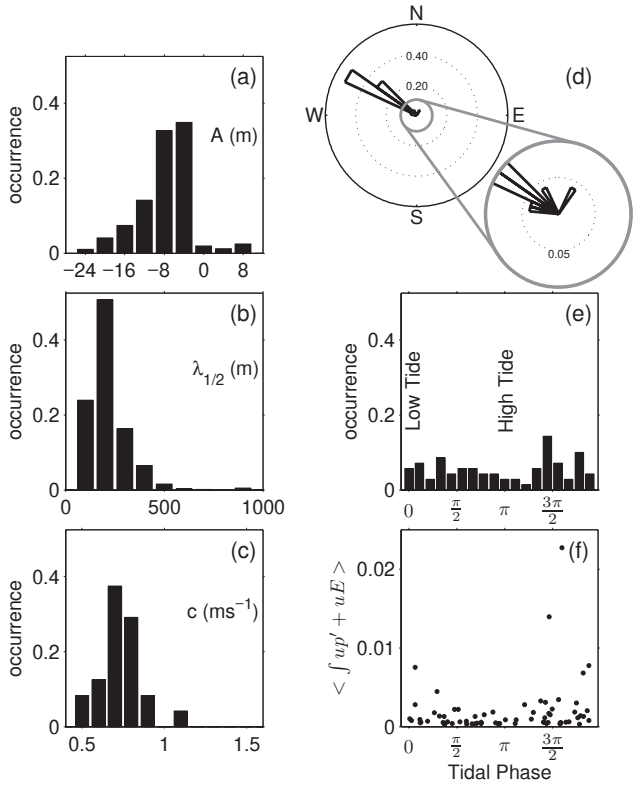


FIGURE 2.7: Summary of wave properties. Histograms of (a) displacement amplitude, (b) half-width, (c) average shoreward wave speed, (d) wave heading, (e) wave arrival times at SW30 relative to the local barotropic tidal height, and (f) average energy flux as a function of tidal phase (low tide corresponds to zero). Panels a-d are calculated from shipboard data; panels e-f are calculated using mooring data from SW30.

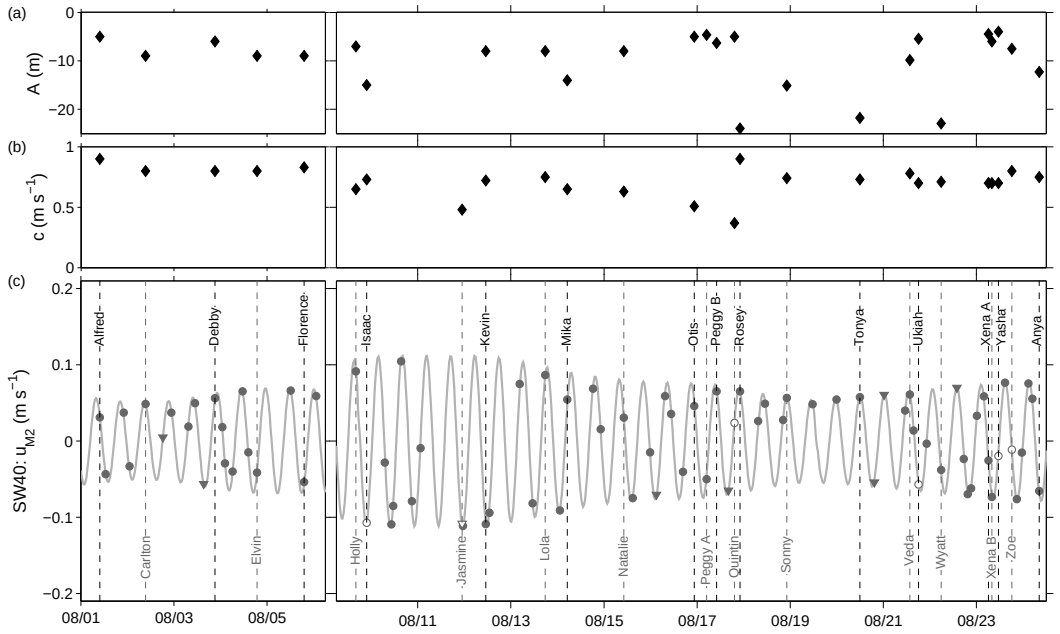


FIGURE 2.8: Tidal height, arrival times, amplitude, and wave speed. Maximum magnitude of (a) wave displacement amplitude and (b) average wave speed of ship-tracked waves. (c) Barotropic $u_{M2}$ at a shelf-break mooring (SW40) with arrival times of mode-1 (circles) and mode-2 (triangles) NLIWs observed at SW30. Waves tracked from the ship are named. Open markers indicate ship-tracked waves that do not appear in the mooring record; for these six waves, arrival times are projections based on the closest observation point and the measured wave speed. The ship returned to port from the 6–9 August; since no waves were tracked during this period, it is excluded for aesthetic reasons.

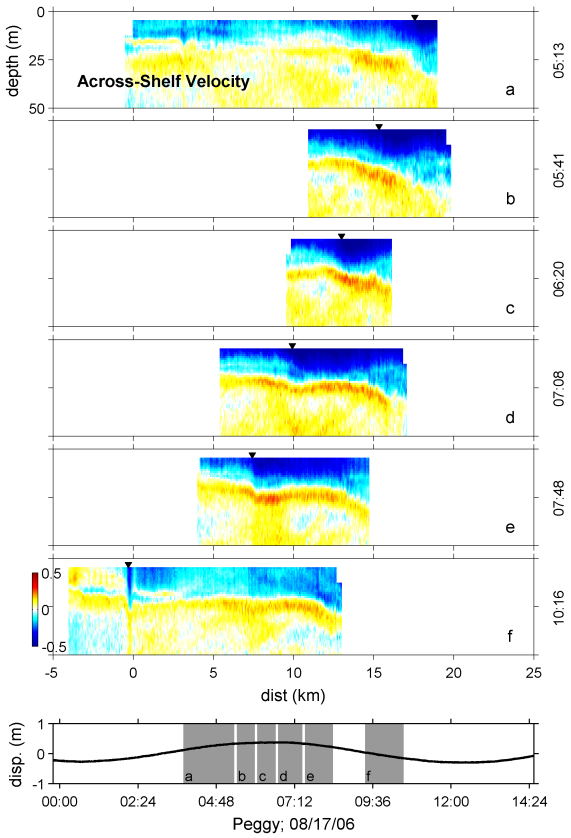


FIGURE 2.9: Tide steepening and wave formation. (a-f) Transects of across-shelf, baroclinic velocity plotted as a function of distance. The bottom panel shows tidal height at SW30 (0 km), time periods of transects are shaded in grey.

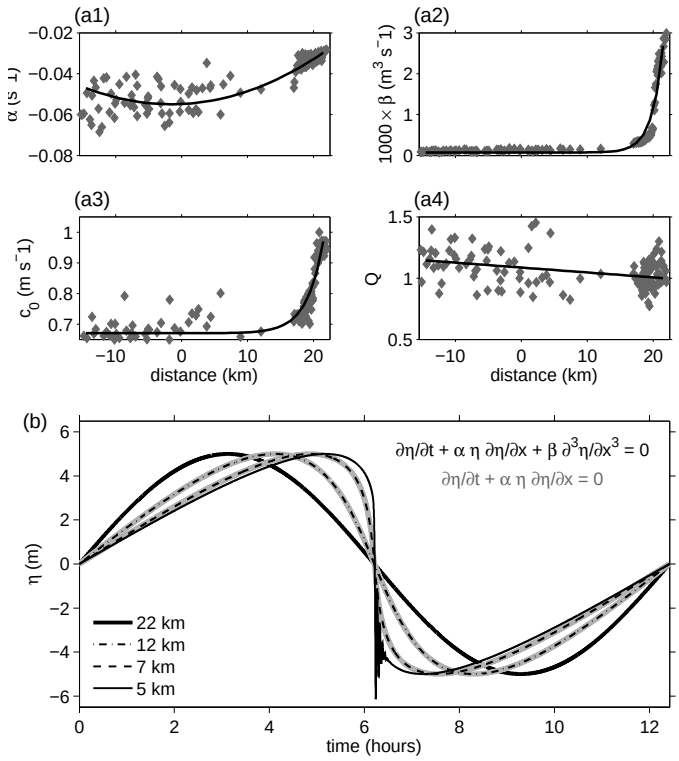


FIGURE 2.10: KdV-based model of wave formation. (a) KdV coefficients (grey diamonds) and empirical fits (black lines) extended onto the slope. (b) Modeled displacements of an initial sine wave (thick black line) with M2 frequency across the outer shelf. For the solution at 7 and 12 km, two cases are shown: the first with dispersion (black) and the second without dispersion (grey).

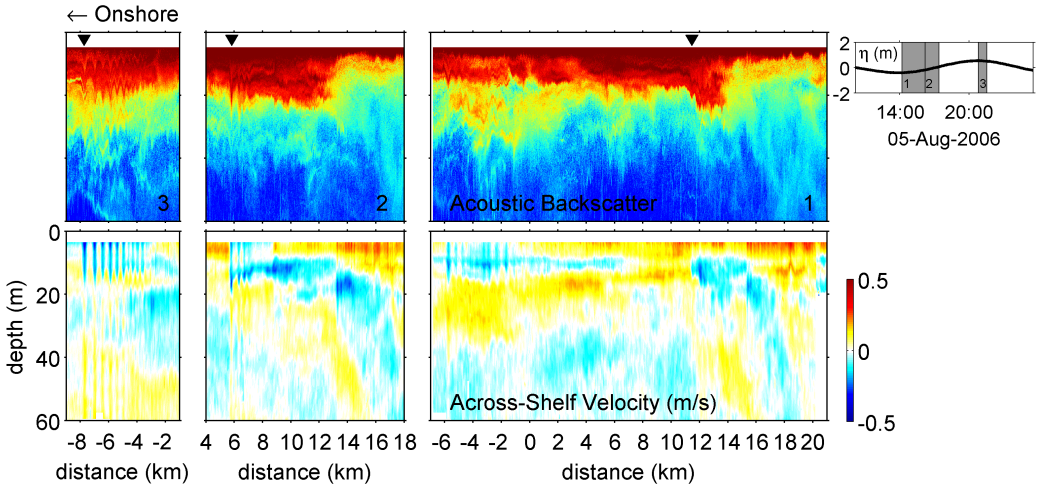


FIGURE 2.11: A more complicated example of wave formation. Transects of acoustic backscatter (top panels) and across-shelf, baroclinic velocity (bottom panels). In time, the first transect is on the far right and the final transect is on the far left. Tidal height at SW30 is plotted in the upper right panel, and transects are shaded in grey. Wave/bore locations are indicated by black triangles.

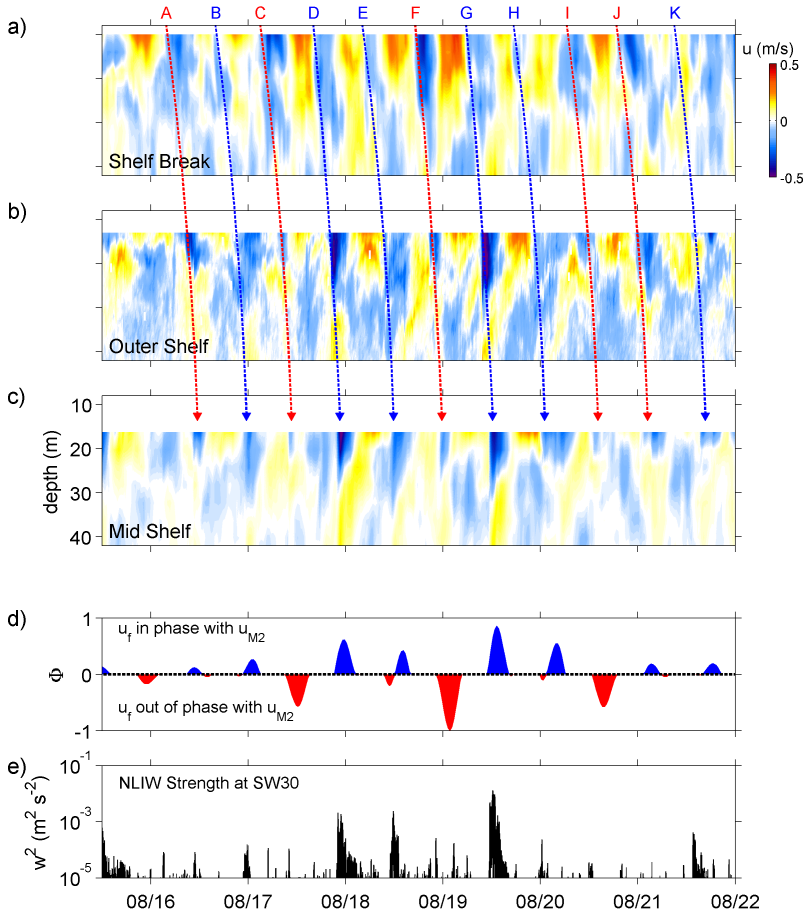


FIGURE 2.12: Modulation of the tide by near-inertial waves. Across-shelf, baroclinic velocity (30 min. bin averages) at (a) SW42, (b) an outer-shelf mooring (7 km) provided by Glen Gawarkiewicz[1], and (c) SW30 for the period of large waves. Onshore M2 pulses are tracked through the mooring line with the dashed arrows, colors are used to distinguish between pulses that increased/decreased in strength (blue/red) as the tide propagated onshore. (d) *Phi*, the interference between the M2 tide and inertial waves at SW30. (e) The square of the depth mean vertical velocity at SW30 ($w^2$), which is a proxy for NLIW energy.

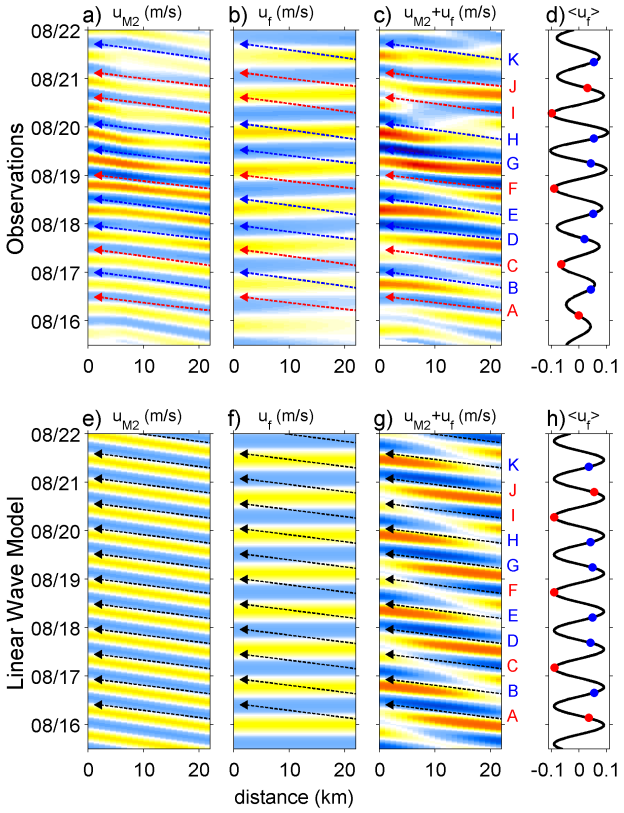


FIGURE 2.13: Distance-time plots of near-surface, across-shelf velocity components, $u_{M2}$ (a,e), $u_f$ (b,f), and $u_f + u_{M2}$ (c,g) for observed, harmonic series (a–c) and modeled, linear waves (e–g). Waves A–K (Fig. 2.12) are traced across the shelf (c,g), and are color-coded in accordance with Fig. 2.12. The across-shelf averages of near-surface $u_f$ are plotted in (d,h). Colored circled correspond to times when the M2 flow shifted onshore near the shelf break at 18 km.

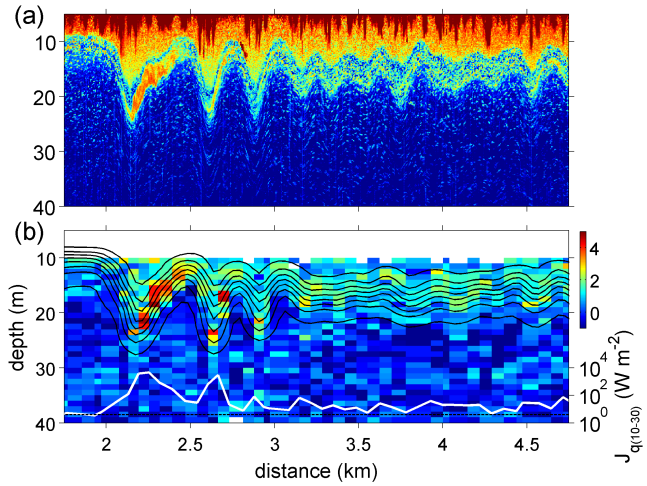


FIGURE 2.14: [Heat flux in *Wave Mika*. (a) Acoustic backscatter through *Mika* and (b) the measured $\log_{10} J_q$ with isopycnals, [21.5, 22.5, 23.5] kg m$^{-3}$, contoured in black. Lower right hand axes shows $J_{q(10-30)}$, which is defined as the average of $J_q$ from 10 to 30 m.

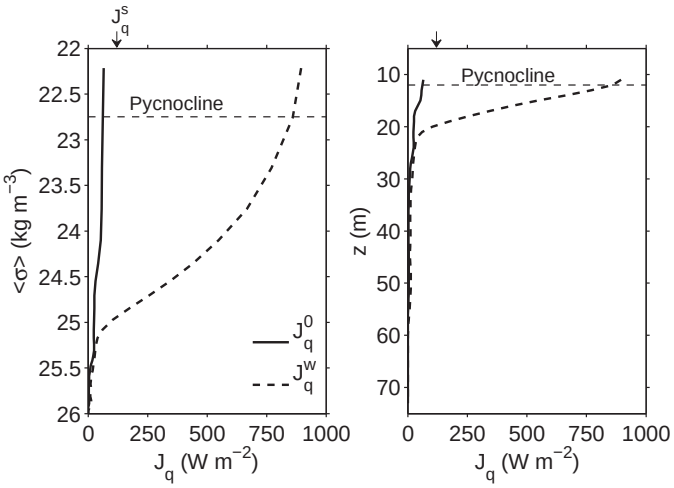


FIGUR E 2.15: (a) Average downward heat flux profiles as a function of density through waves (dashed line) and in background (solid line). Background conditions are based on profiles taken just prior to wave groups, and a 24 hour stationary profiling series with periods of waves removed. Average surface heat flux is indicated by the black triangle. (b) Same as in panel (a), but plotted as a function of depth. Profiles have been filtered to include scales larger the 7 m.

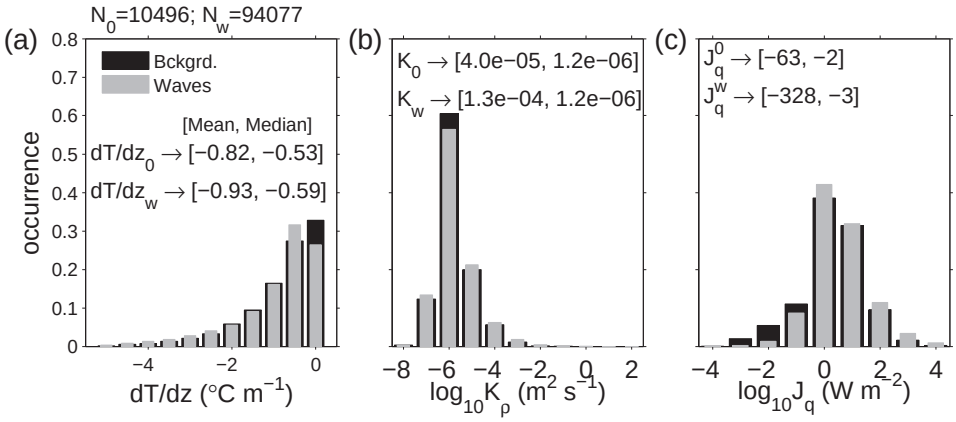


FIGURE 2.16: Histograms of (a) $dT/dz$, (b) $K_\rho$, and (c) $J_q$ for background (black) and wave (grey) conditions. Mean and median values are given for each quantity. These values are those used to create average vertical profiles of $J_q$ (Fig. 2.15).

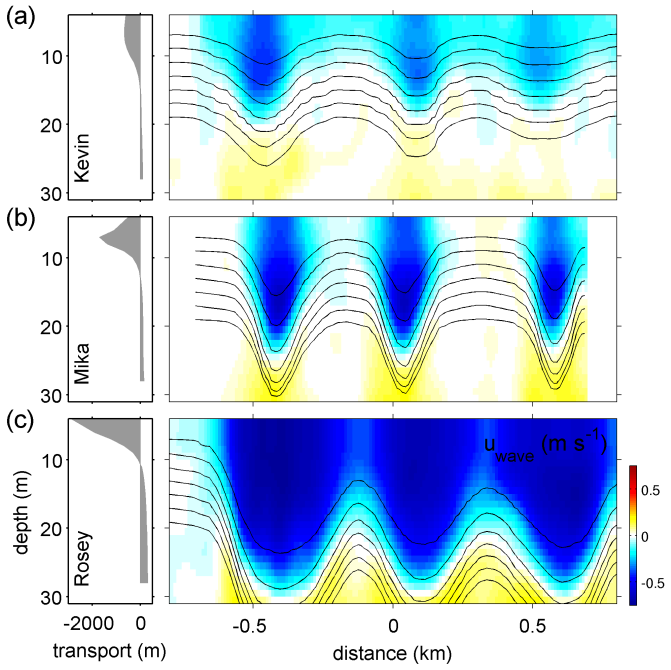


FIGURE 2.17: Three examples of particle transport in waves. Left panels show particle transport as a function of initial particle depth for leading three waves. Right panels show the across-shelf velocity with isopycnals originating at z= (7, 9, 11,. . . , 19) m contoured on top for threes different wave trains, (a) *Kevin* at -15.25 km, (b) *Mika* at -27.5 km, and (c) *Rosey* at -7.25 km. Negative transports are directed shoreward.

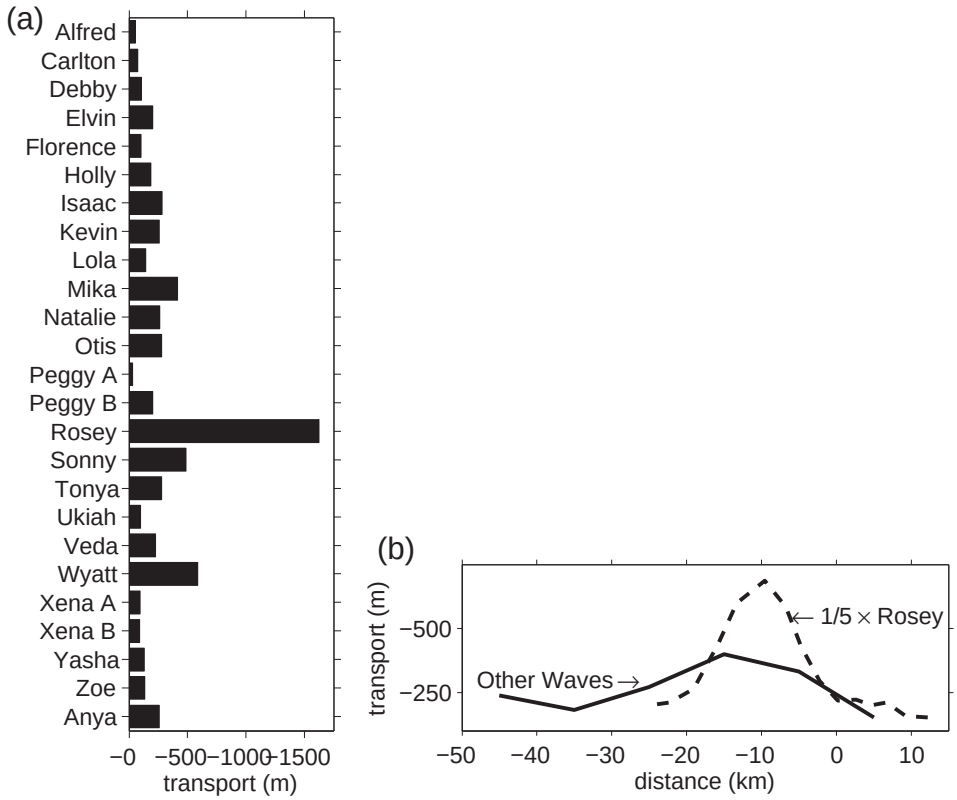


FIGURE 2.18: (a) The average, measured surface transport of the three leading waves for each mode-1 wave group observed from the ship platform. Note that the averages are made over a variety of time ($\mathcal{O}$(1 hr to 1 day)) and spatial ($\mathcal{O}$(1–50 km)) scales depending on the length of time a particular wave group was transited. (b) Solid black line shows the ten-kilometer bin averages for all waves excluding *Rosey*. Dashed line shows *Rosey's* transports divided by 5.

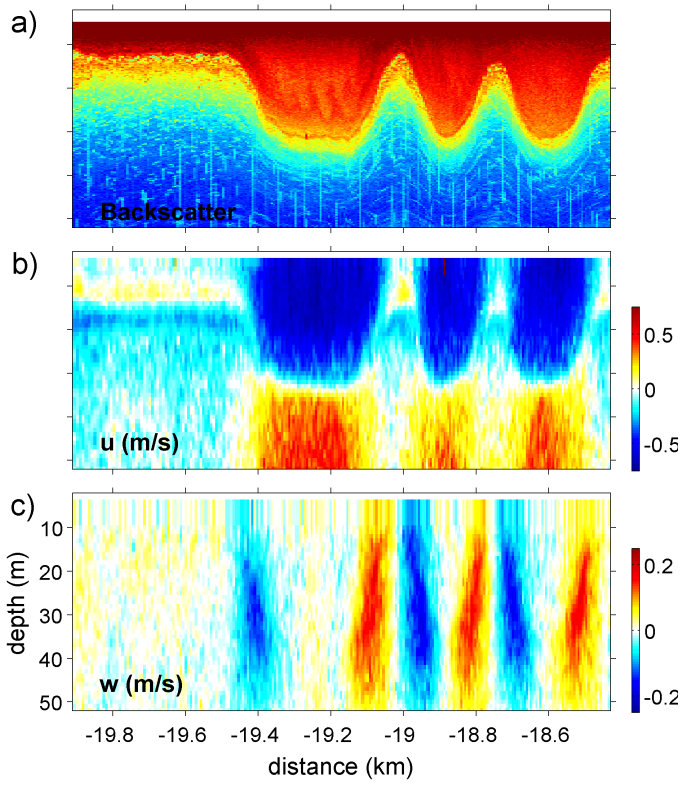


FIGURE 2.19: (a) Backscatter, (b) across-shelf velocity, and (c) vertical velocity for *Wave Rosey* at 0400 UTC 18 August 2006.

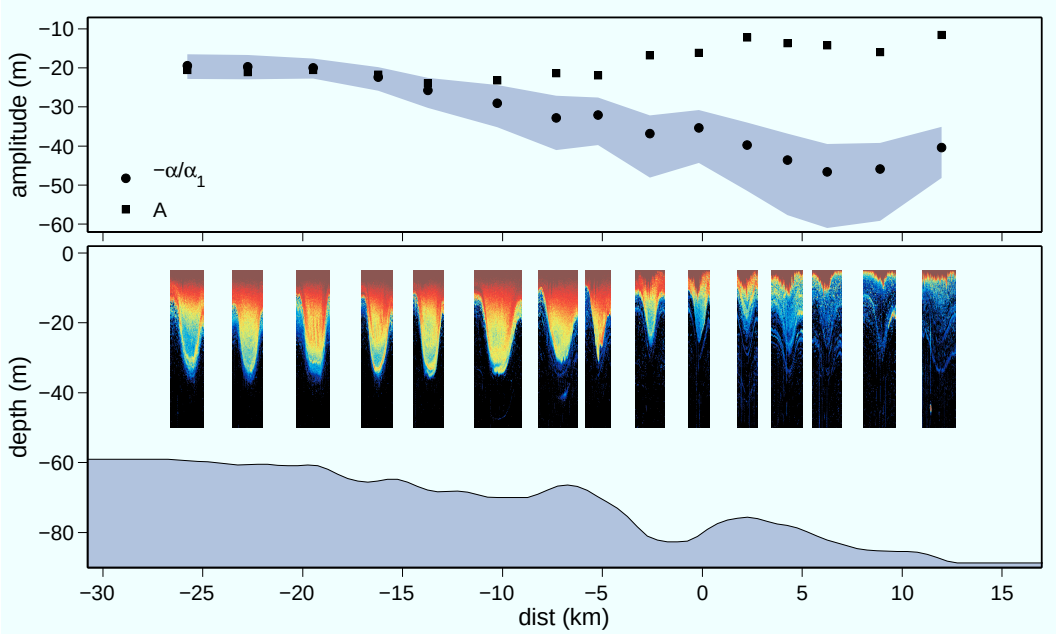


FIGURE 2.20: *Rosey*– an amplitude-limited wave. (a) Black circles show the limiting amplitude as defined by second-order KdV analysis. The grey cloud represents limits assuming the depth is known to within ±2 m. Black squares show measured displacement amplitude of lead wave. (b) Backscatter images of leading waves are plotted across topography. Images are centered at actually wave locations. Depths are true to the vertical axis, and wavelengths have been multiplied by a factor of three.

TABLE 2.1: Table summarizing mooring sensors used in this work.

| Mooring | Type | Depth (m) | Dist. (km) | Location |
|---|---|---|---|---|
| SW29 | water column | 62.5 | -21 | 39º 7.2', 73º 16.6' |
| | Temperature | 1, 12, 21, 31, 42, 55, 60 | | |
| | Conductivity | 12, 31, 55 | | |
| | ADCP | 55 | | |
| | Tide Gauge | 55 | | |
| SW30 | water column | 86 | 0 | 39º 1.5', 73º 4.0' |
| | Temperature | 14, 17, 21, 26, 33, 40, 48, 57, 66, 75, 83.3 | | |
| | Conductivity | 14, 17, 21, 26, 33, 40, 48, 57, 66, 75 | | |
| | 300 kHz ADCP | 75 | | |
| SW34 | water column | 124 | 19 | 38º 56.4', 72º 52.6' |
| | Temperature | 1, 12, 21, 31, 42, 53, 64, 75, 86, 97, 106, 118, 121.5 | | |
| | Conductivity | 12, 31, 53, 75, 97, 118 | | |
| SW37 | bottom Lander | 72 | -10 | 39º 4.1', 73º 10.1' |
| | Conductivity/Temperature | | | |
| | Pressure (ppod) | | | |
| | ADP | | | |
| SW38 | bottom Lander | 79 | 1 | 39º 1.2', 73º 3.4' |
| | Conductivity/Temperature | Surface reflection resulted in bad data | | |
| | Pressure | from 40-70 m depth. | | |
| | ADCP | | | |
| SW40 | bottom Lander | 127.5 | 19 | 38º 56.2', 72º 52.6' |
| | Conductivity/Temperature | | | |
| | ADCP | | | |
| SW41 | water column | 114 | 17 | 38º 56.9', 72º 53.7' |
| | Temperature | 11, 16, 22, 30, 39, 48, 59, 70, 81, 93, 105 | | |
| | Conductivity | 16, 30, 48, 70, 93 | | |
| SW42 | water column | 175 | 20 | 38º 56.1', 72º 52.0' |
| | Temperature | 11, 19, 30, 42, 56, 72, 89, 108, 128, 149, 170 | | |
| | Conductivity | 19, 42, 72, 108, 149 | | |
| | 300 kHz ADCP | 149 | | |
| SW43 | water column | 480 | 22 | 38º 55.6', 72º 50.7' |
| | Temperature | 22.5, 31.5, 41.5, 51.5, 66.5, 89.5, 112.5, 140.5, 169.5, 199.5, 230.5, 262.5, 295.5, 329.5, 364.5, 399.5, 435.5, 472.5 | | |
| | Conductivity | 31.5, 41.5, 66.5, 112.5, 169.5, 230.5, 295.5, 364.5, 435.5 | | |
| | 75 kHz ADCP | 435.5 | | |
| SW47 | water column | 58 | -29 | 39º 9.2', 73º 21.5' |
| | Temperature | 1, 14, 20, 25, 30, 35, 40, 55.5 | | |

# 3 MODE-2 WAVES ON THE CONTINENTAL SHELF: EPHEMERAL COMPONENTS OF THE NONLINEAR INTERNAL WAVE FIELD

Emily L. Shroyer, James N. Moum, Jonathan D. Nash

Journal of Geophysical Research–Oceans

2000 Florida Avenue, NW Washington, DC 20009

submitted

## Abstract

Shoreward-propagating, mode-2 nonlinear waves appear sporadically in mooring records made off the coast of New Jersey in the summer 2006. Our inability to track individual mode-2 packets large distance through the mooring array combined with detailed observations from a ship suggest that these higher mode waves are short-lived. The evolution of the ship-tracked wave group was recorded using acoustic backscatter, ADCP, and turbulence profiling. The leading mode-2 wave was observed to rapidly change form and developed a tail of short, small-amplitude, mode-1 waves. The wavelength of the mode-1 oscillations agreed with that expected for a co-propagating tail based on linear theory. Turbulent dissipation in the mixed layer and radiation of the short, mode-1 waves contributed to large, rapid losses of energy in the leading mode-2 wave, consistent with the observed decay rate and short life span of only a few hours. The energy in the leading mode-2 wave was 10–100 times smaller than the energy of mode-1 nonlinear internal waves observed during the experiment; whereas, the magnitudes of wave-driven turbulent dissipation were similar.

## 3.1 Introduction

Nonlinear internal waves (NLIWs) are commonly seen in the coastal ocean. The bulk of observations consist of waves of depression, perhaps due to the relative ease of distinguishing these features using remote imagery (Jackson, 2004). However, several studies also document waves of elevation (e.g., Klymak and Moum, 2003; Orr and Mignerey, 2003; Scotti and Pineda, 2004; Moum and Smyth, 2006). The terms, NLIWs of depression and elevation, automatically imply a mode-1 structure, in which all isopycnals are displaced in the same direction. Mode-2 nonlinear internal

waves have also been observed in the ocean (Farmer and Smith 1980, see Fig. 2 of Akylas and Grimshaw, 1992; Duda et al., 2004; Bogucki et al., 2005) and in the laboratory (Davis and Acrivos, 1967; Helfrich and Melville, 1986; Hüttemann and Hutter, 2001; Mehta et al., 2002). These higher mode waves are of two types. Either upper isopycnals are displaced upward and lower isopycnals are displaced downward, or the opposite is true. The first type of mode-2 wave is sometimes referred to as varicose emphasizing the bulging shape; the observations presented here are of this type.

Several studies highlight potential mechanisms for the formation of mode-2 NLIWs. For example, Helfrich and Melville (1986) found that a mode-2 wave may emerge after a shoaling, first baroclinic mode wave undergoes a breaking instability, while Hüttemann and Hutter (2001) and Vlasenko and Hutter (2001) describe the formation of reflected and transmitted mode-2 waves after a mode-1 wave encounters a sill. A separate modeling study generated mode-2 waves via resonant interaction of a depth-independent velocity field with topography, where the background velocity is set near the mode-2 linear wave speed (Stastna and Peltier, 2005). These first three examples involve differing topographic interactions, which may not always be necessary. Both Maxworthy (1980) and Mehta et al. (2002) produced mode-2 waves at the head of gravity intrusions in lab studies.

Theoretical studies and numerical models have been employed to study the structure and form of mode-2 nonlinear waves (Davis and Acrivos, 1967; Tung et al., 1982; Akylas and Grimshaw, 1992; Vanden-Broeck and Turner, 1992; Stastna and Peltier, 2005). A noteworthy characteristic of mode-2 waves is the development of an oscillatory wave tail, which consists of a series of short, linear, mode-1 waves. Mode-2 waves are not unique in this respect, and in theory a leading nonlinear wave of arbitrary mode number greater than one may develop a tail composed of lower mode waves (Akylas and Grimshaw, 1992). The growth of the tail is related to

wave speed dependence on vertical mode number and horizontal wavelength. For example, consider again the case of a mode-2 nonlinear wave. Since internal wave speed increases with wavelength and decreases with mode number, short, mode-1 waves may travel at the same speed as long, mode-2 waves for a given background state. The resonance condition, at which the short, mode-1 wave speed is equal to the wave speed of the long, mode-2 wave (i.e., $c_1 = c_2'$, where $c_1$ is the linear, first baroclinic mode wave speed and $c_2'$ is the nonlinear mode-2 speed), results in co-propagation of wave forms and permits growth of the oscillatory, mode-1 wave tail. This growth comes at the expense of the nonlinear wave's energy. We distinguish the wave speed of mode-2 waves from the short, mode-1 tail with the appropriate subscripts. Measured, nonlinear wave speeds are primed.

While the mode-2 wave with its tail is not a soliton in the strict definition, as it is neither steady (radiative loss to the wave tail) nor solitary, the wave form is sometimes referred to as a weakly non-local solitary wave or generalized solitary wave (e.g., Boyd, 1990; Vanden-Broeck and Turner, 1992). These terms are not limited to mode-2 internal waves, as generalized solitary wave solutions exist for equations governing gravity-capillary solitary waves (Hunter and Vanden-Broeck, 1983) and nonlinear Rossby waves (Williams and Wilson, 1988). The development of a resonant tail is distinct from transient, dispersive wave tails, which may form as a wave evolves, in that the tail and NLIW travel at the same speed (i.e., co-propagate). The observations presented here show a mode-1 wave tail that forms some time after the first sighting of the mode-2 wave group, and as such there is some question as to whether the observed tail is an artifact of resonance or dispersion.

In the following we investigate mooring- and ship-based observations of mode-2 waves recorded during the Office of Naval Research's NonLinear Internal Wave Initiative/Shallow Water '06 Experiment (*NLIWI/SW06*) on the New Jersey shelf. This note begins with a review of the experiment in section 3.2, followed by a de-

scription of the observed waves in section 3.3. The structure and energetics of the ship-based observations are detailed in sections 3.4 and 3.5, respectively. Possible generation mechanisms are discussed in section 3.6, followed by a summary (section 3.7). To aid the reader, we point out a subtlety of the terminology used in this manuscript. We occasionally compare the mode-2 nonlinear waves with other, nonlinear, long mode-1 waves that were documented during SW06. These mode-1 NLIWs are distinct from the short, linear mode-1 waves that comprise the tail. We have been careful to refer to these waves as large-amplitude or nonlinear, and hopefully the distinction between theses two types of mode-1 waves will be clear to the reader.

## 3.2 Experimental Details

As part of *NLIWI/SW06* (Tang et al., 2007), a shipboard survey of New Jersey's nonlinear wave field was conducted in August 2006. The R/V Oceanus was equipped with a 120 kHz echosounder, a side-mounted RD Instruments (RDI) 1200 kHz acoustic Doppler current profiler (ADCP) and a hull-mounted RDI 300 kHz ADCP. These shipboard acoustics, combined with the ship's X-band radar and visual sightings, were used to locate and track shoreward propagating wave groups. Wave groups were transited through at 3–4 m $s^{-1}$ from the back to leading wave; at which point the ship was turned and held stationary. As the wave propagated past the ship, microstructure measurements (density and turbulent dissipation) were collected using the Chameleon profiler (Moum et al., 1995). Typically the first three to four waves passed the ship, before the ship was turned and the process repeated. Shipboard observations of 27 wave groups were obtained. One particular wave group consisted of mode-2 waves, the focus of this analysis.

The shipboard survey coincided with a large-scale mooring deployment (Fig.

3.1). Two environmental moorings, SW30 and SW38, were located 1 km apart near the 80 m isobath, and 8 groups of mode-2 waves were identified in these mooring records over the course of a month. SW30 was a water column mooring equipped to measure both density and velocity with CTD sensors located at 14, 17, 21, 26, 33, 40, 48, 57, 66, and 75 m and upward-facing ADCP sampling 4-m vertical bins every 30 s. SW38 was a bottom lander with an upward facing RDI 300 kHz ADCP that sampled 1-m bins every 5 s. Lower-frequency mode-2 oscillations were evident in the velocity record at the nearest offshore mooring (SW40), but we could not distinguish any mode-2 NLIWs in this record. The nearest onshore mooring (SW37, located 10 km inshore of SW30) was a bottom lander similar in set-up to SW38. No mode-2 waves were identified in its velocity record. The nearest, onshore water-column temperature sensors (located at 1, 12, 21, 31, 42, 55, and 60 m) were on SW29, which was positioned 20 km inshore of SW30. From this temperature record we isolated only two sets of mode-2 waves. SW29 was also equipped with a bottom mounted ADCP sampling with a set-up identical to SW30. For further details on the tracking experiment and mooring set-up, the reader is referred to Shroyer et al. (2009c).

## 3.3 Observations

### 3.3.1 Mooring Record

Mode-2 wave trains were discernible in the temperature and velocity data recorded at mooring SW30 (located at the x–y origin in Fig. 3.1). While the nearby bottom lander, SW38, was equipped to better resolve water column velocities, distinguishing mode-2 waves from the velocity record is difficult due to side-lobe contamination of near-surface velocity data and energetic background shear. Therefore, we rely on the temperature record at SW30 to identify mode-2 waves and then

project these times backward to help identify the mode-2 waves in the SW38 velocity record. Mode-2 wave properties are summarized in Table 3.1. The fourth group was observed at SW30, but not in the SW38 record.

Wave groups detected at SW30 were comprised of 2–6 waves. We were unable to identify lower mode tails in the mooring records, a possible result of a relatively coarse sampling scheme. Ideally amplitudes should be calculated using maximum displacements, but the limited vertical resolution of the mooring CTD data precludes such an approach. Instead, amplitudes ($A$) were calculated in the following manner. First, temperature records were converted to displacements ($\eta$) using the relation,

$$\eta = \frac{\theta'}{\overline{\partial\theta/\partial z}}$$

at sensors located at 14 m and 26 m depths. Here, $\theta'$ is the perturbation temperature and $\overline{\partial\theta/\partial z}$ is a time-averaged, vertical gradient of temperature at each sensor. The 14-m sensor provided the closest available measurement to the surface. In all but one case, this upper sensor recorded upward displacements, and the lower sensor recorded downward displacements through mode-2 waves. The amplitude was then computed as $A = 1/2 \times (|\eta_{14m}| + |\eta_{26m}|)$. For the eighth wave group, the 14 m sensor only recorded upward displacements in the leading wave. $\eta_{14m}$ of the trailing waves was negligible, indicating that the sensor was possibly in the midst of the pycnocline. The amplitude in these waves was assumed to be equal to $A = |\eta_{26m}|$. $A$ varied from 1.6 m to 7.5 m, with an average of 4.1 m. These magnitudes are similar to those obtained from full-depth profiles for the ship-tracked wave group.

The wave period, $T$, was calculated as the amount of time that $\eta_{14}$ was greater than zero through each disturbance. $T$ was on average 8 minutes. The shortest wave periods were approximately 4 minutes, and larger values of $T$ were near 13 minutes. The observed, mode-2 wave speeds, $c_2'$, were calculated as $c_2' = \Delta x/\Delta t$

between SW38 and SW30, and therefore include advection by the background current. In contrast to the convention used for measured velocities (with negative $u$ directed onshore), positive values of $c_2'$ are directed shoreward. The average $c_2'$ is 0.39 m s$^{-1}$ with a propagation direction of 300°. In an attempt to adjust for advection, depth-mean velocities at SW30 were averaged for the hour preceding wave arrival to estimate a barotropic velocity. For the majority of waves, the corrected wave speed, $c_2^*$, centers around 0.4 m s$^{-1}$ with $c_2^*$ near 0.3 m s$^{-1}$ for two of the wave groups. The wave heading was calculated assuming that the variance in the along-crest dimension should be minimized. Arrival times of the mode-2 waves were not clearly linked to the M2 barotropic tide, which was calculated using a harmonic fit to velocity data. Arrival times relative to the peak ebb varied from 5.7 hours to just under 12 hours, and arrival times relative to the previous mode-1 wave group show an even larger spread with time lags from 2.5 to 12.5 hours.

Two additional mode-2 wave groups were recorded in the temperature and velocity records at SW29, located inshore another 20 km from SW30. Both groups propagated onshore at 300°. The first, which was observed at 1400 UTC 7 August 2006, propagated into a strong offshore flow whose magnitude was approximately equal to the onshore, wave particle velocities ($\sim$ 0.15 m s$^{-1}$). This wave group consisted of a large leading wave ($T$ = 10 minutes, $A$ = 7 m), and a weak trailing wave with amplitudes and particle velocities less than half of the leading wave. The second wave group was observed at 0925 UTC 26 August 2006 and consisted of four mode-2 waves with periods near 5 minutes and amplitudes ranging from 3–7 m. Neither of these wave groups were apparent in the records from SW30/SW38. Amplitudes were calculated as described above for SW30, but using sensors located at 12 and 31 m-depth. Observed wave speeds were not calculated for the SW29 waves, since we were not able to track the wave groups between moorings.

### 3.3.2 Shipboard Record

The mode-2 wave train, referred to as *Wave Jasmine*, was encountered on 2105 UTC 11 August 2006 at 38.95°N, 72.92°W. (A naming convention was adopted for ship-tracked waves; we use the name here so that comparisons may be made with Shroyer et al. 2009c.) We profiled through *Jasmine* three times (Fig. 3.1; stars), before the wave's signature was lost at 2315 UTC 11 August 2006. Note that *Jasmine* was not observed in SW30, which is consistent with the loss of the shipboard signal 10 km farther offshore. Unlike most mode-1 depression waves, *Jasmine* lacked a surface signature (either visible or in X-band radar), presumably due to reduced surface convergence and divergence. The wave group was tracked in the direction of wave propagation, 300°, calculated by minimizing the along wave front component of particle velocity. The direction coincided with the principal propagation direction of other, large-amplitude, mode-1 wave groups.

During the first and second profiling periods, *Jasmine* consisted of three mode-2 waves (Fig. 3.2a and b). In the third transect a sequence of relatively short, mode-1 waves developed in the wakes of the first two mode-2 waves (Fig. 3.2c). During this final transect, the bottom interface of the second wave was distorted, possibly as a consequence of the leading wave's tail, and the third mode-2 wave was no longer apparent. The wavelength ($\lambda$) of the leading wave decreased from about 180 m to 120 m; in contrast, the shorter mode-1 waves had wavelengths near 60 m. The amplitude, defined by taking $(|\eta_{top}| + |\eta_{bot}|)/2$, where $\eta_{top/bot}$ is the maximum displacement above/below the pycnocline, was near 4 m in the first and final transect but slightly reduced to 3 m in the second transect. The amplitude, defined as the displacement from the mid-line to the peak, of the trailing mode-1 waves was about 1 m.

Using the difference in distance and time between the three profiling periods,

an average wave speed of $\overline{c_2'} = 0.48$ m s$^{-1}$ is estimated. This value is slightly larger than the mode-2 linear phase speed, $c_2$, calculated using the Taylor-Goldstein (T.G.) equation with background shear (e.g., Kundu and Cohen, 2004). $c_2$ increased from 0.40 m s$^{-1}$ at the first profiling site to 0.46 m s$^{-1}$ at the third site. This increase was also observed in the local estimates of $c_2'$ and is attributed primarily to onshore advection by the barotropic current. Background profiles of $\rho_0$ were estimated as averages of a minimum of two profiles taken ahead of the leading wave; background velocity profiles, $u_0(z)$, were calculated by averaging 10 minutes of data ahead of the wave (Fig. 3.3). Both $\rho_0$ and $u_0$ were low-pass filtered in the vertical with a cutoff wavenumber of 0.15 m$^{-1}$.

The background density remained relatively steady during this period, although a general shift toward less dense water onshore existed. The pycnocline centered between $\sim 10 - 20$ m depth spans two near-homogeneous layers located at the surface and at depth. While $u_0$ maintained a consistent overall shape (e.g., the reversal at $\sim$15 m), the exact structure and magnitude of the shear changed. For example, prior to the first crossing the background velocity changed from -0.28 m s$^{-1}$ to 0.02 m s$^{-1}$ in the upper 40 m, while $u_0$ ahead of the third crossing decreased from approximately the same starting value to only -0.13 m s$^{-1}$. The nature of the background shear was quite complicated particularly near the pycnocline, which corresponds to the vertical center of the mode-2 waves.

The general characteristics of the mooring-observed mode-2 waves are consistent with those of *Jasmine*, discussed above. In addition, background profiles of salinity and velocity ahead of some mooring waves are similar to those observed for *Jasmine*; we will look in more detail at the background structure in both the mooring and ship records in section 3.6. However, first the structure and energetics of the leading wave in *Jasmine* are explored in the following two sections. This

extended analysis is possible for the ship-tracked group but not the mooring waves due to 1) the fine vertical resolution provided by Chameleon, 2) the fine horizontal resolution of the acoustic backscatter, and 3) the fact that *Jasmine* was sampled at multiple locations.

## 3.4 Wave Structure

### 3.4.1 Mode-2 Wave Structure

Using shipboard profiles of $\rho_0$ and $u_0$ the linear mode-2 vertical structure function, $\phi_{\text{T.G.}}$, may be compared to the observed vertical structure function, $\phi_{\text{obs.}}$ (Fig. 3.4). Density was averaged into 3 m bins prior to calculating displacements, after which the calculated vertical displacements were re-interpolated onto the original z-grid. $\phi_{\text{obs.}}$ differs from $\phi_{\text{T.G.}}$, particularly in the location of the maximum displacements in the final two transects. In the final transect, the upper and lower horizontal structures of the leading mode-2 wave were not symmetric (Fig. 3.2c), and consequently are more reminiscent of work by Stastna and Peltier (2005) as opposed to modeling efforts which rely on a symmetry plane through the mixed layer (e.g., Tung et al., 1982).

### 3.4.2 Mode-1 Wave Tail

Possibly the most striking feature of the shipboard observations is the sudden appearance of the mode-1 tail in the final transect. While not shown, the tail was fully formed by the time the ship ran back over the wave in between the profiling series shown in Fig. 3.2b and c. Only thirty minutes ($\sim 4.5T$) passed between profiling through the leading wave at 13.4 km and the return transit. The change in wave structure, which was manifested in the decreased wavelength and the development of the short, mode-1 tail, was coincident with changing conditions of the

background fluid between the second and final series. A close examination of Fig. 3.3 reveals an increase in stratification, a contraction of the pycnocline width that is also highlighted by a change in the backscatter return through the pycnocline (Fig. 3.2), and a surfacing of the pycnocline. The background fluid thus shifted to a "more" two-layer stratification as the wave form propagated onshore. The growth of the wave tail could be a product of either transient dispersion, or co-propagation; we take this opportunity to highlight two aspects of the observations that suggest co-propagation via the resonance condition.

- *The leading mode-2 wave form steepened.* The decrease in $\lambda$ between the second and third transect is significant and exceeds reasonable error bounds associated with the correction of the Doppler shift. Note that a reduction of wavelength is the opposite of what would be expected due to barotropic currents, since the wave propagated into a region of increased shoreward flow.

- *The tail is composed of oscillations of a single wavelength.* To offer a more quantitative assessment of this last point, the power spectral density of the backscatter return depth-averaged between 10–15 m ($< \sigma >_{10-15m}$) was calculated through the oscillatory tail sections (black line, Fig. 3.5a). The peak in power occurs at 56 m (Fig. 3.5b); and while there is some energy at large wavelengths, the cut-off is sharp at smaller length scales. This wavelength agrees well with those predicted by the resonance condition, $c_2' = c_1$. Using $\rho_0$ and $u_0$ from the second profiling series, the predicted wavelength is almost identical to the observed wavelength (Fig. 3.5c).

If field conditions were uniform and stationary (as often employed in modeling and laboratory analyses), the evolving form of the leading wave would likely be attributed to dispersion, especially if the evolution occurred in an early wave stage. However, nature provides a complex and rich environment, and the response of

the wave form to variations in density and velocity is not easily confined. For example, the observed surfacing of the mixed layer, and contraction of the transition layer could have resulted in the "more" nonlinear wave form in the final series. We could then attribute the sudden appearance of the mode-1 waves to amplitude growth of a co-propagating tail in response to increased nonlinearity in the mode-2 wave. Modeling studies have noted an analogous response as increased wave nonlinearity, which in these cases is set by amplitude, results in growth of oscillatory tails (Stastna and Peltier, 2005; Williams and Wilson, 1988). The dominance of a single, short wavelength that agrees with the resonance condition further supports this mechanism for tail growth.

The group speed of the mode-1 waves, $c_1^g = \partial\omega/\partial k$, was calculated from the dispersion relation, $\omega(k)$, solved for using the T.G. equation. $c_1^g$ was approximately 0.3 m s$^{-1}$ less than the linear phase speed. Taking the length of the mode-1 tail, $L$, to be the distance between the first and second mode-2 wave (i.e., assuming that only the mode-1 waves ahead of the second mode-2 wave originated from the first mode-2 wave), this difference results in a development time, $\tau = (c_1 - c_1^g) \times L$, of approximately 15 minutes for the mode-1 tail. $\tau$ is consistent with the sudden appearance of the waves within the 30 minutes required to make the return transect. Given this time frame, the lack of multiple wavelengths in the tail further discounts dispersion in favor of co-propagation. We expect that at least some variation in wavelength should exist if dispersion was important, since even very short waves (20m) that travel 0.2 m s$^{-1}$ slower than the mode-2 speed would only lag the leading wave by 350 m in 30 minutes. However, regardless of the mechanism, the radiated wave tail contributes to the evolving energetics of the leading wave.

## 3.5 Energetics

### 3.5.1 Details of Energy Calculation

While the profiling method allows for very fine resolution of the vertical structure (1 m), the horizontal resolution is unfortunately coarse. In order to calculate the available potential energy of the wave, the density structure of the wave was interpolated onto a finer horizontal grid (100 points per wave). Backscatter images were used to obtain a horizontal shape function both above and below the wave's centerline. At each vertical level, a linear regression of the observed density displacements ($\eta$) onto these functions was used to fit the data onto the refined grid. After obtaining this high-resolution displacement field, the density is found by assuming $\rho(z+\eta) = \rho_0(z)$. The interpolated density field agrees well with the measured density at a given location.

The interpolated density field and wave velocity were used to calculate the APE,

$$APE = \int\int (\rho - \rho_*) g z dx dz,$$

and the KE,

$$KE = \int\int \frac{1}{2}\bar{\rho}(u_{wave}^2 + w_{wave}^2) dx dz,$$

in the lead waves. In the previous expressions, $\bar{\rho}$ is the average density, and $\rho_*$ is the reference density, defined by the state of minimum potential energy (Winters et al., 1995; Hebert, 1998). The wave horizontal velocity, $u_{wave}$, was calculated by subtracting $u_0$ along interpolated isopycnals. The integration limits extend across the wavelength and over the entire water column. Evaluating the above expressions through the lead wave in each transect yields total energies, $E = APE + KE$, that decreased from 51 kJ m$^{-1}$ in the first transect to 41 kJ m$^{-1}$ and 33 kJ m$^{-1}$ in the second and final transects, respectively. A schematic summarizing the lead wave

energetics that are detailed below is represented on the right hand side of Fig. 3.2.

### 3.5.2 Dissipative Loss

Approximately forty percent of the leading wave's energy was lost between the first and third crossing, presumably to the combined effects of wave radiation and turbulent kinetic energy (TKE) dissipation, $\epsilon$. Observations show elevated levels of TKE dissipation were present during the first and third transect (refer to Fig. 3.6), increasing from background levels of $10^{-7}\mathrm{m}^2\ \mathrm{s}^{-3}$ up to $10^{-6}\mathrm{m}^2\ \mathrm{s}^{-3}$ and $10^{-5}\mathrm{m}^2\ \mathrm{s}^{-3}$ in the waves. While there was no observed increase in $\epsilon$ through the core of the lead wave during the second transect, the trailing mode-1 wave train that developed before the third crossing exhibited an increase in TKE dissipation from background levels by an order of magnitude. The average dissipative loss, $D$, through each wave was calculated by integrating the measured $\epsilon$ through the core of the lead wave (usually one profile) over the depth of the water column and then multiplying by the wavelength ($\lambda \times \int_0^H \bar{\rho}\epsilon dz$). Values of $\epsilon$ above 10-m depth are discarded due to contamination by the ship wake. We assume that dissipation due to bottom friction is negligible; this assumption seems reasonable since 1) the water column is relatively deep ($\sim$100 m) and 2) wave velocities are small at the bottom.

The resultant estimates of dissipative loss for the leading waves are 10 W $\mathrm{m}^{-1}$ in the first transect, 1 W $\mathrm{m}^{-1}$ in the second transect and 20 W $\mathrm{m}^{-1}$ in the final transect. A sustained dissipative loss equal to the average of these three values (10 W $\mathrm{m}^{-1}$) would deplete the leading wave's energy (51 kJ $\mathrm{m}^{-1}$) in 1.5 hours, corresponding to about $15T$ and a propagation distance of approximately 2.5 km ($\sim 15\lambda$). While in reality turbulent mixing events are episodic in NLIWs, the high values of dissipation that were observed in two of the three profiling periods contributed to the short life-span of *Jasmine*. These estimates of dissipative loss are comparable to typical values for the large-amplitude, long mode-1 waves observed

during *SW06*.

The observed loss in energy per unit time, $dE/dt = 3.5$ W m$^{-1}$, between the first and second crossing is roughly equal to the average dissipative loss ($\sim 5$ W m$^{-1}$) between the first two transects. The change in energy ($\Delta E = 8$ kJ m$^{-1}$) between the second and final transect is approximately equal to that appearing in the trailing mode-1 waves, $E_1 \approx 10$ kJ m$^{-1}$. This value was calculated by integrating the energy between the back edge of the leading mode-2 wave and the front edge of the second mode-2 wave. Energy loss to the radiated mode-1 tail was calculated as

$$D_1 = \frac{d}{dt}\int_z\int_x E_1^* dxdz = (c_1 - c_1^g) \times \int_z E_1^* dz,$$

where $E_1^*$, the energy density of the mode-1 waves in units of J m$^{-3}$, is integrated over the water column. The above expression depends upon the relation $dx = (c_1 - c_1^g)dt$. This calculation results in an estimate of $D_1 \approx 10$ W m$^{-1}$; thus, the magnitude of energy loss to the mode-1 waves is comparable to the dissipative loss.

### 3.5.3 Comments on Wave Energetics

To summarize, it appears that the initial mode-2 wave first loses energy to turbulent mixing, and afterward loses a similar amount of energy to mode-1 wave radiation, assuming all waves between the first two mode-2 waves originated from the leading wave. The large dissipative loss at the third crossing and the assumed continued losses to wave radiation contribute nearly equally to depletion of the mode-2 wave energy. The mixing associated with these waves may play an important role in eroding the barrier established by the pycnocline, especially considering their location centered in the transition layer. Thus these waves, which have 10-100 times less energy than the mode-1 NLIWs observed in the same region, may have a disproportionate, localized effect on the coastal environment and the vertical fluxes

of heat and nutrients. Not dissimilar to open ocean internal waves, in which low modes carry the energy (over large distances), but high modes are associated with dissipation.

## 3.6 Discussion

*Wave Jasmine* evolved quickly over the profiling periods, and the first transect was made after the mode-2 waves were clearly established. Similarly, mooring records are limited to analysis of pre-existing mode-2 wave forms. Consequently, the formation mechanism was not directly observed and is not known for certain. Mooring- and ship-based observations of the mode-2 waves occur inshore of the shelf break over a gradually sloping bottom in a region where the larger mode-1 NLIWs were growing in amplitude; thus, generation by a breaking mode-1 wave as suggested by Helfrich and Melville (1986) is unlikely. Given the steep, variable slope, mode-2 wave generation may be a result of tidal forcing near the shelf break; or, wave formation may be tied to frontal intrusions, as this region is characterized by a complex salinity/temperature field on the shelf. Below we speculate on these two generation pathways.

### 3.6.1 Character of the Wave Guide

The horizontally-averaged salinity and velocity fields for *Jasmine* (Fig. 3.7) show a complicated vertical structure, with an onshore pulse of relatively salty water located near the wave core. The horizontally-averaged velocity (black line), which includes a contribution from the wave, mimics the reversal present in the background velocity (grey line), as if *Jasmine* is possibly "riding" along the shoreward propagating, salty layer. Inshore at SW30, the mode-2 waves were classified into two types, the first of which was characterized by a salinity maximum in the ver-

tical, similar to that exhibited by *Jasmine*. Six of the eight wave groups fit into this "Type 1" category. In three of the six, the salinity maximum corresponded to the wave centerline (as shown in Fig. 3.8a), and in the other three groups, salinity maximums were located slightly below the wave core. The temperature, salinity, across-shelf velocity, and vertical velocity for a wave group illustrating Type-1 features is shown in Fig. 3.8a. For this example, the mode-2 waves were near the front of a sub-surface, shoreward pulse of high salinity water. The vertical structure in salinity and velocity is reminiscent of the background conditions for *Jasmine*. The shear measured ahead of the wave was multi-layered; and while near-surface temperature displacements were not completely resolved, the vertical velocity is mode-2 for the leading four waves.

In contrast, the remaining two wave groups observed at SW30 showed no evidence of salinity intrusions (Fig. 3.8b). For these waves (Type 2), salinity was temporally stationary (neglecting high-frequency perturbations) for at least two hours past the leading wave. The background velocity profile was near-barotropic (at least below 10-m depth); and the temperature and salinity fields co-varied. Limited conductivity measurements at SW29 prohibit classification of the final two mooring wave groups. However, the onshore appearance of the these two wave groups that cannot be tracked back to the offshore moorings points to some on-shelf process driving wave formation. And yet, the lack of a sub-surface, salty maximum for the Type 2 waves combined with the complexities discussed in the following paragraph, prohibit an absolute answer to the formation question.

### 3.6.2 Comments on Formation

The internal tide was highly irregular across the shelf, with spectral peaks occurring not only at M2 frequencies, but higher harmonics as well (M4 and M6). Significant inertial energy was also present, particularly during the second half of

the month, and in general the background shear environment was energetic and complex. Even the arrival times of the long, mode-1 NLIWs were not phased with the M2 tide (Shroyer et al., 2009c). Furthermore, we note that while nonlinear mode-2 waves were not observed at the shelf break moorings, lower frequency mode-2 structures were occasionally apparent. These factors combined to produce a highly variable wave guide and forcing field, making it difficult to rule out tidal generation of mode-2 waves. For example, mode-2 waves could be the consequence of the interplay between tidally-generated mode-1 NLIWS and the complex, vertical shear characteristic of the intrusions. Or possibly, some of the mode-2 waves could have been tidally forced, while others the result of frontal intrusions. However, regardless of whether intrusions directly force mode-2 waves, they likely help to erode the near two-layer stratification that was seen regularly during this experiment, thus paving the way for creation of higher mode waves. The mode-2 wave environment may have been particularly susceptible to these effects, as the 2006 experiment was preceded by a heat wave and intense rain fall increasing the stratification between the warm, fresh surface water and cool, mixed water at depth.

## 3.7 Summary

While the New Jersey nonlinear internal wave field was dominated by mode-1 depression waves during the SW06 experiment, mode-2 waves were also present. The majority of mode-2 wave groups were observed in two mooring records that were 1 km apart near the 80-m isobath; two wave groups that were recorded at the inshore mooring were not documented in the offshore mooring records. All mode-2 waves propagated shoreward, with average amplitudes of 4 m and average wave speeds around 0.4 m $s^{-1}$. Waves occurred irregularly throughout the month-long experiment.

Detailed measurements obtained from the ship-board platform, allowed for a more thorough analysis of the structure and energetics of one wave group. The vertical structure of the tracked, mode-2 waves differed from linear theory; and the observed wave speed was slightly larger than the theoretical, long mode-2 wave speed as expected for nonlinear waves. A mode-1, short-wavelength tail was observed to develop behind the leading mode-2 waves. The wavelength of the oscillations composing the tail was uniform, and is in agreement with that predicted for a co-propagating tail. The energy loss calculated from shipboard measurements was attributed to the radiation of the short, mode-1 waves and turbulent dissipation in the mixed layer. Mode-2 wave dissipations were comparable to large-amplitude, mode-1 NLIW counterparts, however energies were 10-100 times smaller. Consequently, the mode-2 decay time scale was much shorter (a few hours compared to 10s of hours), and the propagation distance smaller (a few km compared to 10s of km).

The inability to track mode-2 waves large distances through the mooring array and the rapid evolution of the ship-tracked wave group suggest that these waves are ephemeral in this variable shelf environment. The short-lived nature of the waves may be a factor in the relatively few observations of these waves in the field, while in reality they could be numerous but difficult to observe. The formation of the mode-2 waves may be related to frontal intrusions, although the link is ambiguous. Nevertheless frontal dynamics likely play a role in setting the stage for higher mode waves by eroding the two-layer stratification present during much of the SW06 experiment. Although beyond the scope of this manuscript, questions surrounding the details of the mode-2 wave formation and the rapidly-evolving structure of the ship-tracked wave could be further addressed using a numerical model. For example, it would be interesting to see if the somewhat subtle changes in background conditions initiate the growth of the mode-1 tail. Additionally, exploring the consequences of

complex, shear fields to propagating mode-1 and mode-2 waves would be of use in interpreting field observations.

## 3.8 Acknowledgments

This work was funded by the Office of Naval Research. We are grateful to the Captain, crew and marine technician of R/V Oceanus, which conducted the shipboard portion of these observations. We acknowledge the assistance of Mike Neeley-Brown, Ray Kreth, Alexander Perlin, Greg Avicola, and Sam Kelly in obtaining the data. We recognize the Captain and crew of the R/V Knorr, along with John Kemp, James Lynch and James Irish who were responsible for the deployment and recovery of the moorings. We also appreciate the comments of Roger Grimshaw and Sam Kelly on an earlier draft of the manuscript.

## Bibliography

Akylas, T., and R. Grimshaw, 1992: Solitary internal waves with oscillatory tails. *J. Fluid Mech.*, **242**, 279–298.

Bogucki, D., L. G. Redekopp, and J. Barth, 2005: Internal solitary waves in the Coastal Mixing and Optics 1996 experiment: modal structure and resuspension. *J. Geophys. Res.*, **110**, doi:10.1029/2003JC002253, C02024.

Boyd, J. P., 1990: A numerical calculation of a weakly non-local solitary wave: the $\phi^4$ breather. *Nonlinearity*, **3**, 177–179.

Davis, R. E., and A. Acrivos, 1967: Solitary internal waves in deep water. *J. Fluid Mech.*, **29**, 593–607.

Duda, T. F., J. F. Lynch, J. D. Irish, R. C. Beardsley, S. R. Ramp, C.-S. Chiu, T. Y. Tang, and Y.-J. Yang, 2004: Internal tide and nonlinear internal wave behavior at the continental slope in the northern South China Sea. *IEEE J. Oceanic Engin.*, **29**, 1105–1130.

Hebert, D., 1998: The available potential energy of an isolated feature. *J. Geophys. Res.*, **93**, 556–564.

Helfrich, K. R., and W. K. Melville, 1986: On long nonlinear internal waves over slope-shelf topography. *J. Fluid Mech.*, **167**, 285–308.

Hunter, J. K., and J.-M. Vanden-Broeck, 1983: Solitary and periodic gravity–capillary waves of finite amplitude. *jfm*, **134**, doi:10.1017/S0022112083003316, 205–219.

Hüttemann, H., and K. Hutter, 2001: Baroclinic solitary water waves in a two-layer system with diffuse interface. *Exper. in Fluids*, **30**, 317–326.

Jackson, C. R., 2004: *An Atlas of Internal Solitary-like Waves and their Properties*. Global Ocean Associates, www.internalwaveatlas.com, second edition.

Klymak, J. M., and J. N. Moum, 2003: Internal solitary waves of elevation advancing on a shoaling shelf. *Geophys. Res. Let.*, **30**, 2045–2048.

Kundu, P. K., and I. M. Cohen, 2004: *Fluid Mechanics*. Elsevier Academic Press, third edition, 484–486 pp.

Maxworthy, T., 1980: On the formation of nonlinear internal waves from the gravitational collapse of mixed regions in two and three dimensions. *J. Fluid Mech.*, **96**, 47–64.

Mehta, A., B. Sutherland, and P. Kyba, 2002: Interfacial gravity currents II: Wave excitation. *Phys. Fluids*, **14**, 3558–3569.

Moum, J. N., M. C. Gregg, R. C. Lien, and M. E. Carr, 1995: Comparison of turbulence kinetic energy dissipation rate estimates from two ocean microstructure profilers. *J. Atmos. Ocean. Tech.*, **12**, 346–366.

Moum, J. N., and W. D. Smyth, 2006: The pressure disturbance of a nonlinear internal wave train. *J. Fluid Mech.*, **558**, 153–177.

Orr, M. H., and P. C. Mignerey, 2003: Nonlinear internal waves in the South China Sea: Observation of the conversion of depression internal waves to elevation waves. *J. Geophys. Res.*, **108**, doi:10.1029/2001JC001163, 3064–3079.

Scotti, A., and J. Pineda, 2004: Observation of very large and steep internal waves of elevation near the Massachusetts coast. *Geophys. Res. Let.*, **31**.

Shroyer, E., J. Moum, and J. Nash, 2009: A description of the nonlinear internal wave field over New Jersey's continental shelf. *J. Geophys. Res.*, **submitted**.

Stastna, M., and W. Peltier, 2005: On the resonant generation of large-amplitude internal solitary waves and solitary-like waves. *J. Fluid Mech.*, **543**, 267–292.

Tang, D. J., and Coauthors, 2007: Shallow Water '06. *Oceanography*, **20**.

Tung, K.-K., T. F. Chan, and T. Kubota, 1982: Large amplitude internal waves of permanent form. *Studies in Applied Mathematics*, **66**, 1–44.

Vanden-Broeck, J., and R. E. L. Turner, 1992: Long periodic internal waves. *Phys. Fluids*, **4**, 1929–1935.

Vlasenko, V., and K. Hutter, 2001: Generation of second mode solitary waves by the interaction of a first mode soliton with a sill. *Nonlinear Processes in Geophysics*, **8**, 223–239.

Williams, G. P., and R. J. Wilson, 1988: The stability and genesis of Rossby vortices. *J. Atmos. Sci.*, **45**, 207–241.

Winters, K., P. Lombard, J. Riley, and E. D'Asaro, 1995: Available potential energy and mixing in density-stratified fluids. *J. Fluid Mech.*, **289**, 115–128.

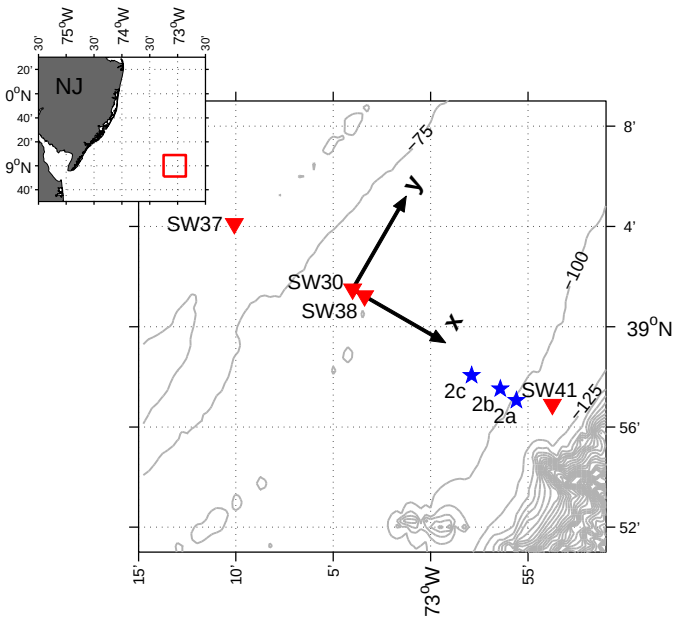


FIGURE 3.1: SW06 Site and Bathymetry. Moorings, SW38 and SW30, that were used in this analysis are shown along with the two nearest, across-shelf environmental moorings, SW37 and SW41 (red triangles). SW29 (not shown) is located 10 km inshore of SW37 along the same mooring line. The blue stars indicate locations of shipboard profiling series through *Wave Jasmine* with reference to Fig. 3.2a, b, and c; and the black axes define the coordinate system.

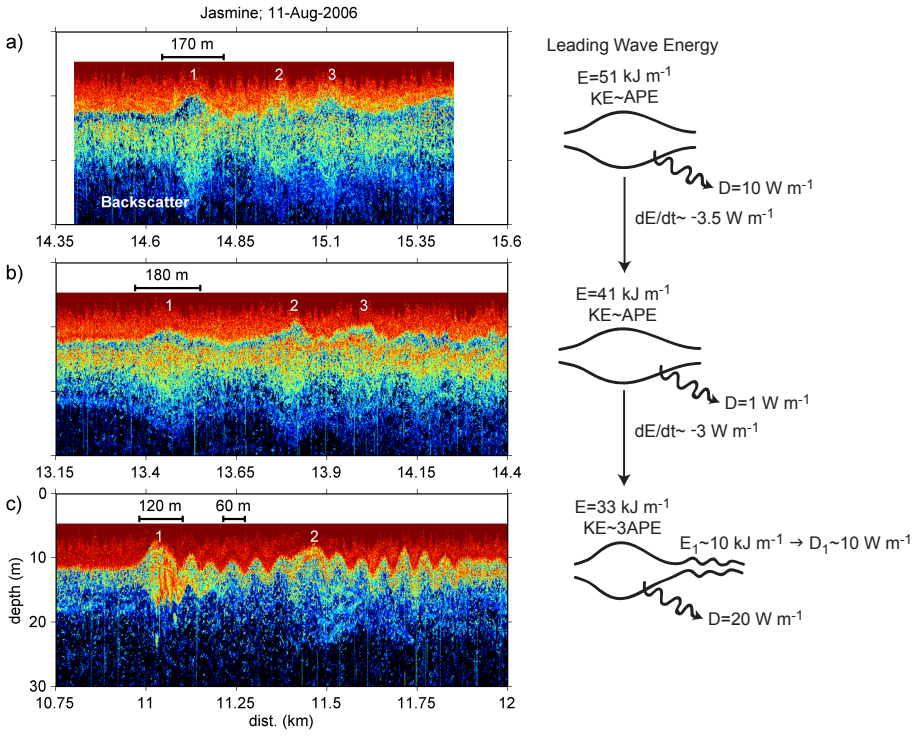


FIGURE 3.2: Right: Acoustic backscatter series for the a) first, b) second, and c) third profiling series through *Wave Jasmine*. Times series have been converted to distances using the wave speed and the axes shown in Fig. 3.1. Waves are propagating to the left. Distances are corrected for the Doppler shift using the ship velocity. Left: Schematic detailing lead wave energetics, which are discussed in section 3.5.

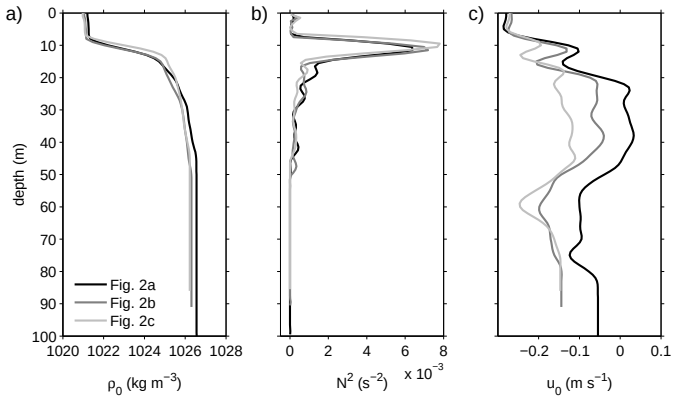


FIGURE 3.3: Background profiles of a) density and b) velocity for the first, second and third profiling series.

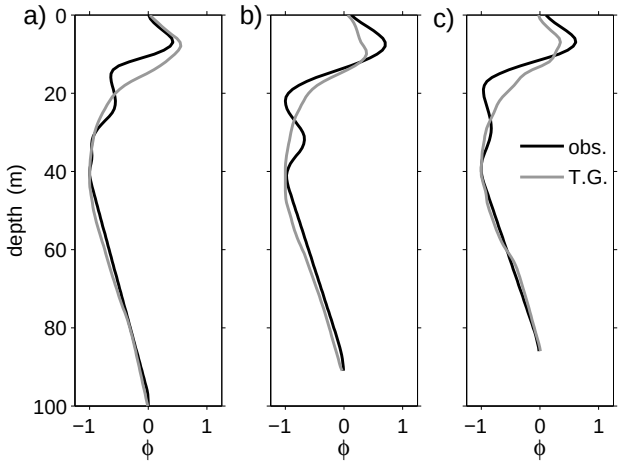


FIGURE 3.4: The observed vertical structure (black) and as calculated by the Taylor Goldstein equation (grey) for the first (a), second (b) and third (c) profiling series for *Wave Jasmine*.

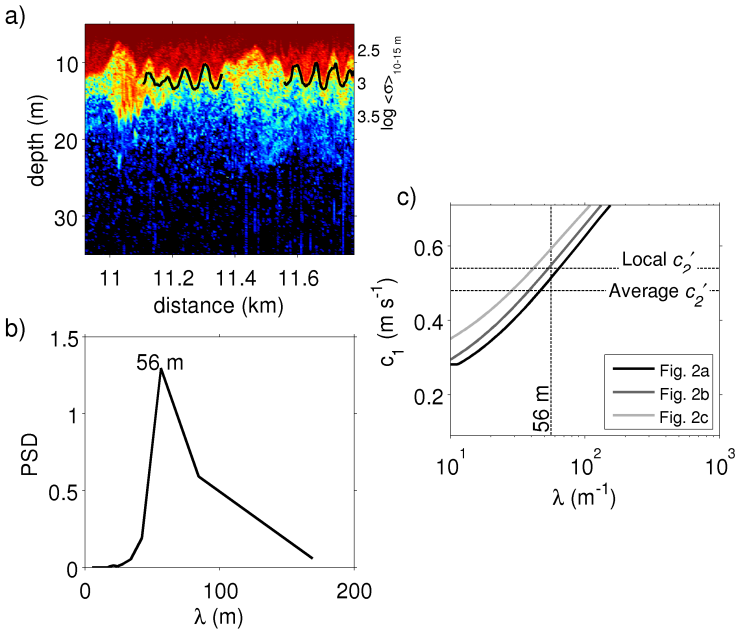


FIGURE 3.5: Criteria for mode-1 wave resonance. a) Acoustic backscatter and b) power spectral density of backscatter return averaged between 10–15 m. Wave tails were isolated (black overlay in upper panel) before spectra were calculated. c) Mode-1 linear wave speed as a function of wavelength for the three profiling periods (Fig. 3.2a, b, and c). Horizontal dashed lines represent the average mode-2 wave speed (0.48 m $s^{-1}$) and the measured speed between second and third series (0.54 m $s^{-1}$).

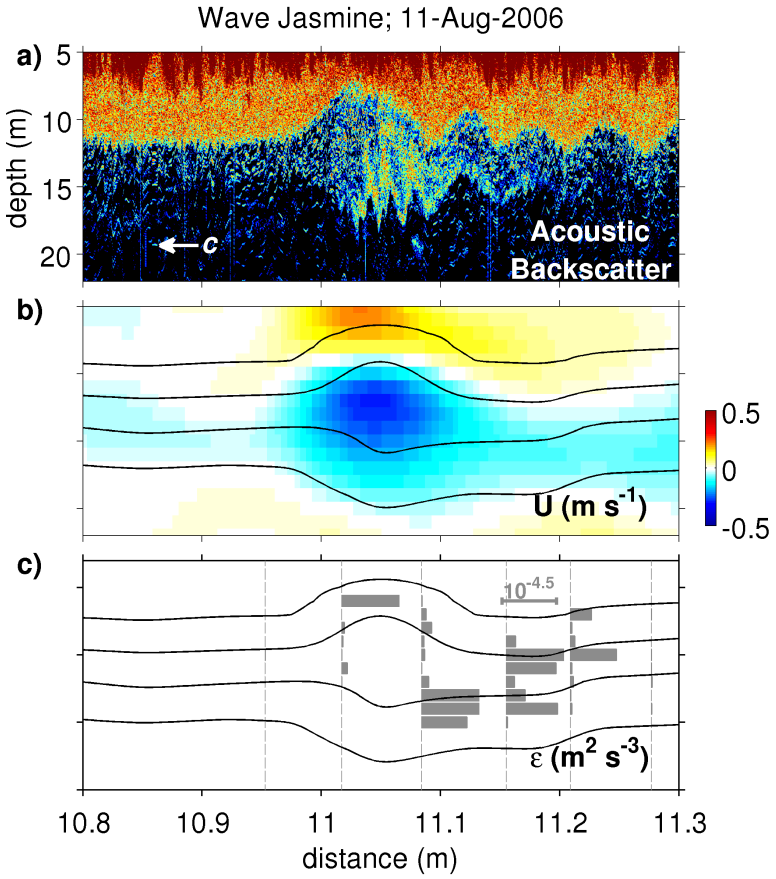


FIGURE 3.6: a) Acoustic backscatter, b) $u_{wave}$, and c) measured dissipation through the leading wave of the third transect of *Wave Jasmine*.

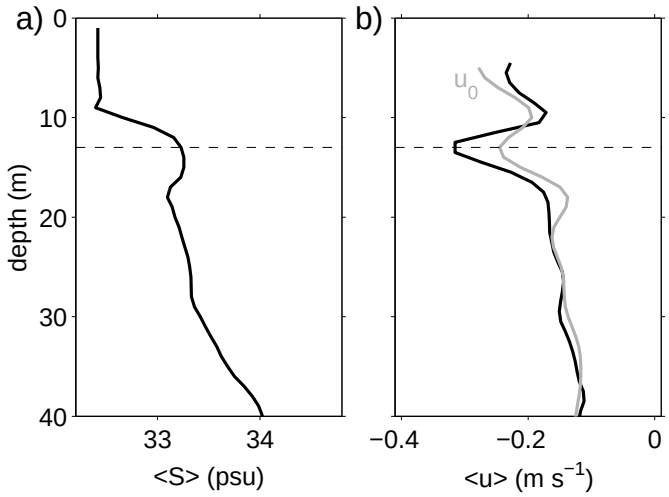


FIGURE 3.7: a) Mean salinity profile and b) velocity profile through the first wave of the third transect. For reference purposes $u_0$ is shown in grey.

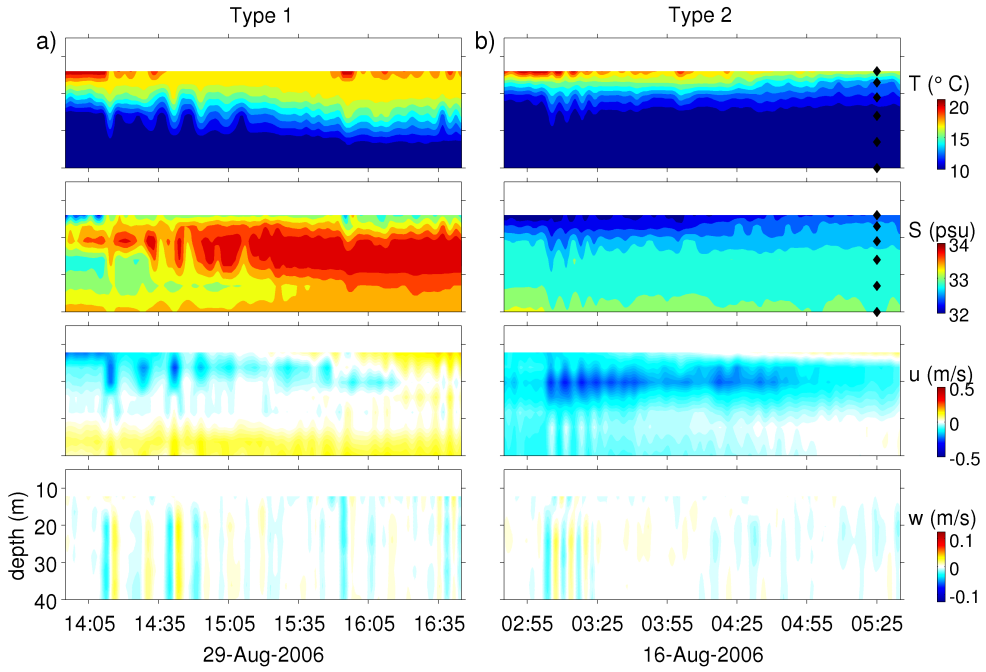


FIGURE 3.8: Contours of temperature, salinity, across-shelf velocity and vertical velocity for a) the third and b) seventh wave group recorded at SW30 (refer to Table 3.1).

TABLE 3.1: Summary of mode-2 NLIW properties as observed from moorings SW38 and SW30. Wave speeds, $c_2'$, are calculated by differencing arrival times at SW38 and SW30. $c_2^*$ is adjusted for advection by barotropic currents (calculated as an hour-long average of the depth-mean velocity immediately preceding the arrival of each wave).

Mode-2 Wave Properties

| | Time: SW38/SW30 | $A$ (m) | $T$ (min) | $c_2'$ | $c_2^*$ | Heading |
|---|---|---|---|---|---|---|
| 1 | 1732 UTC 02 August 2006 | 5.7 | 10.4 | 0.37 | 0.3 | 320 |
| | 1817 UTC 02 August 2006 | 6.2 | 10.4 | | | |
| | | 6.6 | 9.5 | | | |
| 2 | 1444 UTC 03 August 2006 | 4.0 | 5.5 | 0.45 | 0.38 | 315 |
| | 1520 UTC 03 August 2006 | 4.4 | 5.8 | | | |
| | | 3.7 | 7.6 | | | |
| | | 4.5 | 6.1 | | | |
| | | 5.8 | 4.5 | | | |
| | | 4.1 | 3.9 | | | |
| 3 | 0232 UTC 16 August 2006 | 5.3 | 6.8 | 0.51 | 0.43 | 280 |
| | 0305 UTC 16 August 2006 | 3.8 | 6.7 | | | |
| | | 3.4 | 5.9 | | | |
| | | 3.1 | 5.1 | | | |
| | | 1.6 | 3.6 | | | |
| 4 | No Signal | 3.0 | 5.9 | | | 290 |
| | 1610 UTC 17 August 2006 | 2.6 | 5.1 | | | |
| 5 | 1842 UTC 20 August 2006 | 3.2 | 11.5 | 0.37 | 0.29 | 300 |
| | 1926 UTC 20 August 2006 | 3.5 | 7.4 | | | |
| | | 3.0 | 6.7 | | | |
| 6 | 2333 UTC 20 August 2006 | 2.3 | 9.6 | 0.32 | 0.38 | 295 |
| | 0025 UTC 21 August 2006 | 4.7 | 10.5 | | | |
| 7 | 1251 UTC 22 August 2006 | 1.9 | 12.9 | 0.23 | 0.38 | 295 |
| | 1404 UTC 22 August 2006 | 3.0 | 11.1 | | | |
| | | 5.5 | 8.0 | | | |
| | | 3.6 | 10.2 | | | |
| | | 2.9 | 11.8 | | | |
| 8 | 1338 UTC 29 August 2006 | 7.5 | 11.5 | 0.46 | 0.41 | 290 |
| | 1414 UTC 29 August 2006 | 3.3 | 13.5 | | | |
| | | 5.5 | 6.9 | | | |
| | | 5.7 | 9.8 | | | |

# 4 OBSERVATIONS OF POLARITY REVERSAL IN SHOALING NONLINEAR INTERNAL WAVES

Emily L. Shroyer, James N. Moum, Jonathan D. Nash

Journal of Physical Oceanography

45 Beacon Street, Boston, MA 02108

Vol. 39, No. 3, March 2009

## Abstract

Observations off the New Jersey coast document the shoaling of three groups of nonlinear internal waves of depression over 35 km across the shelf. Each wave group experienced changing background conditions along its shoreward transit. Despite different wave environments, a clear pattern emerges. Nearly symmetric waves propagating into shallow water develop an asymmetric shape; in the wave reference frame, the leading edge accelerates causing the front face to broaden while the trailing face remains steep. This trend continues until the front edge and face of the leading depression wave become unidentifiable and a near-bottom elevation wave emerges, formed from the trailing face of the initial depression wave and the leading face of the following wave. The transition from depression to elevation waves is diagnosed by the integrated wave vorticity, which changes sign as the wave's polarity changes sign. This transition is predicted by the sign change of the coefficient of the nonlinear term in the KdV equation, when evaluated using observed profiles of stratification and velocity.


## 4.1 Introduction

The role of nonlinear internal waves (NLIWs) in the coastal ocean has been the study of recent investigations, as many processes may be influenced by these waves. In addition to the potential transport of sediment (Bogucki et al., 1997), nutrients and biota (Lamb, 1997, 2003), these waves may have a profound effect on human activities such as offshore drilling operations and waste disposal (Osborne and Burch, 1980). NLIWs are often associated with large turbulent mixing events (Klymak and Moum, 2003; Moum et al., 2003, 2007b) and are thought to be an important link in energy dissipation from the barotropic tide (e.g., Sandstrom and

Elliott, 1984; Sandstrom and Oakey, 1994). For these reasons, emphasis has been placed on understanding the formation, evolution, and demise of nonlinear internal waves. In this paper we attempt to address the latter part of this story by documenting the shoaling of three groups of nonlinear internal waves of depression.

A pycnocline located near the surface supports waves of depression; however in shallow water or winter stratification, the pycnocline is often located closer to the bottom than the surface, supporting waves of elevation. As a depression wave train shoals, the wave group encounters an increasingly shallow water column. If the pycnocline maintains a constant depth across the shelf, there exists the possibility of a point at which the depression wave group will transition into elevation waves. While field observations documenting reversal of wave polarity are scarce, some modeling and laboratory studies have been designed with the intent of elucidating the evolution process through a critical point, where the first-order nonlinear term vanishes and the fluid shifts from depression to elevation wave favorable (Helfrich et al., 1984; Helfrich and Melville, 1986; Liu et al., 1998; Zhao et al., 2003; Grimshaw et al., 2004; Vlasenko and Stashchuk, 2007). Most of these studies rely on weakly nonlinear theory to describe the evolution of the shoaling wave; however, Vlasenko and Stashchuk (2007) employ a fully nonlinear model. In general, as the modeled soliton approaches the critical point a dispersive wave tail forms consisting of elevation and depression waves, while at the same time an asymmetry in the lead wave develops with the front edge traveling faster than the rear edge. Eventually the lead wave is destroyed, and an elevation wave emerges from the dispersive tail.

The exact position where the various studies refer to the destruction of the lead depression wave and emergence of elevation waves differ. For example, Liu et al. (1998) (using a modified version of the eKdV equation) note the creation of an elevation wave behind the lead depression wave well in advance of the critical point in accordance with Vlasenko and Stashchuk (2007). However, whereas Liu

et al. (1998) continue to refer to the lead depression disturbance as a wave well beyond the critical point, Vlasenko and Stashchuk (2007) refer to the disturbance as a depressed pycnocline and claim conversion happens prior to the critical point. Despite the different terminologies, a comparison between Fig. 10 in Liu et al. (1998) and Fig. 4 in Vlasenko and Stashchuk (2007) reveals a similar development in the shoaling wave. This similarity is perhaps even more surprising due to the significant differences in both the models used and their initialization (e.g., wave amplitude, stratification and bottom slope).

In a separate study using a fully nonlinear model, Vlasenko and Hutter (2002) found that a shoaling depression wave may collapse into a bottom-trapped, elevated mass of fluid, resembling an undular bore, after wave breaking. The authors noted two distinct cases of wave shoaling. The first was controlled primarily by dispersion, resulting in a long wave of depression followed by a dispersive wave train, qualitatively similar to results from weakly nonlinear models. The second case was that nonlinearity dominated wave dynamics, resulting in wave breaking. The rear face of the shoaling wave steepened until a kinematic instability formed, where particle speeds exceeded the local wave speed. The authors established a breaking criterion for the waves, which is both a confirmation and extension of the criterion established by Helfrich and Melville (1986) for steeper slopes.

This paper examines the shoaling process of three wave trains across the New Jersey shelf. In section 4.2 the concept of a critical point is reviewed. The experimental design is outlined in section 4.3. A description of wave properties and background conditions is given in section 4.4. The shoaling process of each wave train is examined in detail in section 4.5, and concluding remarks are presented in section 4.6.

## 4.2 Definition: The Critical Point ($\alpha = 0$)

Nonlinear internal waves observed in geophysical fluids do not generally satisfy assumptions made in weakly nonlinear theory. However, the soliton solution to the KdV equation can be used to illustrate the existence of a critical point. For a KdV soliton, the wavelength, $\lambda$, is related to the amplitude by

$$\lambda^2 \eta_0 = 12 \frac{\beta}{\alpha}. \tag{4.1}$$

The coefficients of the nonlinear and dispersive terms, $\alpha$ and $\beta$, depend on the linear vertical structure function, $\phi$, and linear wave speed, $c_0$, as follows:

$$\alpha = \frac{3 \int_{-H}^{0} (c_0 - U)^2 \phi_z^3 dz}{2 \int_{-H}^{0} (c_0 - U) \phi_z^2 dz} \tag{4.2}$$

$$\beta = \frac{\int_{-H}^{0} (c_0 - U)^2 \phi^2 dz}{2 \int_{-H}^{0} (c_0 - U) \phi_z^2 dz}. \tag{4.3}$$

As long as $c_0$ is everywhere greater than $U$, oceanic conditions control the polarity of the soliton through the sign of the coefficient, $\alpha$, as evident in relation (4.1). In a two-layer fluid without background shear, the transition between $\eta_0 > 0$ and $\eta_0 < 0$ occurs at a critical point (defined as $\alpha = 0$) when $h_1 = h_2$, where $h_1$ and $h_2$ are the depth of the upper and lower layer, respectively. This result may be extended to include an upper ($U_1$) and lower layer velocity ($U_2$), which provides a simple interpretation of the effect of background shear on wave transition (4.4):

$$\frac{h_1}{h_2} = \frac{c_0 - U_1}{c_0 - U_2}. \tag{4.4}$$

As an example, consider the case where $U_1$ is in the direction of wave propagation (i.e., toward shallower water), while $U_2$ travels in the opposite direction (i.e.,

$U_2 < 0$). In this case, the ratio on the R.H.S. of (4.4) is less than one, and the wave will reach the critical point before $h_1 = h_2$. The transition will be delayed if the ratio on the R.H.S. is greater than one. While this development is simple, it serves as a useful illustration of the effect background shear has on the location of the critical point. The parameters, $\alpha$ and $\beta$, may be computed numerically from (4.2) and (4.3) for a fully stratified flow with background shear. In section 4.5, we test the efficacy of using $\alpha$ to define wave polarity by comparison to an observational diagnostic.

In reality, higher order or fully nonlinear theories are needed to describe the transition across a critical point; since by definition the solitary wave does not exist when $\alpha = 0$. Including a cubic nonlinear term in the equation allows for the development of multiple critical points associated with both the quadratic and cubic nonlinear coefficients. Grimshaw et al. (2004) provide a useful, more detailed description of the possible wave transformation scenarios using this expanded theory.

## 4.3 Experimental Details

Shipboard measurements on the *R/V Oceanus* were conducted off the coast of New Jersey in conjunction with the *NonLinear Internal Wave Initiative/Shallow Water '06 Experiment (NLIWI/SW06)* in August 2006 (Tang and Coauthors, 2007). Site location and mooring positions are indicated in Fig. 4.1; although the data presented here are solely from shipboard observations, mooring locations are shown for future reference. NLIWs were located and tracked using a range of shipboard acoustics. High-resolution echosounder images provided a qualitative view of the wave structure and were useful in tracking disturbances in real time. Velocity data was obtained using both a hull-mounted 300 kHz ADCP and a side-mounted 1200 kHz ADCP. The setup permitted velocity measurements from $\sim$ 10 m above the

sea floor to within 3 m of the surface. Depending on wind speed and direction, the ship's X-band radar provided a clear picture of wave orientation; these images along with visual sightings of wave fronts helped us to make our crossings perpendicular to wave fronts.

Once a wave train was identified the wave group was transited at a high speed (3–4 m $s^{-1}$), providing a relatively undistorted view of the waves. The ship was then positioned ahead of the waves and held semi-stationary as microstructure measurements of density ($\sigma_\theta$) and turbulence dissipation rate ($\epsilon$) were made using the Chameleon profiler (Moum et al., 1995). On average, five profiles were obtained through a given wave in a train; however, this number varied depending on the disturbance width and the relative ship–wave motion. The ship maintained position as the first few waves of the train propagated past (typically 3–4), then the profiler was recovered and the process repeated. At each station, the profiling period lasted from a half-hour to an hour. This "leapfrog" method was continued as the waves propagated onshore, enabling multiple observations of a single evolving wave group to be made over long distances, in some cases more than 50 km.

## 4.4 Observations

### 4.4.1 Wave properties

During the course of the cruise ($\sim$ 1 month), observations of 27 wave groups were made. Background stratification and shear varied in both time and space, creating heterogeneous conditions for wave groups along their shoreward journey. A naming convention was adopted for bookkeeping purposes. In this paper, we examine the evolution of three wave groups, *Wave Sonny*, *Wave Tonya*, and *Wave Wyatt*, first observed at 2000 UTC 18 August 2006, 1400 UTC 20 August 2006, and 0800 UTC 22 August 2006, respectively. In each case, waves were followed

onshore more than 35 km ($\sim$ 14 hours), over which time at least 10 Chameleon profiling time-series were made. These three wave groups are unique in that they provide clear observational evidence of polarity reversal. The other 24 wave groups were either not tracked as far inshore (so that the critical point for wave transition was not captured), or the waves were of smaller amplitude (so that the wave signal deteriorated before transition could be observed). As a result, we focus the following analysis on the three wave packets, *Sonny*, *Tonya* and *Wyatt*.

The ship transects following these waves are shown in Fig. 4.1; except for small deviations primarily required to avoid mooring positions, the waves were tracked perpendicular to wave fronts. Distances along the wave path are defined using the axes shown in black. The positive x-axis is oriented in the mean direction of wave propagation, and the origin is defined at mooring SW30, located at the intersection of the T-shaped array.

The changes in the vertical scale, horizontal scale, and wave speed of the lead waves are shown in Fig. 4.2. The vertical scale of the wave, $A$, is an estimate of the maximum displacement of scattering layers, which correspond closely to density surfaces; here we define waves of depression as having negative $A$. $A$ is equivalent to the amplitude, $\eta_0$, for a KdV soliton (section 4.2). The horizontal wave scale, $L$, is an estimate of the total disturbance width, which for a symmetric KdV soliton would correspond to $4\lambda$ as defined in section 4.2. We use $A$ and $L$ as opposed to $\eta_0$ and $\lambda$ because of the highly nonlinear, asymmetric nature of the observed waves. Wave speeds were calculated from the inverse slope of the time-position plot of maximum displacement (Fig. 4.2c).

Mean wave speeds and propagation direction, as calculated from acoustic backscatter and radar, were 0.74/0.73/0.71 m s$^{-1}$ and 300°/300°/310° for *Sonny*/ *Tonya*/ *Wyatt*. These wave speeds represent the mean over the entire transit period; local phase speed vary likely due to modulation by the internal tide. *Wave Sonny* initially had

a horizontal scale, $L$, of $\sim$ 500 m that broadened to over 1300 m prior to transition. *Tonya's* horizontal wave scale increased from 400 m to 1200 m, and *Wyatt* displayed the most extreme example of broadening, increasing nearly five times from an initial $L$ of 300 m. The amplitude of *Wave Sonny* decreased from $A \approx$ -12 m to $A \approx$ -6 m prior to transition. Waves *Tonya*, and *Wyatt* experienced rapid, extreme changes in amplitude, in which $A$ nearly doubled in magnitude for a short distance. These anomalies (denoted by circles in Fig. 4.2a) are associated with potential wave interactions; a more detailed analysis of these interactions is the focus of a separate study. These deviations are superimposed on a gradual decreasing trend from amplitudes of -10/-12 m to -5/-5 m for *Tonya/ Wyatt*.

The signature of the observed waves deteriorated before breaking of the lead elevation wave could be documented. This was possibly due to limitations in our tracking techniques, as very short (50 m) NLIWs of elevation have been observed in the region shoreward of the 30 m isobath (Scotti and Pineda, 2004). In particular, the ability to distinguish a small-amplitude, short wave from a moving platform depends on the relative ship to wave speed. Assuming a relative speed of a few meters per second, real-time observations would last for under a minute for a wave with a length of $\sim$100 m. It is also possible that dissipation by bottom friction accounts for the loss of the wave signature.

### 4.4.2 Background conditions: properties of the wave guide

Background profiles of density and velocity for waves *Sonny*, *Tonya*, and *Wyatt* are shown in Fig. 4.3. Background density is estimated using at least one full depth profile taken prior to the wave's arrival at a given location; if more than one profile was obtained ahead of the wave, the average is used. Background velocity measurements represent a five-minute time average of data taken ahead of the wave; values are extrapolated to the surface and at depth using a constant velocity. In

all cases the pycnocline depth (Fig. 4.3a) increased as the water depth decreased, hinting at the development of a critical point. A reversal in the background shear (Fig. 4.3b) was apparent during each wave's shoreward transit time. Since the wave transit times exceeded the $M_2$ tidal period, tidal motions are certainly aliased into this signal. The fluid may be approximated as two layers using the maximum value of buoyancy frequency to distinguish the interface. Average values of background velocity were used to compute the ratio (4.4) shown in Fig. 4.3c (black lines, left axis). When $h_1 h_2^{-1}$ (solid black line) $\geq (c_0 - U_1)(c_0 - U_2)^{-1}$ (dashed black line), the fluid transitioned to elevation wave favorable. While we base the location of the critical point on $\alpha = 0$ (gray line), computed using observed profiles of density and velocity, we note that the two-layer approximation is consistent with this fully stratified, sheared calculation, i.e., $\alpha = 0$ occurs when $h_1 h_2^{-1} = (c_0 - U_1)(c_0 - U_2)^{-1}$. The two-layer approximation is useful in distinguishing the consequence of the background shear on the location of the critical point. The shaded gray regions surrounding the darker gray lines are confidence limits assuming that the depth bin position for both density and velocity is known to within $\pm 2$ m.

The exact location of the critical point ($\alpha = 0$) and nature of the wave guide shoreward of this point differed for each wave group. For *Wave Sonny*, the very last profile approached the critical point for a two-layer fluid without shear flow with $h_1 h_2^{-1} = 1$, and exceeded the critical point for a shear flow ($h_1 h_2^{-1} \geq (c_0 - U_1)(c_0 - U_2)^{-1}$). Unfortunately, the wave group was poorly defined much past this point, preventing extensive observations in the elevation-friendly environment. In contrast, *Wave Tonya* was followed for a considerable distance after passing through the critical point at around 32.5 km. The background conditions for *Wave Wyatt* were complex, in that the fluid switched from supporting depression waves to elevation waves ($\sim$ 26–36 km) and back again to depression waves. In fact, the wave guide seemed to hover around the critical point ($\alpha \approx 0$) rather than undergoing a

definitive transition.

## 4.5 Discussion: Wave Shoaling and Polarity Reversal

Time series showing the evolution of *Wave Sonny* as it developed from a depression wave through transition to an elevation wave, are presented in Fig. 4.4. These series were taken during semi-stationary times of shipboard profiling; the time series were converted into distance plots using wave speed. Isopycnals calculated from streamlines, following the method outlined by Moum and Smyth (2006), are contoured in black. The background velocity has been subtracted using the upstream vertical profile mapped onto isopycnals. Initially, the structure of the leading depression wave (Fig. 4.4, left column) was symmetric. The horizontal velocity reached a maximum speed in excess of 0.45 m $s^{-1}$, and there was a strong compensating flow at depth. The vertical velocity signature shows a downward velocity at the leading edge and upward motion at the trailing edge of each wave. As the wave shoaled, an asymmetry in the leading wave developed (Fig. 4.4, middle columns); the front face of the wave broadened and the rear face of the wave remained steep. The maximum horizontal velocity shifted closer to the rear face of the wave; this is similar to the description given by Vlasenko and Hutter (2002). Accompanying the elongation of the leading face and convergent region, the downwelling region became weaker in magnitude but broader in scale while the upward motion present at the steep rear face remained sharp and clearly defined. In the final stage as a leading elevation wave emerged (Fig. 4.4, right column), an upward pulse preceded a downward pulse of equal magnitude; we take this as a defining characteristic of elevation waves. At this point, maximum horizontal velocities were $\sim$ 0.13 m $s^{-1}$, five times smaller than the phase speed of the wave. Referring to Fig. 4.3, the observed appearance of the leading elevation wave at about 40 km

is consistent with the transition through the theoretical critical point at 38 km, as defined by the background conditions alone.

Figure 4.4 demonstrates that the sign of the vorticity for depression waves is different from that of elevation waves for waves propagating in the same direction. These two cases are clarified in Fig. 4.5. We employ this distinction as an observational diagnostic, and define the integrated wave vorticity,

$$\Omega_w = \int_{-H}^{0} \omega dz = \int_{-H}^{0} \frac{\partial u_{\text{wave}}}{\partial z} - \frac{\partial w_{\text{wave}}}{\partial x} dz. \tag{4.5}$$

For a wave of depression/elevation propagating in the positive x-direction, the integrated wave vorticity is positive/negative. This is a useful characteristic for our purposes, since we follow waves that change sign but not propagation direction. $\Omega_w$ is evaluated for each transect, and its change in sign used as a marker for the observed location of the critical point.

The acoustic backscatter series shown in Fig. 4.6a for *Wave Sonny* provides a means of visualizing the developing wave form. Well-formed depression waves were observed during the earliest stages, when the pycnocline was approximately 15 m in almost 70 m of water (Fig. 4.6A,B). As the wave shoaled, the leading wave began to form a slight asymmetry (between 30–35 km; Fig. 4.6E–F). This trend became more pronounced as the wave approached the critical point (Fig. 4.6G–I), after which freely propagating elevation waves emerged (Fig. 4.6J–K). The sign of the lead wave vorticity in the last two transects is negative (Fig. 4.6b). The process resembles the transformation described by models (e.g., Liu et al., 1998; Vlasenko and Stashchuk, 2007), although as mentioned in section 4.1, ambiguity exists in defining a precise location for the demise of the lead elevation wave. In these observations the case is further complicated by the difficulty in distinguishing dispersive waves from pre-existing wave forms, i.e., observations are the product of several shoaling waves

rather than a single soliton. Deciphering the details of the wave train's evolution is complicated by the coarse horizontal resolution of the observations; wave crossings are separated by distances of approximately $5L$. Another source of disparity between the observed and modeled waves arises from differences in the model initializations and observations. In this work, we have chosen to define the observed transition as the location at which the lead wave's velocity signal can no longer be separated from the mean flow, i.e., $\Omega_w = 0$. However, while care was taken to ensure that the *RV Oceanus* was not prematurely turned on transects, distinguishing the leading edge of a wide ($\sim$ 2 km), small-amplitude ($<$ 5 m) wave is somewhat subjective. And yet, the demise of the leading depression wave as defined by $\Omega_w = 0$ was coincident with the transition region as predicted by the change in sign of $\alpha$ from first-order KdV analysis.

The development of the lead wave asymmetry in *Waves Tonya* and *Wyatt* and their subsequent evolution through the critical point is consistent with that described above for *Wave Sonny*. We summarize the attributes of the evolution process for each of the wave groups in Figs. 4.7 and 4.8. The speed of each wave group's front edge shows a clear departure from that of the trough and rear edge (Fig. 4.7a–c). This separation continued as the waves approached their respective critical points. In each case the front of the wave traveled $\sim$ 5 cm s$^{-1}$ faster than the trough/rear of the wave. The increased speed of the front edge marks the onset of the structural asymmetry in the waves. The asymmetry continued to develop as the speed of the front remains greater than that of the rest of the wave. Note that for each wave this pattern of asymmetry onset and further development is present. Wave speed estimates given in Fig. 4.2 appear inconsistent with values shown in Fig. 4.7; however, the two are resolved if the average wave speed is calculated using all locations along wave transits.

The evolution of the asymmetry in the lead waves is quantified using the wave

slope of the front and rear faces (Fig. 4.8). Slope magnitudes were calculated using a linear fit to an acoustic backscatter contour associated with the pycnocline. (The front and rear faces are fit separately using a least squares approximation to a line.) This technique depends on the premise that density surface follow backscatter contours. For the waves presented here, this assumption seems reasonable (Fig. 4.4a). For *Wave Sonny* (Fig. 4.8a), the slope of the front face tended to zero as the wave approached the critical point. An increase in the rear slope is observed at approximately 34 km (i.e., the rear face steepened), after which the rear slope remained relatively constant. The shift from symmetric waves to asymmetric wave is emphasized in the slope ratio. Prior to transition the ratio is near one; through the transitional period, this ratio decreases steadily toward zero. After transition lead elevation waves (gray markers) are once again nearly symmetric, as the front slope of the elevation wave now corresponds to rear slope of the depression wave just prior to transition. A similar pattern is observed for *Tonya* (Fig. 4.8b) and *Wyatt* (Fig. 4.8c). *Wave Tonya* displayed a steady decrease towards zero in the front slope, while the rear slope remained greater than zero and fairly steady. After transition, symmetric elevation waves (slope ratio = 1) were observed for a considerable distance (over 20 km). For *Wave Wyatt* the large asymmetry apparent at 21 km stands out as an anomaly. The rear face was extremely steep, possibly approaching the breaking limit documented by Vlasenko and Hutter (2002). However, an analysis of their breaking criterion reveals that the mild slope dominated, and topographically controlled breaking was highly unlikely. The slope of the front face continued to weaken past this point. While a decrease is also apparent in the slope of the rear face, the slope ratio nevertheless tends to zero, mirroring the development in the other two wave groups.

The transition from depression to elevation waves is clear (Fig. 4.9). In each case, the theoretical critical point, $\alpha = 0$, predicts the observed transition to

elevation waves as defined by $\Omega_w$. Fig. 4.9a is an exact replication of Fig. 4.6b for *Sonny* and has been discussed previously. For *Wave Tonya* (Fig. 4.9b) the lead elevation wave emerged past 34 km. As with *Sonny*, the observed transition ($\Omega_w = 0$) is in good agreement with the predicted critical point ($\alpha = 0$). The wave group was transited several times beyond this point, and the elevation wave structure was clearly developed. Both *Sonny* and *Tonya* displayed a smooth transition of background conditions from a depression- to elevation-friendly environment. In contrast, the background conditions for *Wave Wyatt* were more complex (refer to Fig. 4.3), and as may be expected the shoaling process is not as clear. Around 28 km the signature of the initial depression wave is faint; a weak positive vorticity (not shown) precedes a relatively stronger negative vorticity, which seems to support the impending demise of the lead depression wave and emergence of an elevation wave. Recall, however, that the background conditions for *Wave Wyatt* hovered around $\alpha = 0$ rather than clearly transitioning. Similarly, the wave form disintegrated into a disorganized assortment of disturbances of the pycnocline past this point rather than clearly establishing a lead elevation wave, and we cease to recognize a leading wave of either polarity shoreward of this region.

## 4.6 Summary

Observations of three groups of shoaling NLIWs of depression reveal the complex evolution of each of the leading waves. Shoaling is controlled by background stratification and velocity, which vary not only for each of the wave trains, but also over the shoaling duration for a particular train that in each case is longer than either a tidal cycle or inertial period. As the waves traveled shoreward, they experienced a decrease in water column depth, an increase in pycnocline depth, and a change in background shear. These factors all contributed to the development

of a critical point, where conditions change from supporting depression waves to supporting elevation waves.

As the waves approached the theoretical critical point ($\alpha = 0$) an asymmetry developed in the lead wave; the front edge accelerated relative to the trough and rear edge, leading to a broadening of the front face while the rear face of the wave remained steep. Eventually, the slope of the front face of the lead depression wave became indistinguishable from zero. At this point an elevation wave, formed by combining the rear face of the original depression wave with the front face of the second wave in the train, emerged as the leading wave. The signature of transition is apparent in the wave's vertical velocity and vorticity. For a depression wave, downwelling precedes upwelling as horizontal velocity converges at the leading edge of the wave near the surface. Furthermore, the wave-induced circulation yields a positive vertically integrated wave vorticity through a depression wave. The reverse is true for elevation waves. This difference is utilized to establish a diagnostic for the observed wave transformation. For each of the wave groups, the observed transition point coincides with the prediction from small-amplitude wave theory, as long as the effect of background shear is included. For two of the three waves this transition is clearly defined; for the third, background conditions produce a situation that appears favorable to neither elevation nor depression waves.

## 4.7 Acknowledgments

This work was funded by the Office of Naval Research. We are grateful to the Captain, crew and marine technician of *R/V Oceanus*. We acknowledge the assistance of Mike Neeley-Brown, Ray Kreth, Alexander Perlin, Greg Avicola, and Sam Kelly in obtaining the data. This work has benefited greatly from discussions with Bill Smyth.

## Bibliography

Bogucki, D., T. Dickey, and L. G. Redekopp, 1997: Sediment resuspension and mixing by resonantly generated internal solitary waves. *J. Phys. Ocean.*, **27**, 1181–1196.

Grimshaw, R., E. Pelinovsky, T. Talipova, and A. Kurkin, 2004: Simulation of the transformation of internal solitary waves on oceanic shelves. *J. Phys. Ocean.*, **34**, 2774–2791.

Helfrich, K. R., and W. K. Melville, 1986: On long nonlinear internal waves over slope-shelf topography. *J. Fluid Mech.*, **167**, 285–308.

Helfrich, K. R., W. K. Melville, and J. W. Miles, 1984: On interfacial solitary waves over slowly varying topography. *J. Fluid Mech.*, **149**, 305–317.

Klymak, J. M., and J. N. Moum, 2003: Internal solitary waves of elevation advancing on a shoaling shelf. *Geophys. Res. Let.*, **30**, 2045–2048.

Lamb, K. G., 1997: Particle transport by nonbreaking internal solitary waves. *J. Geophys. Res.*, **102**, 18641–18660.

— 2003: Shoaling solitary internal waves: on a criterion for the formation of waves with trapped cores. *J. Fluid Mech.*, **478**, 81–100.

Liu, A. K., Y. S. Chang, M.-K. Hsu, and N. K. Liang, 1998: Evolution of nonlinear internal waves in the East and South China Seas. *J. Geophys. Res.*, **103**, 7995–8008.

Moum, J. N., D. M. Farmer, E. L. Shroyer, W. D. Smyth, and L. Armi, 2007: Dissipative losses in nonlinear internal waves propagating across the continental shelf. *J. Phys. Ocean.*, **37**, 1989–1995.

Moum, J. N., D. M. Farmer, W. D. Smyth, L. Armi, and S. Vagle, 2003: Structure and generation of turbulence at interfaces strained by internal solitary waves propagating shoreward over the continental shelf. *J. Phys. Ocean.*, **33**, 2093–2112.

Moum, J. N., M. C. Gregg, R. C. Lien, and M. E. Carr, 1995: Comparison of turbulence kinetic energy dissipation rate estimates from two ocean microstructure profilers. *J. Atmos. Ocean. Tech.*, **12**, 346–366.

Moum, J. N., and W. D. Smyth, 2006: The pressure disturbance of a nonlinear internal wave train. *J. Fluid Mech.*, **558**, 153–177.

Osborne, A. R., and T. L. Burch, 1980: Internal solitons in the Adaman Sea. *Science*, **208**, 451–460.

Sandstrom, H., and J. A. Elliott, 1984: Internal tide and solitons on the Scotian shelf: A nutrient pump at work. *J. Geophys. Res.*, **89**, 6415–6426.

Sandstrom, H., and N. S. Oakey, 1994: Dissipation of internal tides and solitary waves. *J. Phys. Ocean.*, **25**, 604–614.

Scotti, A., and J. Pineda, 2004: Observation of very large and steep internal waves of elevation near the Massachusetts coast. *Geophys. Res. Let.*, **31**, doi:10.1029/2004GL021052.

Tang, D. J., and Coauthors, 2007: Shallow Water '06. *Oceanography*, **20**, 156–167.

Vlasenko, V., and K. Hutter, 2002: Numerical experiments on the breaking of solitary internal waves over a slope-shelf topography. *J. Phys. Ocean.*, **32**, 1779–1793.

Vlasenko, V., and N. Stashchuk, 2007: Three-dimensional shoaling of large-amplitude internal waves. *J. Geophys. Res.*, **112**, doi:10.1029/2007JC004107.

Zhao, Z., V. Klemas, Q. Zheng, and X. Yan, 2003: Satellite observation of internal solitary waves converting polarity. *Geophys. Res. Let.*, **30**, doi:10.1029/2003GL018286.

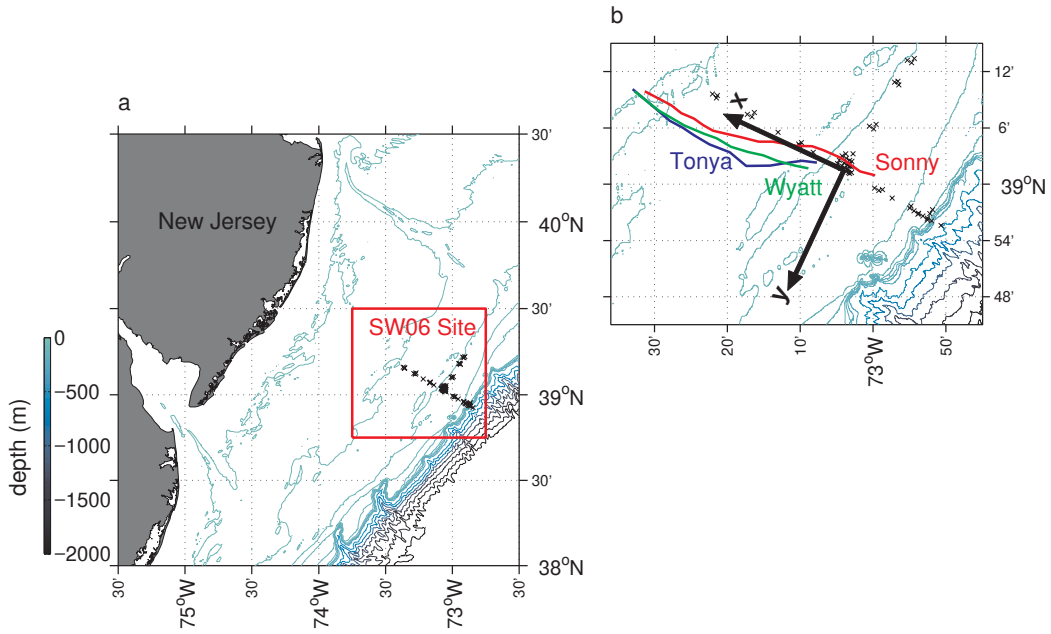


FIGURE 4.1: a) SW06 Site and bathymetry. Black x's indicate locations of SW06 moorings. b) Ship transects following *Wave Sonny* (red), *Wave Tonya* (blue), and *Wave Wyatt* (green). The waves were tracked perpendicular to wave fronts, determined visually and from the ship's radar. The wave reference frame is rotated into the mean direction of wave propagation, and the origin positioned at the intersection of the T-shaped mooring array (mooring SW30).

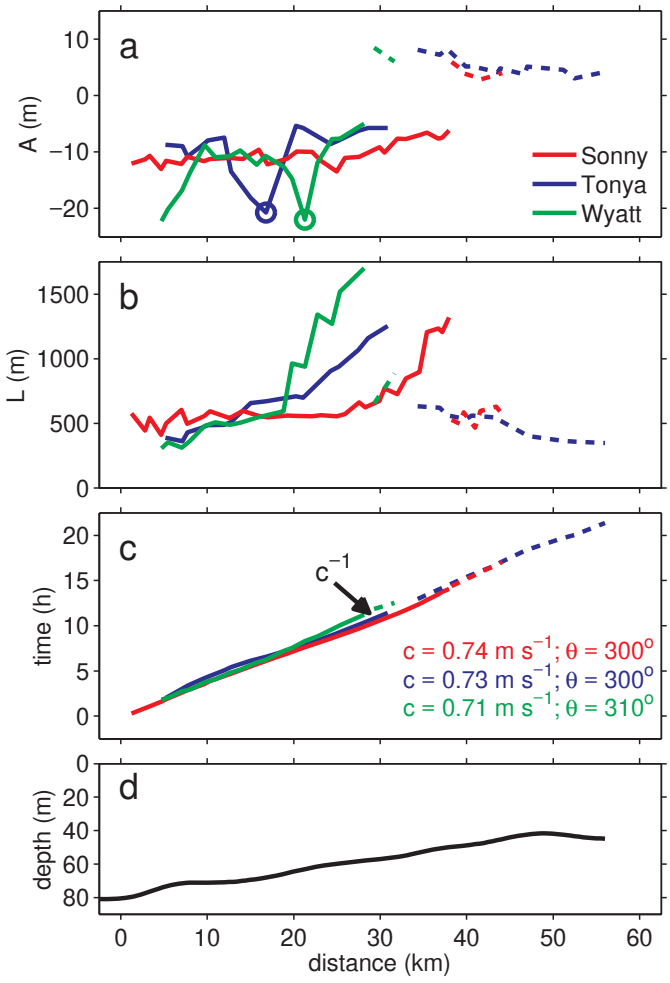


FIGURE 4.2: $A$ (a), $L$ (b), and time-position (c) of the leading wave. $L$ is a measure of the full disturbance length. Solid lines indicate depression waves, and dashed lines indicate elevation waves. Circles in (a) show locations of wave interactions. Average wave speeds, $c = \Delta x/\Delta t$, and headings are given in (c). The bottom depth is shown in (d).

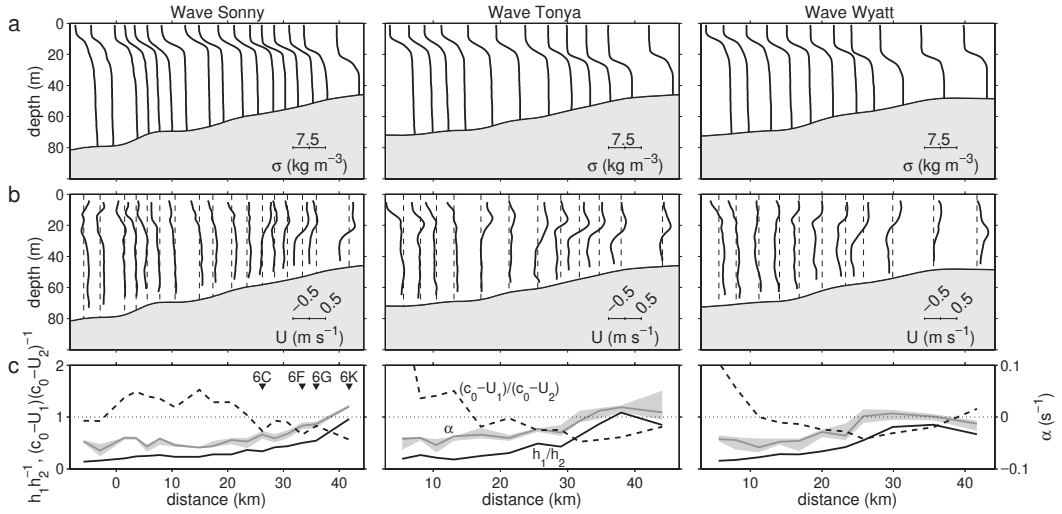


FIGURE 4.3: Profiles of density (a) and background velocity (b) ahead of *Wave Sonny*, *Wave Tonya*, and *Wave Wyatt*. Lower panels (c) are divided into two y-axes. The left axis and corresponding black solid and dashed lines represent the two-layer relation described in (4.4). The continuous case is represented by the change in sign of $\alpha$ (gray line) corresponding to the right axis. The critical point defined by the two-layer approximation is consistent with the continuous estimate for each wave group. For *Wave Sonny* the critical point occurs at approximately 38 km, and for *Tonya* the critical point occurs near 33 km. For *Wave Wyatt* conditions are more varied, and the fluid alternates from supporting depression waves to elevation waves ($\sim$ 26–36 km) and back again to depression waves. Black triangles located on *Sonny* (c) refer to positions in Fig. 4.6 and correspond to transects shown in Fig. 4.4.

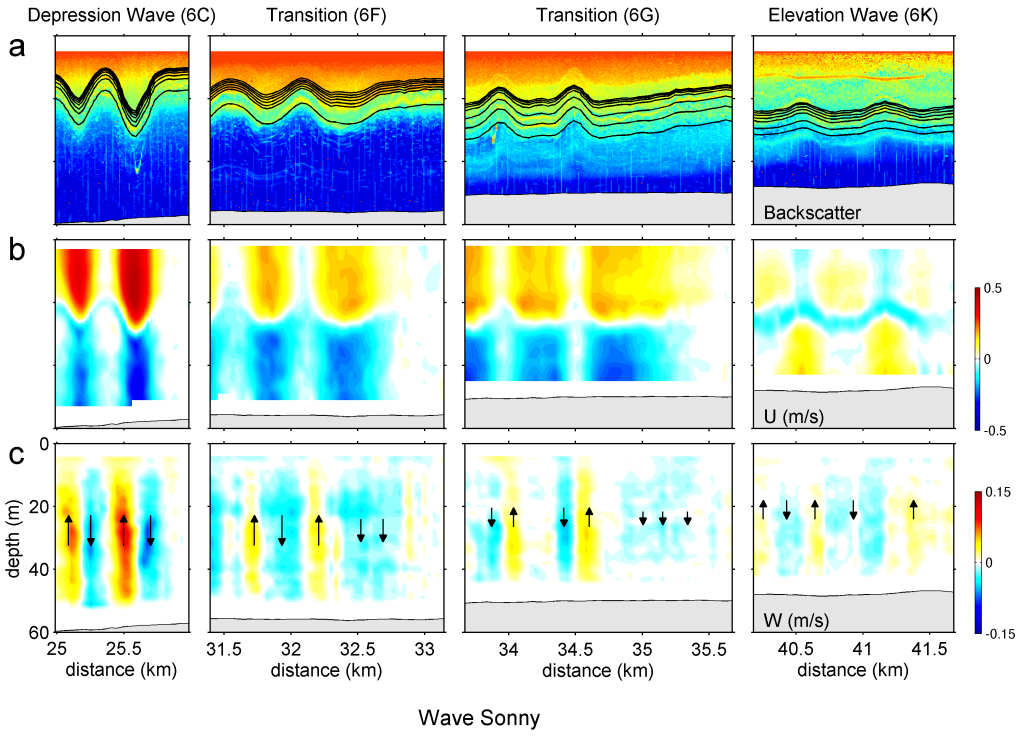


FIGURE 4.4: Acoustic backscatter (a), horizontal velocity (b), and vertical velocity (c) shown for four different periods along the propagation path of *Wave Sonny*. The wave is propagating to the right. Isopycnals range from 22.25 kg $m^{-3}$ to 25.25 kg $m^{-3}$. Black arrows emphasize downward and upward motions. The relative size of the arrows is representative of the magnitude of the vertical velocity. The wave states (Depression, Transition, and Elevation) correspond to Fig. 4.6C, 4.6F, 4.6G and 4.6K. These locations are also marked in Fig. 4.3c.

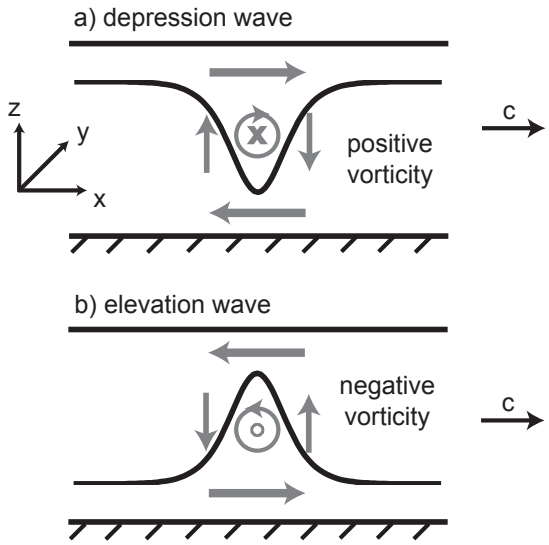


FIGURE 4.5: Schematic illustrating the different vorticity signs for depression (a) and elevation (b) waves.

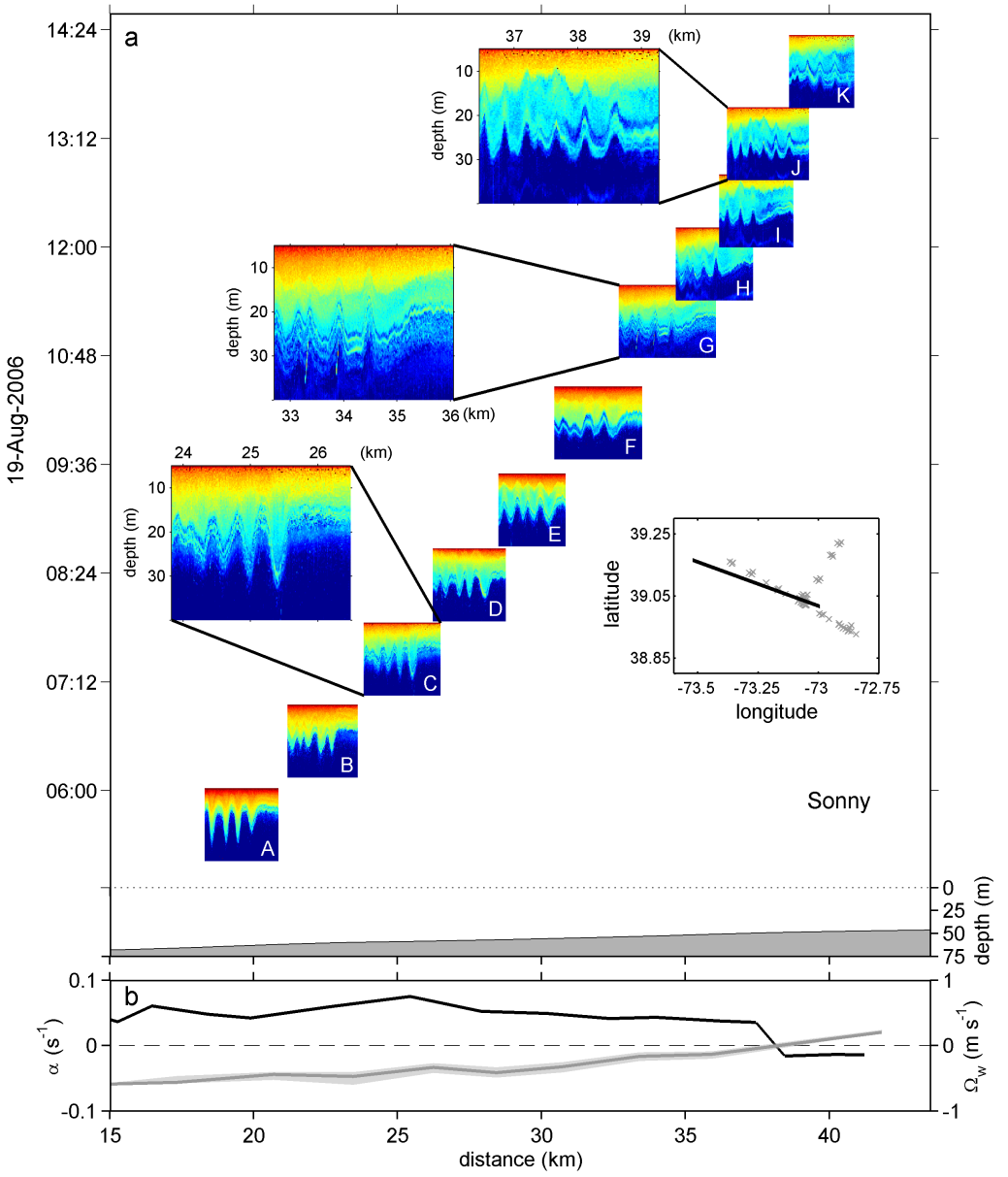


FIGURE 4.6: a) Acoustic backscatter transects taken perpendicular to wave front for *Wave Sonny*. Each series has been corrected for Doppler shifting so that waves may be viewed in a spatial frame with minimal distortion. The horizontal axes for each panel (A–K) are accurately scaled to the distance axis; the vertical axes for (A–K) are centered about the time of the lead wave. Select transects are enlarged in order to highlight details of structural evolution. For reference purposes, water column depth is plotted at the bottom. Lower right inset shows mooring array and approximate wave path (black line). b) The predicted critical point defined by the parameter, $\alpha$, is plotted in gray on the left-hand side, and the observed transition point given by the sign of the maximum integrated wave vorticity is plotted in black on the right-hand side.

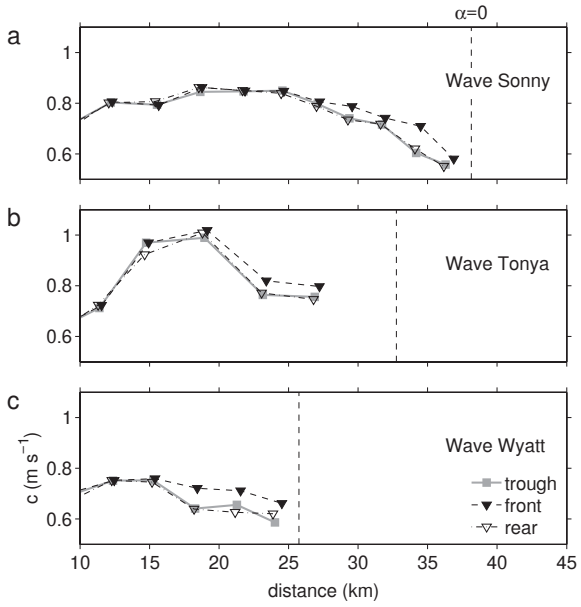


FIGURE 4.7: Wave speed of the front edge (solid triangles), trough (gray squares), and rear edge (open triangles) for *Waves Sonny* (a), *Tonya* (b), and *Wyatt* (c). Only wave speeds associated with depression waves are shown. The critical point ($\alpha = 0$) is marked with the vertical dashed line.

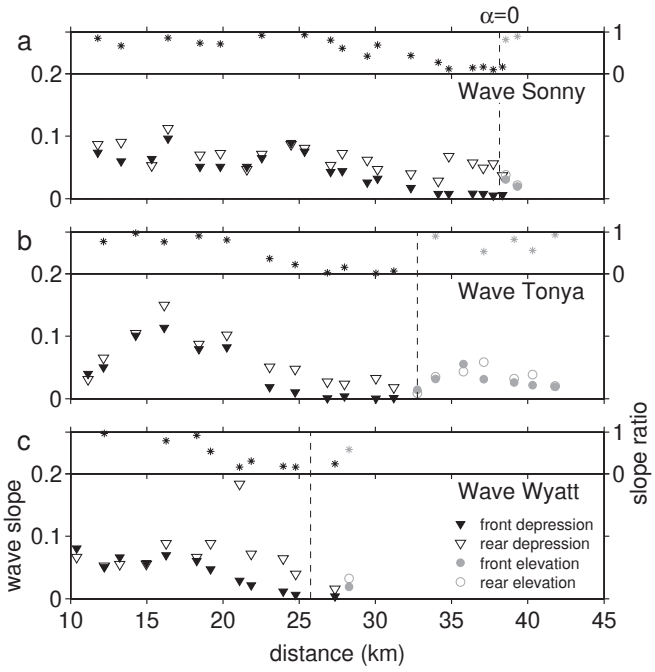


FIGURE 4.8: Changes in wave slope as waves shoal. Left-hand side: Slope magnitude of front (solid markers) and rear face (open markers) for *Waves Sonny* (a), *Tonya* (b), and *Wyatt* (c). Black triangles represent waves of depression, and gray circles represent waves of elevation. Right-hand side: The ratio of the front slope to the rear slope ($*$). The critical point ($\alpha = 0$) is marked with the vertical dashed line.

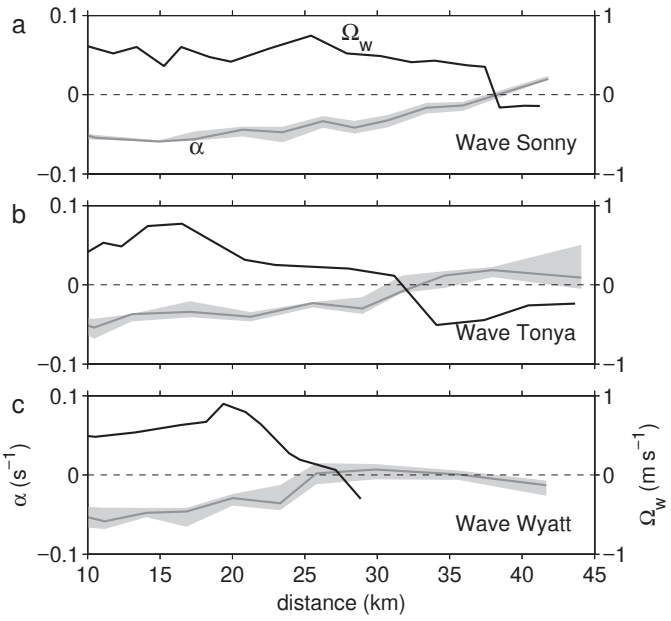


FIGURE 4.9: Observed wave transition point versus the weakly nonlinear prediction. The maximum of the vertically integrated wave vorticity (black line, R.H.S.) and $\alpha$ (gray line, L.H.S.) for *Waves Sonny* (a), *Tonya* (b), and *Wyatt* (c).

# 5 ENERGY TRANSFORMATION AND DISSIPATION IN THE EVOLVING NLIW FIELD OVER NEW JERSEY CONTINENTAL SHELF

Emily L. Shroyer, James N. Moum, Jonathan D. Nash

## Abstract

Nonlinear internal wave energy on New Jersey's continental shelf exhibited significant variability during the Shallow Water 2006 experiment. Temporally, wave energies were ten times greater from the 16–26 of August 2006, as compared to the rest of the month. Spatially, leading waves grew in energy/amplitude across the outer shelf, reached peak values near 40 km inshore of the shelf break, and then lost energy to turbulent mixing, which was dominated by dissipation in the mixed layer as opposed to the bottom boundary layer. Wave growth was attributed to the bore-like nature of the internal tide, as wave groups that exhibited larger long-term displacements (occurring for a few hours) typically had larger energies inshore. The character of turbulent kinetic energy (TKE) dissipation in the wave cores could be classified into one of three types: i) low dissipation, ii) scattered, elevated dissipation, or iii) high, localized dissipation. While a direct relationship between wave energy and the character of TKE dissipation at a given position/time did not exist, the average dissipative loss (over the region of decay) scaled with the peak energy in the wave groups. The scaling applied to mooring data was consistent with estimates of dissipative loss from the flux divergence of the energy. The decay time scale of the waves is approximately 12 hours corresponding to a length scale of 35 km (100 wavelengths). Imposed on these gradual energetic trends, were short, rapid exchanges associated with wave interactions and blocking by topography. Both cases resulted in the onset of shear instabilities and large energy loss to turbulent mixing.

## 5.1 Introduction

In coastal environments, nonlinear internal wave (NLIW) packets transfer energy from the barotropic and baroclinic tide onto the shelf. Here, the wave groups provide an energy source for turbulent mixing. The energy in the waves that is available for conversion to mixing is the sum of the kinetic energy and the available potential energy. The kinetic energy is defined as

$$KE = \int_0^H \int_{x_1}^{x_2} \frac{1}{2}\bar{\rho}(u_{wave}^2 + w_{wave}^2)dxdz, \tag{5.1}$$

and available potential energy is

$$APE = \int_0^H \int_{x_1}^{x_2} (\rho - \rho_0)gzdxdz, \tag{5.2}$$

where integration limits extend from the bottom, $z = 0$, to the surface, $z = H$, and across the wave. In the above expressions, $\bar{\rho}$ is the average density, and $\rho_0$ is the reference density, defined by the state of minimum potential energy (e.g., Shepherd, 1993; Winters et al., 1995). The total, $E \equiv KE + APE$, is defined as the pseudoenergy. When considering the impact of the nonlinear internal waves on shelf mixing, the physically relevant quantity is the pseudoenergy and not simply the combination of $KE$ and the potential energy, $PE$.

Conservation laws governing the pseudoenergy have been described in multiple papers (Shepherd, 1993; Winters et al., 1995; Scotti et al., 2006; Lamb, 2007). While expressions vary slightly depending on the assumptions and generalizations of the particular derivation, the true difficulty emerges in the calculation of the reference density, $\rho_0$. The ocean's density field is highly variable in time and space at a variety of scales. The fundamental difficulties in adequately capturing the variability

observationally make defining the reference state in this open environment inconclusive at best. While Shepherd (1993) discusses the possibility of using a Hamiltonian description to deal with non-resting background conditions, accounting for the non-steady nature of the ocean is a daunting problem particularly when dealing with the limited resolution of an observational system. To side-step this difficulty, reasonable approximations to the reference density are regularly employed.

For example, Hebert (1998) approximated the reference state of a sampled region by first artificially extending the length of the domain before adiabatically resorting the density. As a suitable alternative, Scotti et al. (2006) reconstructed an averaged background state that varied temporally and spatially using a combination of mooring and shipboard data. Some studies have neglected this difficulty entirely by assuming that the energy flux is reasonably approximated by $\overline{u'p'}$ where the prime denotes perturbation fields (Nash et al., 2005; Chang et al., 2006). While for small amplitude waves this may be a valid assumption, the advection of $APE$ and $KE$ density contribute significantly to the flux of large amplitude waves (Scotti et al., 2006; Moum et al., 2007a; Lamb, 2007).

The divergence of the pseudoenergy flux over a measured distance gives an upper bound to the amount of turbulent mixing that occurs in the region. This estimate provides an average quantity, and does not account for the patchiness (both vertical and horizontal) of turbulent kinetic energy (TKE) dissipation observed in NLIWs. For example, Moum et al. (2003) document rapid energy loss to turbulent mixing initiated by the onset of shear instabilities, which are typically localized at the back of the wave near the pycnocline; while Inall et al. (2000) show that for waves observed on the Malin Shelf, TKE dissipation is primarily confined to the bottom boundary layer. This paper examines pseudoenergy and TKE dissipation in NLIWs on the New Jersey shelf using observations from the Shallow Water 2006 (SW06) experiment. We first begin by introducing the experimental setup in section 5.2,

and follow by detailing the method used to calculate energies from the shipboard and mooring platforms in section 5.3. General observations are presented in section 5.4, and the temporal and spatial trends are discussed in section 5.5. Section 5.6 examines two specific examples of energy exchange, wave interactions and a wave impinging on a topographic bump. In the remainder of this manuscript we will simply refer to the energy as opposed to the pseudoenergy; however, in all cases, we are considering the sum of $KE + APE$.

## 5.2 Experimental Details

In August 2006, a wave-tracking experiment was conducted on the New Jersey shelf onboard the *R/V Oceanus*. This endeavor was part of the larger, multi-institutional NonLinear Internal Wave Initiative and Shallow Water 2006 experiment (Tang and Coauthors, 2007). Shipboard observations of velocity, density and TKE dissipation were obtained through 27 distinct wave groups at various locations across the shelf. These ship-tracked wave groups were named for bookkeeping purposes. Multiple, across-shore, environmental moorings were deployed to supplement acoustic moorings (Fig. 5.1). Most environmental moorings provided either velocity measurements, or well-resolved measurements of temperature with sparser salinity measurements. For the calculation of $E$, we selected moorings that were 1) equipped to measure water column velocity and 2) in a location where NLIWs occurred (i.e., on the shelf as opposed to the slope). Three across-shore moorings, SW30, SW37, and SW29, met these requirements (blue diamonds in Fig. 5.1). Depending on the location, shelf moorings recorded the passage of $O100$ different wave packets. A description of the environmental mooring setup is provided in Shroyer et al. (2009c), and details of the shipboard tracking experiment are discussed in Shroyer et al. (2009d).

Ship and mooring data provide two complimentary perspectives of wave groups. Shipboard observations extend over 20 km further inshore than the mooring record. Typically, the profiler was recovered after the first few waves of a group were sampled, and the ship was turned and repositioned ahead of the leading wave at the next location. The time interval between profiling periods of a particular wave group was on the order of an hour, corresponding to a horizontal distance of less than 5 km. So while the horizontal resolution allowed for the shoaling evolution of the wave groups to be captured; only the first few waves in each group were resolved. In addition, after a wave was followed inshore, we frequently elected to pass by developed wave packets on the return to the shelf break in favor of trying to capture a new wave group at an earlier stage of evolution. Mooring records completed this picture by providing localized information about the entire wave field, and, in particular, the structure of entire wave packets was resolved. Accordingly the energy analysis provided by the mooring and ship records differ.

## 5.3 Details of Energy Calculation

### 5.3.1 Shipboard Calculation

The data collected during semi-stationary times of wave profiling were used to compute the energy. Time series were converted into spatial series using the observed wave speed, $c$, measured by differencing wave position as a function of time. The kinetic energy is then straightforward to calculate using Eq. 5.1. The wave velocities are calculated by subtracting estimates of background velocity, $u_0(z)$, along isopycnals. We define $u_0(z)$ using a 5 minute time average of velocity ahead of the wave train. The available potential energy is determined following Lamb (2007)

by first calculating the available potential energy density,

$$E_{\mathrm{a}}(\vec{x},t) = g\int_{\rho_0(z)}^{\rho(\vec{x},t)} z - z^*(s)\mathrm{d}s. \tag{5.3}$$

Here, $z^*(s)$ satisfies $\rho_0(z^*(s)) = s$ for a $\rho_0(z)$ that is monotonic and stable. The $APE$ is found by integrating $E_{\mathrm{a}}$ over the desired domain. The reader is referred to Shepherd (1993), Scotti et al. (2006), and Lamb (2007) for details of the derivation of $E_{\mathrm{a}}$.

While density was directly measured through the wave, the horizontal resolution was coarse with approximately 5 profiles through a wave. Interpolation between profiles was accomplished by using acoustic backscatter from a 120 kHz Echosounder. The density structure during the experiment was approximately two-layer, with a sharp pycnocline that typically provided a consistent, strong backscatter return surface. This backscatter surface was used to define the horizontal amplitude structure of the wave, $R(x)$. The vertical structure, $\phi(z)$, of the wave was obtained by using the observed density to calculate the displacement function. Thus we are assuming the density structure is separable ($\rho(\vec{x}) = R(x)\phi(z)$); however, we make no assumptions about the analytical form of $R(x)$ and $\phi(z)$. This idealized density field is then used to estimate the "local" reference state, $\rho_0(\vec{x})$. First, the domain size is increased by a factor of 10 using the density structure ahead of the wave; the extended domain was then resorted and averaged to find $\rho_0$.

Interior wave TKE dissipation, $\epsilon$, was measured directly from shear probes. Values presented here represent averages through the wave cores, which neglect near surface ($< 10$ m) contributions. Dissipative loss attributed to the waves in the interior of the fluid, was estimated by

$$D_{int.} = \Pi\bar{\rho}\int_{x_1}^{x_2}\int_{z_L(x)}^{0} < \epsilon > dxdz, \tag{5.4}$$

where $z_L$ is the depth of maximum stratification, and the horizontal integration limits extend across the wave. The average dissipation was estimated between the same horizontal limits, and from 10-m depth to $z_L$. If it was obvious that wave dissipation extended beneath $z_L(x)$, the lower limit was extended (typically less than 5 m). $\Pi$ is a weighting factor that accounts for pre-existing turbulent dissipation. $\Pi$ is defined using the background dissipation, $\epsilon_0$, calculated from profiles taken prior to wave arrival as

$$\Pi = 1 - \frac{< \int_{40}^{10} \epsilon_0 dz >}{< \int_{40}^{10} \epsilon dz >}.$$

In the above expression, angle brackets represent the appropriate horizontal average. When $\epsilon_0$ exceeded $\epsilon$, $D_{int.}$ was set to zero.

In order to maximize the horizontal resolution, full water column profiles were made ahead of waves, while during wave passage the profiling was confined between the surface and 40-m depth. Wave profiles extended into the bottom boundary layer only in regions where the water column depth was close to 40 m. We, therefore, adopted a quadratic drag law to estimate the bottom stress, $\tau = C_D u_{10}^2$; we then use the relation $\epsilon = u_*^3(\kappa z)^{-1}$ to calculate the dissipative loss in the bottom boundary layer, $D_{bbl}$. A total of 30 profiling series, which contained measurements into the bottom boundary layer, were used to estimate a drag coefficient of $C_D = 0.002$. The total dissipative loss in the waves was then calculated as $D = D_{int.} + D_{bbl}$.

### 5.3.2 Mooring Calculation

Wave speeds, estimated by assuming a KdV correction (-10 m amplitude) to the linear phase speed, were used to convert mooring time series into a spatial series. At all shelf moorings equipped with acoustic Doppler profilers estimates of KE are made using Eq. 5.1. Wave velocities are isolated by subtracting a background velocity profile, defined as the ten-minute average prior to wave arrival, along isopycnals. Due to surface effects, the upper $\sim$ 10 m is not resolved, and a constant horizontal

velocity is assumed for near-surface extrapolation. Vertical velocity is extrapolated linearly to zero at the surface. For mode-1 depression waves maximum horizontal velocities occur at the surface, and we expect this method will bias KE estimates low.

Available potential energy is only directly calculated at mooring, SW30, due to a well-resolved density structure by mooring instrumentation (both temperature and conductivity sensors). The upper most density measurement was recorded at 14 m below the surface; data at the surface was set using the shipboard flow-through instrumentation. All data recorded within $\pm 8$ km of SW30 was averaged into half-day bins; missing data values were interpolated linearly. The half-day bin average that encompassed the start time of the leading wave was used as the surface density. In the vertical, density was extrapolated linearly between sensors and to this surface value. Other shelf moorings that were equipped to measure currents were not heavily instrumented with CTD sensors ($\leq 3$ sensors); at these moorings, the total energy is estimated using $APE \approx KE$. For this experiment, this relationship was tested using shipboard data across the shelf and was found to be robust (section 5.4). After exhausting multiple extrapolation and interpolation techniques for the unknown density field, we concluded that simply using this approximation provided the most reasonable, straight-forward estimates of total energy.

## 5.4 Ship-based Observations

During wave tracking, vertical profiling series were usually obtained through the first three waves before turning the ship and repositioning ahead of the wave group. However, we remained flexible as to the exact number of waves that were profiled through, sometimes capturing only the lead wave while at other times profiling through as many as 10 waves. The technique was adapted to the character

of the wave group and our interest at the time; for example, if the wave group appeared to be evolving rapidly, density measurements were obtained only through the first 1-2 waves so that the ship could be repositioned as quickly as possible. On the other hand, if profiling occurred near an environmental mooring the series was often extended to allow for detailed comparison of mooring and shipboard data. Energies and mixing parameters were calculated for all waves that were profiled through at each position and time, totaling just over 500 wave "realizations".

### 5.4.1 Energy

Distributions of the observed, ship-based $E$ are shown in Fig. 5.2a. The average $E$ was 0.6 MJ m$^{-1}$, and observed values spanned three decades from $2 \times 10^4$ J m$^{-1}$ to $7 \times 10^6$ J m$^{-1}$. In general, the $KE$ was approximately equal to the $APE$ (Fig. 5.3a). While variability is present, this trend seems to exist in multiple geographic regions for both depression and elevation waves. Accordingly, equipartition of energy may serve as a reasonable approximation if only one component is known. While equipartition violates the relation $KE > APE$ predicted by fully nonlinear theory (Turkington et al., 1991), we argue that the approximation is useful in estimating energies in the ocean for the following reasons. First, the necessary, well-resolved measurements in both the time and space domain are difficult to acquire; even under the best of circumstances, data extrapolation and interpolation is required. Second, as discussed previously, defining the reference density from limited measurements in an open environment is problematic. The combination of these two factors make error estimates of calculated energy difficult to quantify. To attain some measure of the error associated with the first concern, we created KdV solitons for several of the observed background states. "True" energies were estimated from complete soliton fields. Solitons were then sampled in a manner consistent with ship-based observations, and energies were re-calculated. Resultant

estimates indicate that reasonable errors are typically around 25%, a value which in many cases could easily distort the true ratio between $KE$ and $APE$. Note that this error does not account for unknown $\rho_0$.

At the NJ site, the ratio of $KE$ to $APE$ varied from 0.27 to 3.6 for individual waves. This spread may partially be attributed to the sources of error discussed above, i.e., extrapolation, interpolation and (most importantly) estimation of $\rho_0$. Ten-km bin averages, which help to minimize random error, show little range in this ratio with an offshore value of 1.1 and an inshore value of 0.9 (Fig. 5.3b). Inshore, even this highly-averaged value of $KE : APE$ departs from fully nonlinear theory. However, application of this theory, which neglects dissipation and assumes 2d waves, is questionable as wave begin to shoal in dynamic coastal environments. Recent numerical experiments by Lamb and Nguyen (2009) verify the departure from the relation $KE > APE$ for shoaling waves. A similar trend was noted by Scotti et al. (2006) in Massachusetts Bay, where estimates of the average available potential energy density exceeded the average kinetic energy density at an inshore mooring.

Another trait of linear waves (and nonlinear waves that propagate without change in form) that is experimentally verified for these nonlinear counterparts is the relation, $\overline{F} = c\overline{E}$ (Fig. 5.4). Here the energy flux, $F$, is equal to the sum, $up' + uE_{\mathrm{a}} + uE_{\mathrm{k}}$, where $E_{\mathrm{k}} = \overline{\rho}(u_w^2 + w_w^2)/2$ is the kinetic energy density. The perturbation pressure consists of a nonhydrostatic component, hydrostatic component, and surface term (Moum et al., 2007a). Figure 5.4 is an extension of Moum et al. (2007a) Fig. 18 in that the waves presented here encompass both depression and elevation waves in a different geographic region. For the NJ waves, $\overline{up'}$ is approximately twice $\overline{u(E_{\mathrm{a}} + E_{\mathrm{k}})}$; this result is exactly opposite the case of the Oregon shelf waves documented in Moum et al. (2007a).

### 5.4.2 Turbulent Mixing

The distributions of $\epsilon$ (Fig. 5.2b) were based on measurements from 10-40 m depth. The mean value of $\epsilon$ in the waves was $10^{-6}$ W kg$^{-1}$; localized values exceeded $10^{-4}$ W kg$^{-1}$. The median, $\mu_{1/2}(\epsilon)$, was $6\times10^{-9}$ W kg$^{-1}$. The qualitative character of wave mixing differed considerably, and can be classed into three categories: I. high, localized dissipation, II. patchy, elevated dissipation, and III. low dissipation (Fig. 5.5). In all cases, observations of high, localized dissipation were located on the trailing edge of waves and coincided with low Richardson number. These qualities along with billow-like structures in backscatter images point to turbulence generated from shear instabilities. Category I waves were of larger amplitude (exceeding -10-m displacements compared to an average observed amplitude displacement of -8 m), and the highest dissipation rates ($> 10^{-4}$ W kg$^{-1}$) were observed in this category. Category II waves displayed elevated dissipation that was distributed throughout the wave core, in regions of high and low shear. This type of observation was the most common, and while dissipation was elevated, values were not typically as large as those observed in the first category. The third category is comprised of waves with very low dissipations (first column, Fig. 5.5) and waves with $D_{int.} = 0$, i.e. the interior background dissipation exceeded wave dissipation (Eq. 5.4). Category III waves were both large and small amplitude. The example waves shown in Fig. 5.5 were selected because the series illustrates that the character of mixing is not directly related to amplitude and evolves quickly in time. Also, we can imagine one possible story as to the development of multiple categories based on this series, with the onset of shear instability and development of turbulent billows (Category I), the growth of the billows and energy cascade to smaller scales (Category II), and the eventual damping of dissipation as the energy source of the turbulence is depleted (Category III).

## 5.5 Long-term Trends

An exceptional feature of the NJ shelf NLIW field is its variability, which was manifested over the duration of the experiment over a variety of temporal and spatial scales. In the time domain, the larger-scale variability was dominated by a period from the 16-22 August 2006 in which NLIW energies were an order of magnitude larger than at other times during the experiment. Spatially, the leading three waves in a group were observed to grow over 30 km across the outer shelf. This period of growth was followed by energy loss, as the waves began to be influenced by the shoaling bottom. Average values of turbulent mixing parameters did not display the range in variability present in wave energies.

### 5.5.1 Temporal Variability

The observed wave energies varied considerably in time, with larger amplitude, more energetic waves occurring after 16 August 2006 (Fig. 5.6). This time period was not related to the barotropic spring tidal cycle, but instead corresponded to a time of increased shoreward, internal energy flux (Nash et al., 2009). This period also coincided with the onset of upwelling winds and a shift in mesoscale stratification at the shelf break (Shroyer et al., 2009c). Mooring time series, which have the advantage of resolving all NLIWs at one location, are used to highlight the temporal variability (Fig. 5.6a), although shipboard data also show the change (Fig. 5.6b). The energy increase corresponded to an increase in the average amplitude of the waves, and essentially changed the shoaling process, as these large amplitude waves were observed to change polarity (Shroyer et al., 2009d), whereas smaller waves dissipated before reversal was observed.

Shipboard observations allow for the temporal variability in turbulent mixing to be explored. Estimates of $\epsilon$ were 55% greater during the period of large amplitude

waves (Fig. 5.7a), and the average turbulent diffusivity, $K_\rho$, was 70% greater over this same time period (Fig. 5.7b). $K_\rho$ was calculated using

$$K_\rho \equiv \frac{\Gamma\epsilon}{N^2}. \tag{5.5}$$

$N^2$ is the buoyancy frequency, and $\Gamma = .2$ is the mixing efficiency (Osborn, 1980). The turbulent mixing is thus only about a factor of two larger between the two time periods, whereas energies exhibit a factor of ten difference.

### 5.5.2 Spatial Variability

While shipboard observations do not capture the complete wave train, the data set is unique in that it allows for evaluation of the across-shelf evolution of wave energetics. For this analysis, we evaluate the total energy in the leading three waves of each group; and, all references to energies and dissipative loss in the remainder of this section are calculated for the three leading waves. This number was selected because i) integrating over several waves "filters" the short term changes discussed in the section 5.6 and ii) in most cases this was the minimum number of waves profiled through before the ship was re-positioned. If less than three waves were profiled though, the energy was weighted appropriately. (E.g., if at a location only two waves were documented the total energy was multiplied by 3/2 in order to approximate the energy in three waves.) A clear trend exists as leading waves initially grow in energy (amplitude) as they propagate onshore; at approximately 20 km inshore of the T-axis of the mooring array, loss to dissipation (both in the bottom boundary layer and the interior) results in wave decay. This result is based on observations from 16 of the 27 ship-tracked wave packets, leaving 11 "unused" wave packets. Of the total 27, five groups were tracked using only acoustics, precluding direct measurement of $APE$ and more importantly $\epsilon$. Another four wave groups

were profiled through at only one station. One of the other two wave groups was a mode-2 packet (*Wave Jasmine*) whose energetics are explored in Shroyer et al. (2009b), and the final exception, *Isaac*, is discussed in section 5.6.

Figure 5.8a shows $E$ summed over the leading three waves at each profiling series of the remaining 16 wave packets. Individual profiling sites of the larger amplitude wave groups, which dominate the trend, are connected with thin black lines. Note that the bin average (red-blue line) is representative of these individual wave packets. Mooring energies calculated for the ship-tracked wave groups are indicated with yellow diamonds. The difference is likely attributed to the extrapolation of velocity data to the surface required for mooring records. *Wave Rosey* stands out as an anomaly, and is not included in the bin-averaged line. This wave was amplitude limited and is discussed in detail in Shroyer et al. (2009c).

We define the energy supply in the waves as

$$\text{Energy Supply} = \frac{dE}{dt} + D.$$

When this quantity is zero either (i) $E$ does not change, or (ii) decay is balanced by dissipative loss. The energy supply for all wave groups (excepting Rosey) is shown in Fig. 5.8b. As may be expected, the region of energy growth is associated with a supply that is greater than zero, i.e. energy is added to the system. In the region of wave decay the energy supply is on average near zero, indicating a balance between decay and turbulent dissipation. Caution should be exercised when considering individual "points" of energy supply, as this quantity can be largely influenced by localized values of high dissipation. This quantity should in reality be viewed as an average over a larger scale as opposed to an exact balance at a specific point, since the true temporal and spatial extent of mixing events is not known (i.e., observations only provide a snapshot).

#### 5.5.2.1 Growth

The observed growth of the first few waves of a packet likely occurred at the expense of energy from the bore-like component of the internal tide. Nonlinearity prohibits a simple, additive separation of wave and bore energy; and yet, the temperature records at SW30 and SW29 provide evidence of this exchange. Note that SW30 was located at 0 km, slightly inshore of the NLIW formation region (Shroyer et al., 2009c) and at the beginning of the growth trend (Fig.5.8). On the other hand SW29, located at -21 km, was positioned at the average "peak" wave energy that occurred just prior to decay. At SW30 isotherms typically maintained a bore-like offset long after the passage of the leading waves, while at SW29 isotherms returned to near rest positions within a relatively short period of time. This trend was noticeable in a majority of the wave packets, and in particular was a robust feature of larger-amplitude, ship-tracked waves that dominate the trend presented in Fig. 5.8a.

To quantify the bore density offset, displacements were calculated for thermistors located near 20 m depth using

$$\eta = \frac{T'}{\overline{\partial T/\partial z}},$$

where, $T'$, is the perturbation temperature and $\overline{\partial T/\partial z}$ is the mean temperature gradient centered at 20 m. This depth was selected due to its proximity to the average pycnocline depth, where maximum displacements are expected to occur. Furthermore, sensors above this depth gave unreliable wave displacements due to the (nearly) unstratified surface water. Displacements were calculated for 3 hours after passage of the leading wave at both SW30 and SW29. Only those waves that could be reliably tracked between these two moorings were used in this analysis. A crude estimate of the bore displacement was then obtained by taking the minimum

displacement over 25-minute bins. An example calculation is shown in Fig. 5.9a for *Wave Anya*. Solid lines show estimated total displacements, and dashed lines represent the bore component at SW30 (black) and SW29 (grey). A change in the bore displacement was then calculated by subtracting, $\Delta\eta = < \eta_{29}^{bore} > - < \eta_{30}^{bore} >$, so that a positive $\Delta\eta$ indicates a larger bore at SW30. Here the angle brackets denote averages over 1.5 and 3 hours. The results for the largest six, ship-tracked waves are presented in Fig. 5.9b. In all cases, $\eta_{30}^{bore}$, exceeded $\eta_{29}^{bore}$. *Rosey* once again stands out as anomaly with a bore component 2-3 times larger than those of the other waves. Extending the analysis to other NLIW packets recorded in the mooring data shows a general trend in which larger values of $\Delta\eta$ correspond to larger wave energies at SW29 (Fig. 5.9d).

The energy transfer from the bore to the NLIWs results in amplitude growth and an increase in number of the waves between SW30 and SW29. This story is not unique and has analogues in other regions (e.g. Colosi et al., 2001; Ramp et al., 2004; Moum et al., 2007a). What is perhaps surprising is despite this dependence on being physically linked to the internal tidal bore, the arrival times at SW30 were not phased with the across-shelf barotropic M2 velocity at the shelf break (Fig. 5.9c). Only for the time period between the 17-22 August 2006 were arrival times regular. This time period was also notable in that wave groups were consistently of larger amplitude. However, even for the six ship-tracked wave groups that are detailed in Fig. 5.9b, arrival times relative to peak across-shelf M2 velocity varied by roughly 6 hours (grey diamonds in Fig. 5.9c). We attribute this variability to the irregularity of the internal tide on the shelf (Shroyer et al., 2009c; Nash et al., 2009). We note that preliminary modelling efforts of a simple barotropic tide result in a similarly sporadic NLIW field on the shelf with much of the shoreward baroclinic energy flux emerging from the canyon just south of the mooring line (personal communication, Alberto Scotti). Complicating matters on the shelf is the refraction of northward

energy flux apparent in the model and supported by mooring data (Nash et al., 2009).

#### 5.5.2.2 Decay

Waves reached maximum amplitudes/energies at approximately 40 km inshore of the shelf break (x=-20 km). Past this location, a general balance between wave decay and dissipative loss was maintained (Fig. 5.8). Of the 16 waves plotted in Fig. 5.8, 13 were followed into the decay regime. (The remaining three groups were small amplitude with the peak energy, $E_{max}$, in the leading three waves approximately equal to 0.5 MJ m$^{-1}$ for each group.) The average wave decay, $-dE/dt$, was calculated using a least squares fit to a linear trend over the period of energy loss. As may be expected, based on the general balance between the local energy loss and turbulent dissipation (Fig. 5.8b), this average measure of decay balances the average dissipative loss (Fig. 5.10a).

While at a specific time there is not a direct relationship between wave energy and TKE dissipation (Fig. 5.5), the average decay, and consequently the dissipative loss, scales with $E_{max}$ (Fig. 5.10b), so that larger waves lose energy more rapidly than the smaller waves. A similar trend was noted by MacKinnon and Gregg (2003) to the north of the present study site. A simple linear regression of $dE/dt$ on $E_{max}$ results in a decay scale of $-24 \times 10^{-6}$ s$^{-1}$ with an $R^2 = 0.88$. Using the average wave speed (0.8 m s$^{-1}$), the decay time scale is equivalent to a length scale of about 35 km. Larger waves that typically exhibited larger wave speeds will have longer decay length scales than smaller waves. Since SW29 was located near the region of maximum energy for the ship-tracked waves, we extend this analysis to all NLIWs observed at this mooring. The resultant daily averages of $D$ are shown in Fig. 5.11.

Average dissipative loss was also calculated using the flux divergence, $\partial F/\partial x$, assuming that all NLIW energy was dissipated 40 km inshore of mooring SW29.

Daily averages of $D$ based on $\partial F/\partial x$ are compared to that estimated from the scaling discussed above in Fig. 5.11. In general, the two methods agree well, although the peak on 19 August 2006 calculated from the scaling is less than that estimated using the flux divergence. Given the relation, $c\overline{E}=\overline{F}$, these two estimates are not completely independent. For this calculation the pressure work component of $F$ was calculated by mapping "nearby" (in time and space) ship-based profiles onto streamlines, and $E$ was estimated as $2KE$ as discussed in section 5.3. The details of selecting a density profile are not important; however, since the flux divergence calculation includes more information than just $E$, upon which the scaling analysis depends, the agreement between average $D$ based on these two methods is encouraging. Finally, while this scaling is not directly applicable to other geographic regions, the decay time and length scales of the waves may provide a useful comparison to NLIWs in other areas.

## 5.6 Short-term Variability

Imposed on the larger scale trends discussed above are short episodes (both in time and space) of rapidly evolving wave energetics. Here, we present two examples of short-term energy exchange between NLIWs. The first details two sequences associated with the interaction of individual waves. In both cases, large shear instabilities grow as a result of wave collisions. These events are associated with a sudden increase in $E$ as the waves run into each other, followed by an extreme drop in $E$ associated with loss to turbulent production, combined in one case with the "re-separation" of the wave. As a second example we detail the evolution of one wave group, *Isaac*, that encountered a small topographic rise. The combination of an abrupt change in topography along with the onset of strong, opposing barotropic currents greatly affected wave structure, energy, and dissipation.

### 5.6.1 Wave Interactions

The convergent region at the leading edge and the divergent region at the trailing edge of surface-trapped, depression waves modulate small gravity waves, creating alternating bands of rough and smooth water, and providing a means of remotely observing NLIWs. Remote imagery (e.g., Tang and Coauthors, 2007, Fig. 2) and shipboard radar images from the SW06 study site often show cusp-shaped interference patterns that are attributed to interactions between multiple wave groups. Wave interactions may occur between packets that are oriented at different angles or between waves of the same packet. If a leading wave is of smaller amplitude than a trailing wave, weakly nonlinear theory predicts that the larger amplitude wave will overtake the smaller wave. The waves will pass through one another without change in form or wave speed; and the only evidence of the interaction is a change in phase of the two waves, i.e. the larger amplitude wave is advanced slightly, while the smaller wave is impeded as the waves exchange position (Drazin, 1984). While the assumptions for weakly nonlinear waves are not expected to hold for the observed waves, the outcome of wave-wave interactions may be qualitatively similar. Observations acquired during this wave tracking experiment provide in-situ evidence of both interactions between multiple wave packets and interaction between waves of the same group.

#### 5.6.1.1 Group-Group Interactions

The X-band radar imagery (Figure 5.12) provides a clear illustration of the intersection of two distinct wave packets. Wave directions (indicated by white arrows) were calculated by computing the average propagation angle over 1 hour from data images (120 images) surrounding the snapshots shown in Figure 5.12. Initially the northern packet had a heading of approximately 290°, and the southern packet maintained a heading of about 310°. Around -20 km the two packets are difficult

to distinguish in the radar imagery and a combined heading of 300° is estimated for the resultant interference pattern. Unfortunately, past approximately -30 km the radar signature of the NLIWs deteriorated rapidly. During the profiling period near -10 km, velocity data allow for minimization of the along wave front velocity component to determine wave orientation. Applying this method to the two lead waves, we find that the first wave propagated with a heading closer to 290° as compared to the second wave's heading of 300°. While the difference is small, it is clearly distinguishable in the velocity data; however, inshore of this location, computation of a difference in wave orientation using velocity data is ambiguous, which is consistent with radar imagery.

Beneath the surface, acoustic backscatter imagery provides a complimentary perspective of the group interaction (Fig. 5.13 a). In this sequence, the larger amplitude leading wave of the trailing group catches up to the leading wave of the first group, forming a very large amplitude ($\sim 20m$) wave at -16.5 km. In contrast to weakly-nonlinear theory, which predicts that the waves should pass one another with only a change in relative phase, the observed waves do not continue independently of one another. Perhaps surprisingly, the large amplitude composite wave separates into two waves with the smaller amplitude wave taking the lead. Inshore of -19 km, these two leading waves were seemingly linked and continued through the shoaling process together (Shroyer et al., 2009d).

Energy analysis are consistent with the proposed interaction (Fig. 5.13c, blue diamonds). The total energy for the lead disturbance of *Wave Tonya* at -12.5 km was 1.5 MJ $m^{-1}$ (T1), and the total energy in the second wave (T2) at this same location was 1.4 MJ $m^{-1}$. The combination (T1+T2) equal to 2.9 MJ $m^{-1}$ was approximately the same as the leading (combined) wave energy (3.1 MJ $m^{-1}$) at -16.5 km. After the intersection, approximately half of the energy (1.7 MJ $m^{-1}$) was redistributed into two smaller waves (T1' and T2'). The remainder (1.4 MJ $m^{-1}$

lost over 1.2 hours) was lost to turbulent dissipation, $D = 340\text{W m}^{-1}$, at -16.5 km.

#### 5.6.1.2 Wave-Wave Interactions

Backscatter images for *Wave Wyatt* also show evidence of a wave interaction (Fig. 5.13b). However, unlike *Tonya*, neither radar imagery nor velocity data suggest disparate orientations for the first and second waves that combine to form the large amplitude wave at -21 km, indicating that these two waves were likely part of the same wave group. Modeled NLIW trains are known to establish packets that are rank ordered, larger amplitude waves traveling faster. The amplitude of the second wave (W2) was greater than the first (W1) at -16.5 km (Fig. 5.13b, right panel), indicative of a faster phase speed and possibly allowing the second wave to overtake the first. Using backscatter transects from -16 to -20 km a difference in phase speed of 0.07 m $\text{s}^{-1}$ was estimated between the second and first wave, assuming that the two waves collided near -19 km. Calculating the difference in weakly nonlinear phase speed due solely to the different amplitudes of W1 and W2 near -16 km, we find a predicted $\Delta c = 0.1$ m $\text{s}^{-1}$. Analysis of radar imagery in this same range confirms an increase in phase speed of the second wave of about 0.06 m $\text{s}^{-1}$. However, a clear interaction between the waves is not distinguishable using shipboard radar images due to a deterioration in the clarity of the fronts in the backscatter return. The change in the backscatter signal may have been linked to the interaction, which would blur the typical pattern of surface convergence-divergence through the wave train thus effecting the character of the radar return signal.

An energy analysis similar to that given for *Wave Tonya* was performed for *Wave Wyatt* (green diamonds, Fig. 5.13c). The sum of the total energy of the first two waves (W1+W2) at -16.5 km was 3.8 MJ $\text{m}^{-1}$, which was in agreement with the total energy of the lead wave at -19.5 km (3.5 MJ $\text{m}^{-1}$). Continuing this

analysis to -22 km, we find that the sum of the energy of the first two waves at -19.5 km was 4.7 MJ $m^{-1}$; this value agrees with the total $E$ of the lead wave at -22 km (4.9 MJ $m^{-1}$). Hence, we theorize the lead wave at -22 km is actually resultant from the combination of the first three waves (W1+W2+W3) near -16 km (Fig. 5.13b). The leading wave at -22 km loses almost all of the energy gained during this interaction to the intense mixing event ($> 600$ W $m^{-1}$) that followed (Figure 5.14); and in contrast to *Wave Tonya*, the combined wave never re-separates into multiple waves.

The asymmetry in the leading wave at -21 km was pronounced; and the rear face was extremely steep, possibly approaching the breaking limit. However, the breaking criterion defined by Vlasenko and Hutter (2002) was not met; hence kinematic instability was unlikely. On the contrary, examination of the Richardson number criterion shows that the severe deformation of the lead wave past this point (onshore panel in Fig. 5.13b) may have been the result of shear instability. The inverse Richardson number through the lead wave at -19.5 km is shown in Figure 5.14a, regions greater than 4 that support the development of shear instabilities are contoured in white. The values were calculated using 1-m density and velocity bins. Figure 5.14b emphasizes the extremely large values ($> 10^{-4}$ $m^2 s^{-3}$) of turbulent dissipation present during this time period. High resolution ($O$(cm)) density profiles, reveal the existence of density overturns (Fig. 5.14c) with an average $L_T \sim 1.3$ m and maximum $L_T \sim 2.5$ m through the latter portion of the wave.

### 5.6.2 Wave over a bump

*Wave Isaac* was first observed on 0850 UTC 10 August 2006, as the leading wave began to overtake a second wave group, *Holly*. Initially, *Isaac* was observed to travel at $-0.8$ m $s^{-1}$ with average amplitudes of -8 m, as compared to a speed of $-0.65$ m $s^{-}1$ and amplitudes near -4 m for *Holly*. Unlike the example of the group-

group interaction discussed above for *Tonya*, *Holly* and *Isaac* seemed to propagate independent of one another. The difference may be attributed to either the relatively weak nature of *Holly* or to the large differences in wave heading. *Isaac* propagated with a heading of 310°, and *Holly* maintained a heading of 335°, resulting in a difference of 25°. Due to the character of the two wave groups, the ship abandoned *Holly* in favor of following the more energetic, *Isaac*.

At 1200 UTC 10 August 2006, the leading wave of *Isaac* encountered a topographic bump in 60 m of water (Fig. 5.15). The bump had a steepness of $7 \times 10^{-3}$, with a rise of 20 m over a 3 km distance. This value can be compared to a slope of $5 \times 10^{-4}$ across most of the shelf. As *Isaac* approached the bump the tidal amplitude, $\eta_0$, was near a peak, corresponding to a shift from onshore to offshore barotropic tidal velocity. During this time profiles of the background velocity, $u_0$, switched from having an onshore velocity component at depth to being directed offshore at all depths, and the observed onshore wave speed slowed to $-0.3$ m s$^{-1}$ (upper inset, Fig. 5.15). In order to estimate the role of bottom shoaling in the reduction of the shoreward linear wave speed, $c_0$ was calculated using the Taylor-Goldstein equation for i) a quiescent fluid and ii) the fully stratified, sheared background. For the first case, the linear wave speed decreased by only 10%. We conclude, therefore, that $u_0$ is the primary control on the changing wave speed. Comparison of the change in the barotropic velocity, 0.39 m s$^{-1}$, to the change in $c_0$ with shear, 0.44 m s$^{-1}$, emphasizes the importance of advection.

The increase in the depth-averaged $u_0$ can be attributed to two factors. First, as mentioned above the barotropic tidal velocities were moving toward peak offshore amplitudes during the observed time period. The maximum tidal height was achieved at the time that *Issac* was located at the black triangle in the upper inset of Fig. 5.15. Over the duration of the wave's transit, offshore tidal velocities continued to increase. Second, mass conservation requires an increase in the barotropic

velocity as the water column depth decreases over the top of the bump. This second effect, results in an across-shore gradient in $u_0$, which we theorize contributed to the structural and energetic evolution of the wave packet. At any given time, the leading wave, which was always in the shallowest water, encountered the strongest values of $u_0$, and as a result the waves was arrested as it approached the crest. However, even in a quiescent fluid this topographic feature would influence the form of the wave. Indeed, the final two backscatter images show a broadening of the leading wave's front face, an anticipated artifact of shoaling.

The total energy integrated over a distance of 750 m from the leading edge of the first wave more than doubled as the waves appeared to "pile-up" on the bump (middle inset, Fig. 5.15). The integration limit was set by the minimum transect distance during this time. The convergence of wave energy was accompanied by increased loss to turbulent mixing (bottom inset, Fig. 5.15). While the estimate of dissipation includes a contribution from $D_{bbl}$, the signal is dominated by $D_{int.}$, likely associated with shear instabilities. The billows on the trailing edge of the leading wave at -48.5 km were well developed. Thus the presence of this localized topographic feature impacts the energetics of *Isaac* in a similar way that wave interactions induced changes for *Tonya* and *Wyatt*, i.e., energy growth followed by dissipative loss to shear-driven turbulence. While only one wave was followed onto the bump, it is possible that any wave encountering this feature under similar background conditions would undergo an analogous transformation. Thus this regional topographic feature may be a geographically, localized area of intense NLIW mixing. Note that this discussion has neglected effects associated with reflection and three-dimensional motions. The latter consideration may be of particular importance, since the length scale of the bump is smaller than the along-crest length scale of the NLIWs.

## 5.7 Summary

An analysis of NLIW energetics on the New Jersey shelf is presented. Average wave energies were on the order of a MJ $m^{-1}$, and in general a balance between the $KE$ and $APE$ existed. This balance seemed to hold regardless of location on the shelf, and the spread was primarily maintained within a factor of three. Defining the reference density is the main source of error in calculation of the $APE$, and the approximation, $KE \approx APE$, could serve as a simple and useful estimate. The character and magnitude of TKE dissipation in the waves varied considerably. Waves were classified as having either i) low dissipation, ii) patchy, elevated dissipation, or iii) high, localized dissipation. A direct relationship between the character/magnitude of dissipation and wave energy could not be established on a per wave basis.

The NLIW field was highly variable over the experiment duration. Larger amplitude waves were observed between the 16-26 August 2006. These waves exhibited a ten-fold increase in wave energy, whereas the turbulent mixing increased by only a factor of two. Spatially, the leading three waves in a packet were observed to grow in energy across the outer shelf region, after which energy decay was approximately balanced by dissipative loss. Growth is thought to occur at the expense of the bore-like nature of the internal tide, with larger bore displacements typically resulting in larger amplitude waves. Decay was attributed to both losses in the interior of the water column and in the bottom boundary layer, although loss was dominated by $D_{int.}$. The ratio $D_{int.}/D_{bbl}$ varied from median values of 50 on the outer shelf to 3 on the inner shelf. The total, average $D$ for a wave group scaled with the peak energy over the decay region. The resultant decay time scale is approximately 12 hours, corresponding to a length scale of 35 km (100 wavelengths). Short-term, rapid energy exchanges were documented as a result of wave interactions as well as a wave group impinging on a small topographic bump. In both examples, the outcome was

a significant energy loss to turbulent mixing generated via shear instabilities.

## 5.8 Acknowledgments

This work was funded by the Office of Naval Research. We thank the Captains, crew and marine technicians of the R/V Oceanus and R/V Knorr for their assistance in the implementation of the ship tracking experiment and the successful deployment and recovery of moorings. Mike Neeley-Brown, Ray Kreth, Alexander Perlin, Greg Avicola, and Sam Kelly helped in obtaining the ship-based observations; and John Kemp, James Lynch, and James Irish were responsible for managing the mooring component.

## Bibliography

Chang, M.-H., R.-C. Lein, T. Y. Tang, E. A. D'Asaro, and Y. J. Yang, 2006: Energy flux of nonlinear internal waves in northern South China Sea. *Geophys. Res. Let.*, **33**, doi:doi:10.1029/2005GL025196.

Colosi, J. A., R. C. Beardsley, J. F. Lynch, G. Gawarkiewicz, C.-S. Chiu, and A. Scotti, 2001: Observations of nonlinear internal waves on the outer New England continental shelf during the summer Shelfbreak Primer study. *J. Geophys. Res.*, **106**, 9587–9601.

Drazin, P. G., 1984: *Solitons*. Cambridge University Press, second edition, 40–67 pp.

Hebert, D., 1998: The available potential energy of an isolated feature. *J. Geophys. Res.*, **93**, 556–564.

Inall, M. E., T. P. Rippeth, and T. J. Sherwin, 2000: Impact of nonlinear waves on the dissipation of the internal tidal energy at a shelf break. *J. Geophys. Res.*, **105**, 8687–8705.

Lamb, K. G., 2007: Energy and pseudoenergy flux in the internal wave field generated by tidal flow over topography. *Cont. Shelf Res.*, **27**, 1208–1232.

Lamb, K. G., and V. T. Nguyen, 2009: Energy flux in internal solitary waves with an application to reflectance. *J. Phys. Ocean.*, **39**, 559–580.

MacKinnon, J. A., and M. C. Gregg, 2003: Mixing on the late-summer New England shelf – solibores, shear and stratification. *J. Phys. Ocean.*, **33**, 1476–1492.

Moum, J., J. Klymak, J. Nash, A. Perlin, and W. Smyth, 2007: Energy transport in nonlinear internal waves: Experimental determination. *J. Phys. Ocean.*, **37**, 1968–1988.

Moum, J. N., D. M. Farmer, W. D. Smyth, L. Armi, and S. Vagle, 2003: Structure and generation of turbulence at interfaces strained by internal solitary waves propagating shoreward over the continental shelf. *J. Phys. Ocean.*, **33**, 2093–2112.

Nash, J. D., M. H. Alford, and E. Kunze, 2005: On estimating internal wave energy fluxes in the ocean. *J. Atmos. Ocean. Tech.*, **22**, 1551–1570.

Nash, J. D., E. Shroyer, J. Moum, T. Duda, H. Graber, J. Irish, and J. Lynch, 2009: Mesoscale influences on the generation of the internal tide and nonlinear internal waves over new jerseys continental shelf. *J. Phys. Ocean.*.

Osborn, T. R., 1980: Estimates of the local rate of vertical diffusion from dissipation measurements. *J. Phys. Ocean.*, **10**, 83–89.

Ramp, S. R., T.-Y. Tang, T. F. Duda, J. F. Lynch, A. K. Liu, C.-S. Chiu, F. Bahr, H.-R. Kim, and Y. J. Yang, 2004: Internal solitons in the northern South China Sea Part I: sources and deep water propagation. *IEEE J. Oceanic Engin.*, **29**, 1157–1181.

Scotti, A., R. Beardsley, and B. Butman, 2006: On the interpretation of energy and energy fluxes of nonlinear internal waves: An example from Massachusetts Bay. *J. Fluid Mech.*, **561**, 103–112.

Shepherd, T., 1993: A unified theory of available potential energy. *Atmos.–Ocean*, **31**, 1–26.

Shroyer, E., J. Moum, and J. Nash, 2009a: A description of the nonlinear internal wave field over New Jersey's continental shelf. *J. Geophys. Res.*, **submitted**.

— 2009b: Mode-2 waves on the continental shelf: ephemeral components of the nonlinear internal wave field. *Geophys. Res. Let.*, **submitted**.

— 2009c: Observations of polarity reversal in shoaling nonlinear internal waves. *J. Phys. Ocean.*, **39**, 691–701.

Tang, D. J., and Coauthors, 2007: Shallow Water '06. *Oceanography*, **20**.

Turkington, B., A. Eydeland, and S. Wang, 1991: A computational method for solitary internal waves in a continuously stratified fluid. *Studies in Applied Mathematics*, **85**, 93–127.

Vlasenko, V., and K. Hutter, 2002: Numerical experiments on the breaking of solitary internal waves over a slope-shelf topography. *J. Phys. Ocean.*, **32**, 1779–1793.

Winters, K., P. Lombard, J. Riley, and E. D'Asaro, 1995: Available potential energy and mixing in density-stratified fluids. *J. Fluid Mech.*, **289**, 115–128.

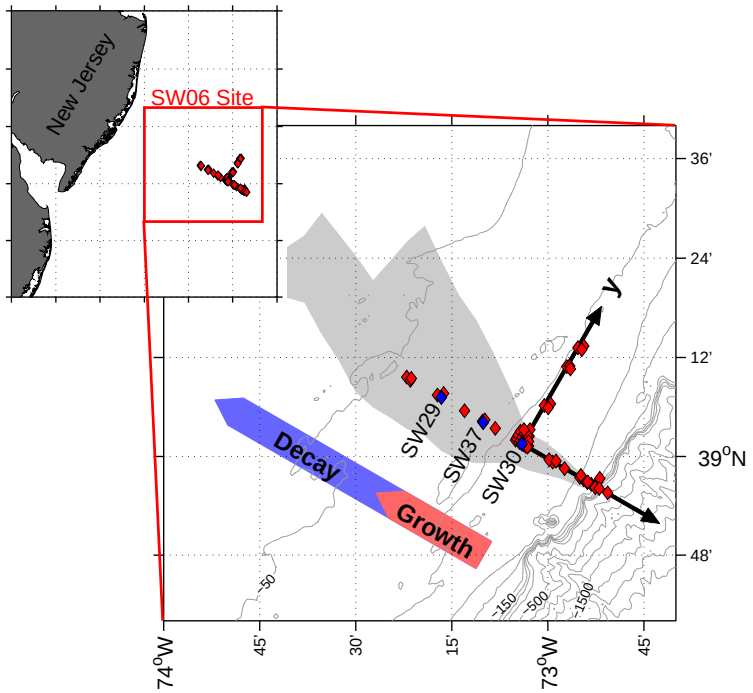


FIGURE 5.1: Site bathymetry and mooring locations (red diamonds). The grey cloud encompasses the ship transect boundary. Blue diamonds show the across-shelf environmental moorings that were used in this analysis. Coordinate axes are defined with black arrows; and colored arrows estimate the regions of wave growth and decay.

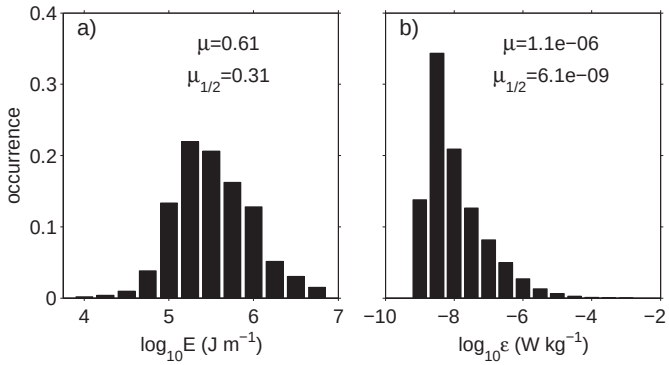


FIGURE 5.2: The frequency distribution of a) wave energy and b) dissipation in waves between 10-40 m depth. The means, $\mu$, and medians, $\mu_{1/2}$, are given; all distributions are calculated from shipboard data.

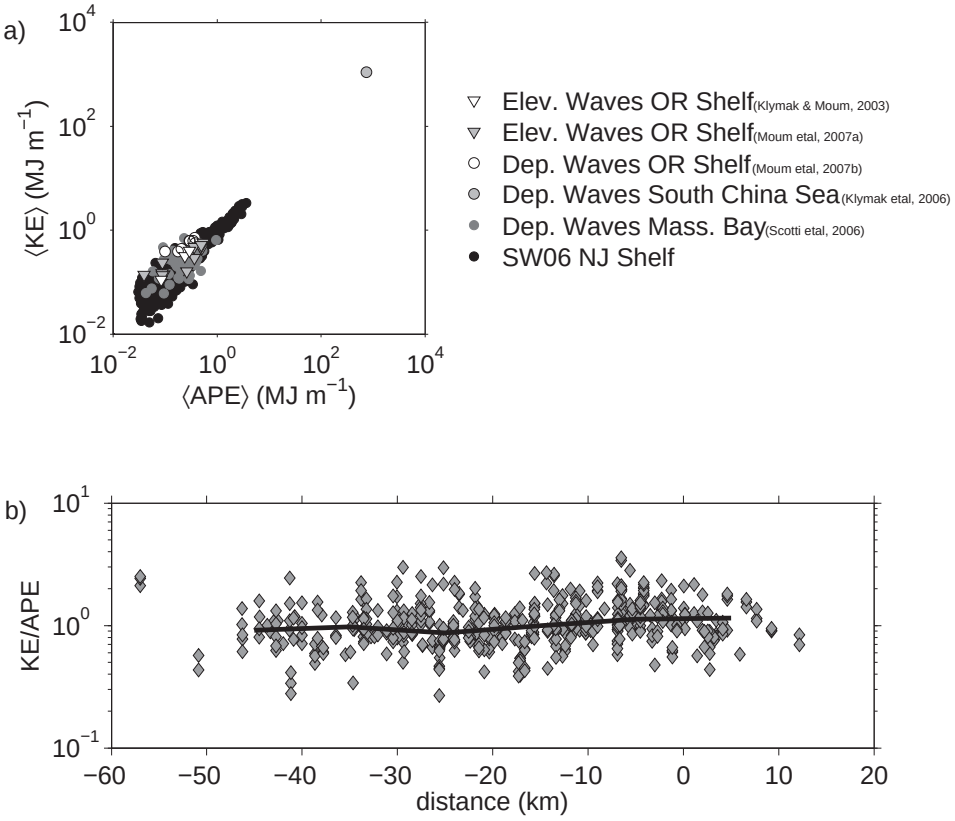


FIGURE 5.3: a) Ratio of $KE$ and $APE$ for the current study (black dots), as well as several other experiments. Data are from a variety of locations and include both elevation and depression waves. b) Ratio of $KE$ to $APE$ as a function of across shelf distance for the NJ shelf waves. The black line is the 10 km-bin average.

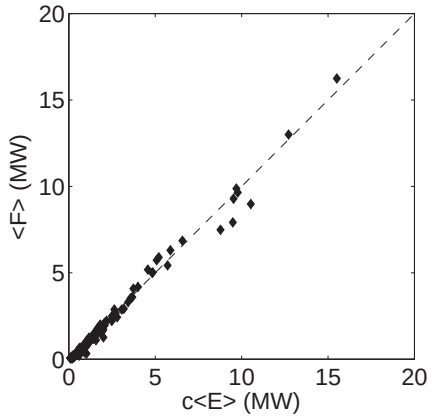


FIGURE 5.4: Average energy flux versus the product $c\overline{E}$. The dashed line plots $\overline{F} = c\overline{E}$.

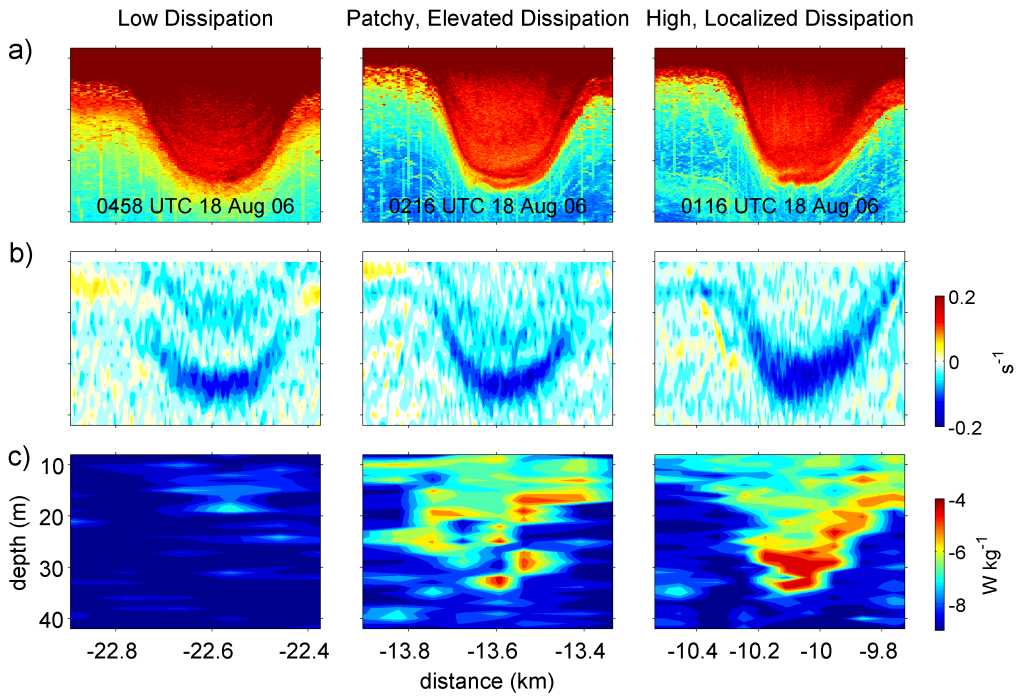


FIGURE 5.5: a) Acoustic backscatter, b) vertical shear, and c) $\log \epsilon$ for the leading wave of the same train at three different times/locations. Both the character and magnitude of the observed dissipation differ greatly despite the fact that shear magnitudes and wave amplitudes are similar.

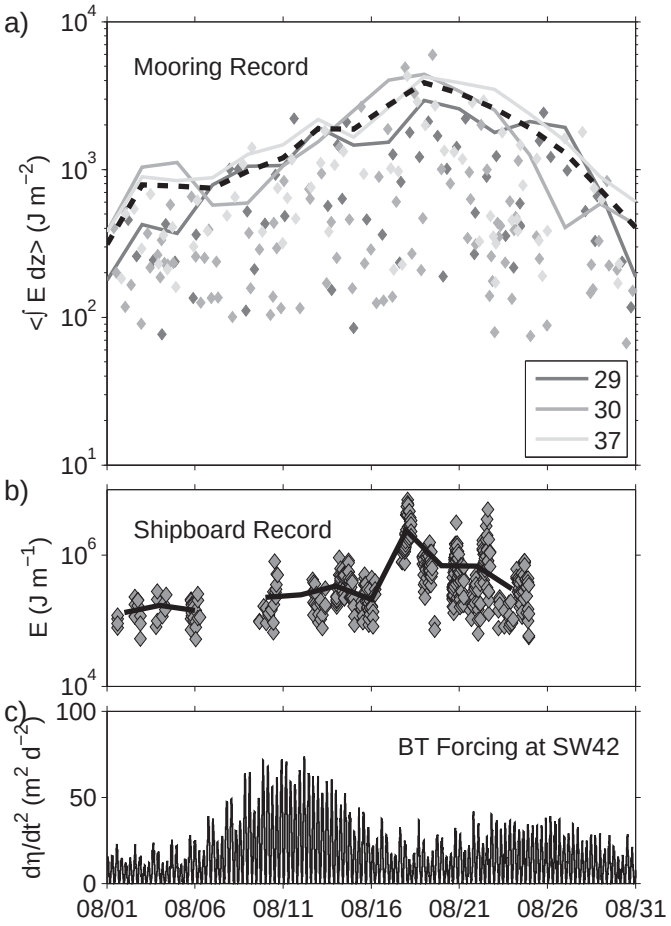


FIGURE 5.6: a) Daily average of the mean depth-integrated NLIW energy calculated at three across shelf moorings, b) shipboard estimated of total wave energy, c) barotropic forcing at the shelf break. Diamonds represent individual wave estimates, and lines are the two-day averages. The black dashed line in a) is the average of all mooring data.

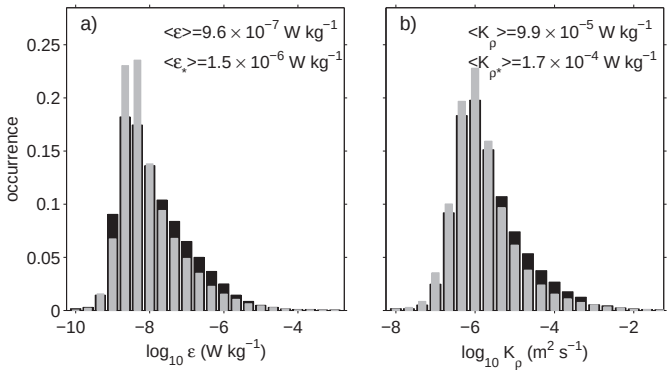


FIGURE 5.7: Histogram of a) $\epsilon$ and b) $K_\rho$ from 10-40 m. Grey bars correspond to waves observed prior to 16 August 2006 and black bars show values for waves observed between 16-25 August 2006. Average values for the first time period are approximately 40% of those in the second time period (denoted with a star).

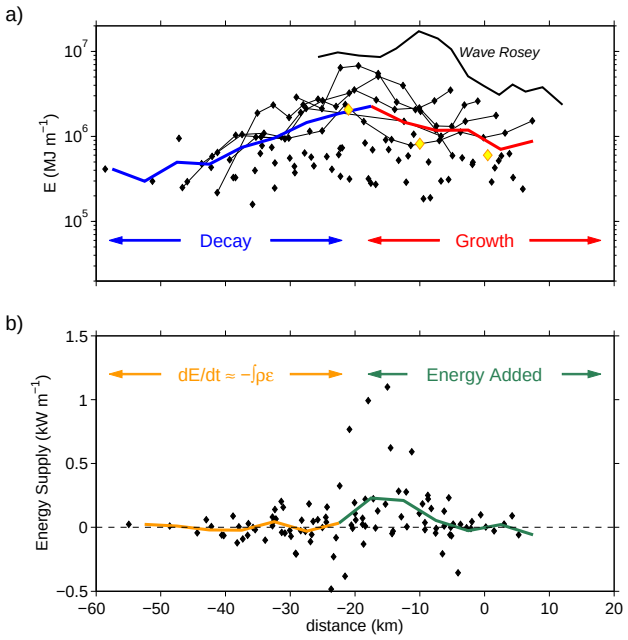


FIGURE 5.8: Energy evolution across the shelf. a) The total energy for the leading three waves are marked with black diamonds, large-amplitude wave site are connected with thin black lines. Energies for *Wave Rosey* are indicated with the thick black line. The thick colored line gives the bin average of energy, excluding *Wave Rosey*. b) Black diamonds represent the value $dE/dt + \int \rho\epsilon$. The shaded line shows the bin average.

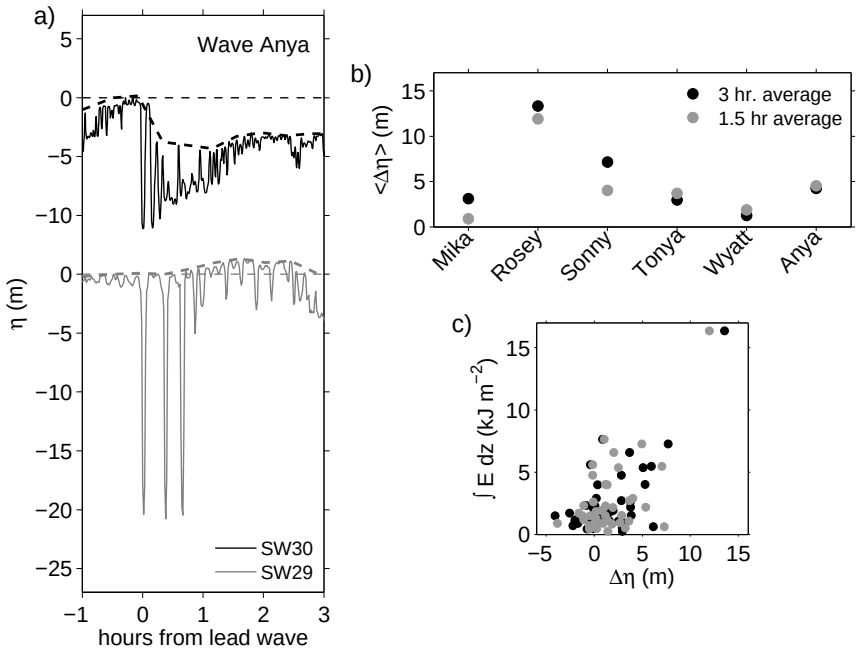


FIGURE 5.9: Wave energy growth from the tidal bore. a) Displacements at SW30 (black and SW29 (grey) for *Anya*. Solid lines show actual displacements, bore estimates are traced with dashed lines. b) Average change in bore displacements between SW29 and SW30 for large amplitude ship-tracked waves. Positive $\Delta\eta$ indicates larger displacements at SW30. c) Wave arrival times at SW30 as compared to the barotropic across-shore M2 velocity at SW40, a shelf-break mooring. All NLIW arrival times between 13-25 August 2006 are shown, and the 6 ship-tracked waves listed in panel b) are highlighted by dark grey diamonds. d) The maximum depth integrated energy at SW29 as a function of $\Delta\eta$ for all wave groups (as observed from mooring records) tracked between SW30 and SW29.

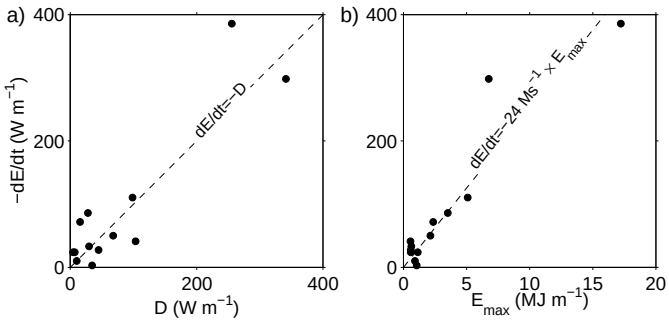


FIGURE 5.10: The average energy loss per unit time compared to a) the average dissipative loss and b) maximum $E$ for ship-tracked wave groups that exhibited decay.

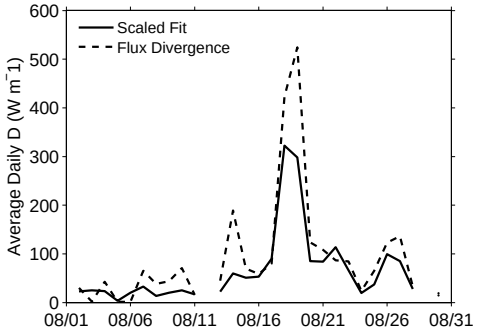


FIGURE 5.11: Estimates of average dissipative loss in the waves as calculated for the scaled fit (solid) and NLIW flux divergence (dashed).

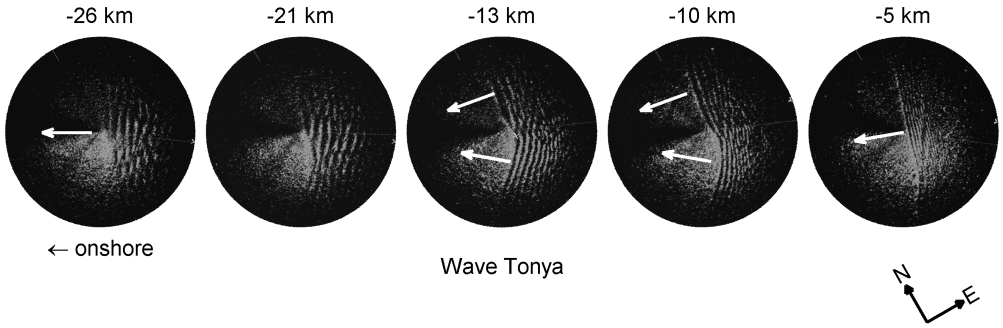


FIGURE 5.12: Series of ship radar images for *Wave Tonya*. Distances along the wave path are indicated above each figure. Wave vectors calculated from images are shown in white. The wave groups are propagating from right to left.

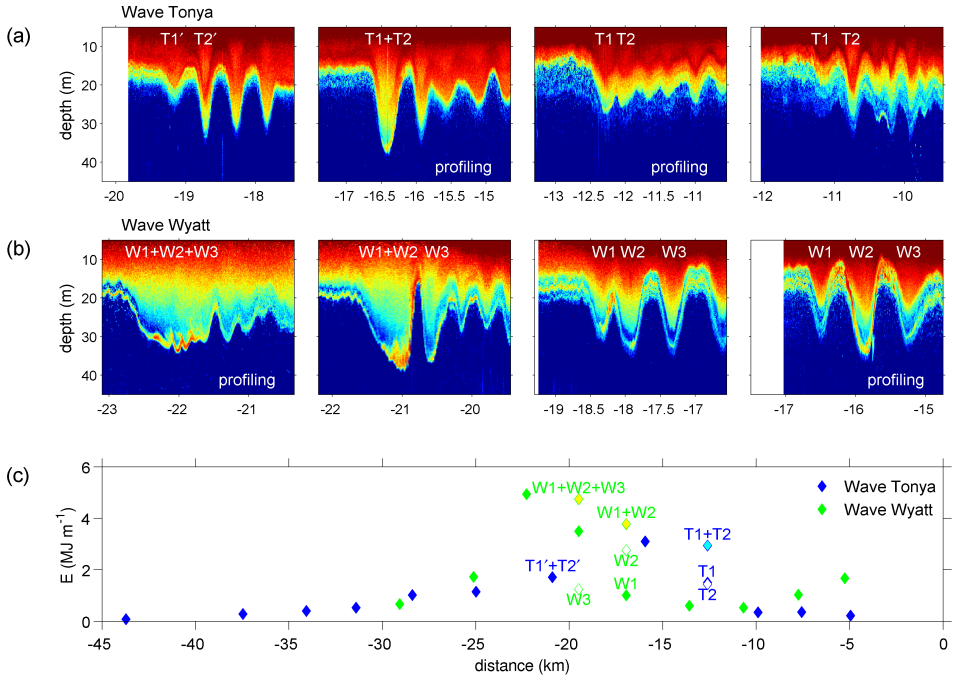


FIGURE 5.13: Sequence of acoustic backscatter transects of a) *Wave Tonya* and b) *Wave Wyatt* showing the hypothesized interactions. Transects accompanied by shipboard profiling are indicated in lower right of backscatter images. c) $E$ of the leading wave for *Tonya* (solid blue) and *Wyatt* (solid green). $E$ in the second waves (open diamonds) and the combined $E$ of the first and second waves (blue/cyan and green/yellow diamonds) are shown at locations just prior to wave interactions. Wave labels are centered either above or below the corresponding markers. Since both *Tonya* and *Wyatt* were profiled through at -16.5 km, markers have been shifted offshore/onshore by 1 km for *Tonya*/*Wyatt* for clarity.

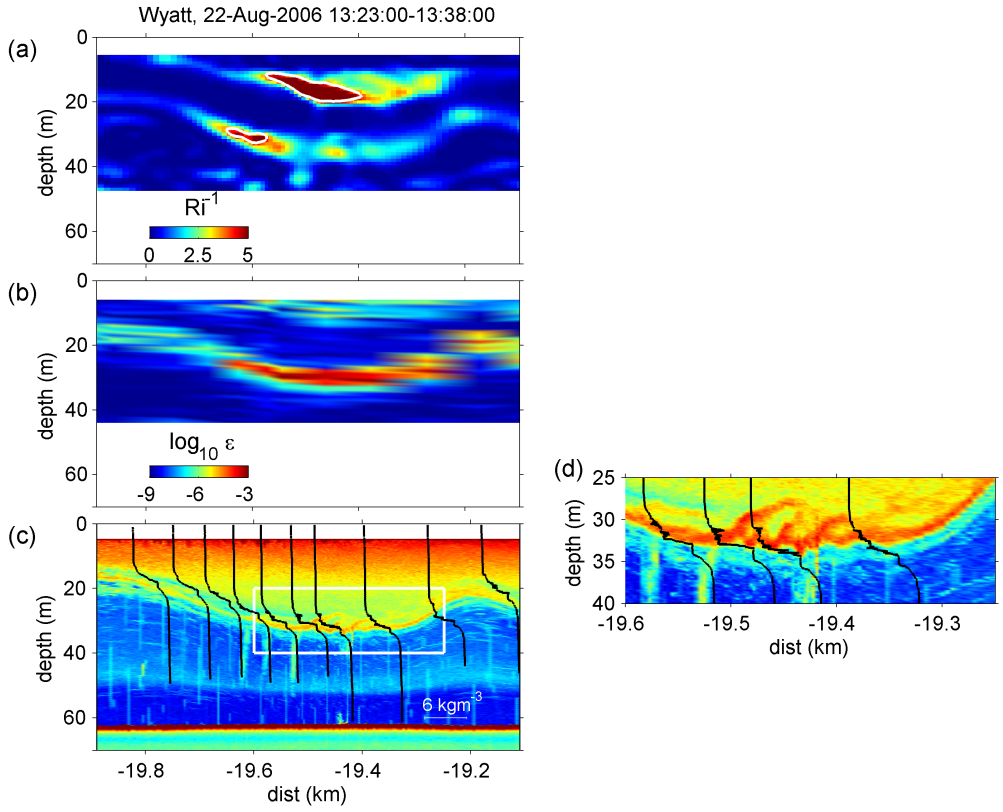


FIGURE 5.14: Turbulent mixing in *Wyatt*. a) Inverse Richardson Number ($\mathrm{Ri}^{-1}$). White contours define $\mathrm{Ri}^{-1} = 4$. b) Turbulent Dissipation ($log_{10}\epsilon$). c) High resolution density profiles ($O$(cm)) are overlaid in black on the the acoustic backscatter image of lead wave. Overturns are evident through the latter portion of the wave.

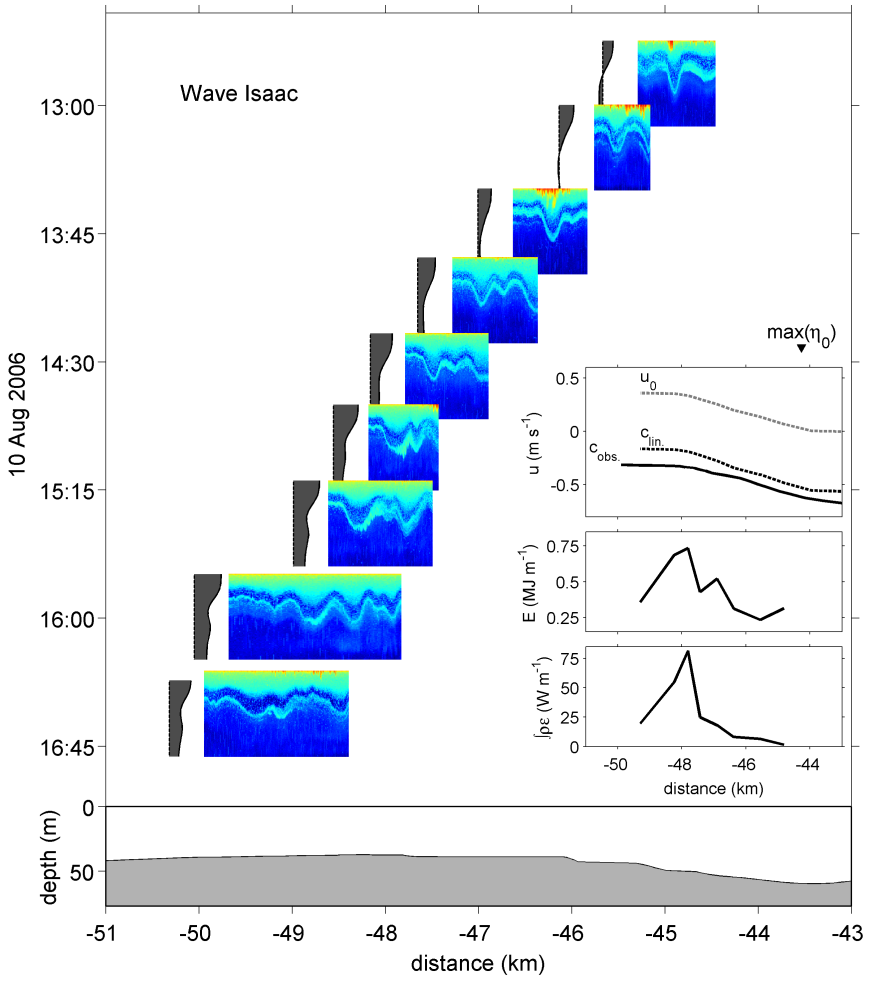


FIGURE 5.15: Acoustic backscatter sequence of *Wave Isaac* as it encounters a topographic bump. Grey patches to the left of backscatter panels show background velocity profiles ahead of the wave. Top inset panel shows the the observed wave speed (solid black line), linear wave speed (dashed black line), and the depth average of $u_0$ (grey dashed line). Positive values are directed offshore. The triangle at top indicates the time of peak tidal elevation, $\eta_0$. The middle inset shows the total energy integrated over 750 m from the leading edge of the first wave, and the bottom inset shows the total dissipative loss integrated over the same distance. The bottom topography is shown in the lower panel.

# 6 CONCLUSIONS

## 6.1 Summary of Results

A defining attribute of the NLIW field on the New Jersey shelf during the Shallow Water 2006 experiment was its variability. A period of approximately six days (17-22 August 2006) distinguished itself from the rest of the month by 1) larger amplitude, more energetic waves and 2) wave arrival times that were more closely tied to the barotropic forcing. In contrast, the remainder of the month was characterized by smaller amplitude waves, whose average energy content was an order of magnitude less. Additionally, during most of the month, waves appeared intermittently with both the number of packets and their arrival times at a given location varying per semidiurnal tidal cycle.

The time period of large NLIWs occurred during neap barotropic conditions, but when the shoreward baroclinic energy was elevated. The difference may be attributed to a shift in the mesoscale stratification at the slope, coincident with the onset of southerly winds. Near-inertial waves were a dominate contributor to the internal motions on the shelf, and apparently regulated wave formation during the six-day period, as larger (smaller) wave packets developed inshore when the surface near-inertial velocity was directed against (with) the semidiurnal tide near the slope. This effect might have been the result of increased (decreased) wave nonlinearity through the background shear field induced by near-inertial waves on the outer shelf.

The observed NLIWs were characterized by large horizontal velocities, large displacements, and elevated mixing near the pycnocline. Thus, the waves impacted the local environment through mass transport and enhancement of turbulent fluxes. One wave group, *Rosey*, that was highly nonlinear and amplitude-limited was capable of transporting mass on the order of 10 km across the shelf. Estimates of heat

flux in the waves were approximately ten times larger than the average background heat flux at the pycnocline, and contributed as much as 50 % of the total heat flux across the shelf during SW06. This difference was primarily attributed to larger values of turbulent diffusivity in the waves as opposed to enhanced vertical temperature gradients; and hence the result can be extended to nutrients and other tracers whose vertical distributions are controlled by the pycnocline. Thus, the waves influence not only thermal properties of shelf water, but may directly impact the biota, by providing a significant contribution to the nutrient supply.

While most of the observed waves were mode-1 in structure, mode-2 wave trains were also observed. Energy analysis for a ship-tracked, mode-2 group and the inability to track individual packets long distances through the mooring array suggest that these waves are short-lived in the dynamic coastal environment. Compared to mode-1 wave groups the propagation distance and decay time scale were much smaller (a few hours/kilometers compared to tens of hours/kilometers). The ship-tracked wave group was an order of magnitude smaller than the mode-1 waves energetically, and it lost energy rapidly to both turbulent dissipation at the mixed layer and radiation of a short, mode-1 wave tail. Estimates of dissipative loss were comparable to those of the larger-amplitude mode-1 waves, indicating that mode-2 waves may be an important contributor to vertical mixing, especially considering that the waves are centered at the pycnocline.

In contrast, mode-1 waves were tracked large distances across the shelf capturing the entire life-cycle, from formation through to shoaling. Of special interest were observations of polarity reversal, from depression to elevation waves, of three different wave groups. As the initially symmetric lead wave approached the fluids critical point, defined by the zero-crossing of the KdV coefficient of nonlinearity, the leading edge accelerated. An asymmetry then developed as the front face of the leading wave flattened, and at the same time the trailing face remained steep.

This trend continued as the wave propagated further inshore until the front face was unidentifiable and a near-bottom elevation wave emerged. Even though the observed waves were highly nonlinear, the location of the observed transition point agreed with that predicted using weakly nonlinear theory.

NLIWs were the dominant energy source of higher-frequency ($\sim 0.2$ min$^{-1}$) motions on the New Jersey shelf. The wave energy grew across the outer shelf, reaching maximum values 40 km inshore of the shelf break. Growth was thought to occur at the expense of potential energy from the bore-like component of the internal tide, and in general wave groups with larger-amplitude density offsets had larger energy inshore. After the period of growth, wave packets lost energy to turbulent mixing, mainly through dissipation in the mixed layer. On a per wave basis, a direct relationship between wave energy and dissipation was not established. However, the average dissipative loss in the region of decay scaled with the maximum wave energy. A decay time of approximately 12 hours was estimated from the scaling, which agrees well with the observed life-span inshore of the growth region. In addition, to these long-term trends, rapid energy exchanges occurred as a result of wave interactions and topographic blocking. The outcome of these events was increased turbulent mixing likely related to shear instability.

## 6.2 Limitations of Analysis and Future Directions

In this thesis, motions are assumed to be primarily two-dimensional, and refraction and three-dimensional spreading have been neglected. Satellite imagery show a NLIW field that is variable in both the across- and along-shore directions. Furthermore, two environmental moorings located in the along-shore branch of the array (only 10 km northeast of SW30), recorded much lower NLIW energies throughout the experiment. The complex geometry of the shelf region, and in particular the

presence of a large canyon just south of the study site, result in a strong along-shore energy flux directed northward. Due to the steep slope, refraction likely plays a role in leaking at least some of this energy onto the shelf. Smaller canyons farther north might also serve as generation regions, possibly creating three-dimensional interference patterns that could account for the reduced energy observed at northern moorings. It is even possible that the smaller-amplitude waves observed at certain times, could in reality have been on the periphery of packets with maximum amplitudes located farther south. Future work should attempt to better quantify the effects associated with 3-dimensional spreading and interference, refraction at the shelf break, and multiple generation sites.

Much of this analysis could be refined further with the aid of numerical simulations. For example, a more detailed analysis of the effect of the near-inertial shear on the generation of NLIW packets could be implemented using a higher-order KdV-type model. Modeling efforts could also help explain the sudden appearance of the short, mode-1 tail for *Jasmine* and the formation of the mode-2 wave groups. In particular, a study detailing the effects of complex background shear with multiple inflection points would be of interest. Also, modeling could provide a better understanding of the physics controlling *Isaac's* interaction with the topographic bump. Numerical efforts could help clarify these specific questions regarding individual wave evolution, and more general questions applicable to the NLIW field in general, such as why wave formation occurs so sporadically on the NJ shelf.

## Bibliography

Akylas, T., and R. Grimshaw, 1992: Solitary internal waves with oscillatory tails. *J. Fluid Mech.*, **242**, 279–298.

Akylas, T. R., R. H. J. Grimshaw, S. R. Clarke, and A. Tabaei, 2007: Reflecting tidal wave beams and local generation of solitary waves in the ocean thermocline. *J. Fluid Mech.*, **593**, 297–313.

Alpers, W., 1985: Theory of radar imaging internal waves. *Nature*, **314**, 245–247.

Apel, J., H. Byrne, J. Proni, and R. Charnell, 1975: Observations of oceanic internal and surface waves from the Earth Resources Technology Satellite. *J. Geophys. Res.*, **80**, 865–881.

Apel, J. R., M. Badiey, C.-S. Chiu, S. Finette, R. Headrick, J. Kemp, J. F. Lynch, A. Newhall, M. H. Orr, B. H. Pasewark, D. Tielbuerger, A. Turgut, K. von der Heydt, and S. Wolf, 1997: An overview of the 1995 SWARM shallow-water internal wave acoustic scattering experiment. *J. Oceanic Engin.*, **22**, 465–500.

Apel, J. R., J. R. Holbrook, A. K. Liu, and J. J. Tsai, 1985: The Sulu Sea Internal Soliton Experiment. *J. Phys. Ocean.*, **15**, 1625–1651.

Bogucki, D., T. Dickey, and L. G. Redekopp, 1997: Sediment resuspension and mixing by resonantly generated internal solitary waves. *J. Phys. Ocean.*, **27**, 1181–1196.

Bogucki, D., L. G. Redekopp, and J. Barth, 2005: Internal solitary waves in the Coastal Mixing and Optics 1996 experiment: modal structure and resuspension. *J. Geophys. Res.*, **110**, doi:10.1029/2003JC002253, C02024.

Bourgault, D., M. D. Blokhina, R. Mirshak, and D. E. Kelley, 2007: Evolution of a shoaling internal solitary wavetrain. *Geophys. Res. Let.*, **34**, 3601–+.

Boyd, J. P., 1990: A numerical calculation of a weakly non-local solitary wave: the $\phi^4$ breather. *Nonlinearity*, **3**, 177–179.

Chang, M.-H., R.-C. Lein, T. Y. Tang, E. A. D'Asaro, and Y. J. Yang, 2006: Energy flux of nonlinear internal waves in northern South China Sea. *Geophys. Res. Let.*, **33**, doi:doi:10.1029/2005GL025196.

Chapman, D., J. Barth, R. Beardsley, and R. Fairbanks, 1986: On the continuity of mean flow between the Scotian Shelf and the Middle Atlantic Bight. *J. Phys. Ocean.*, **16**, 758–772.

Chereskin, T. K., 1983: Generation of internal waves in massachusetts bay. *J. Geophys. Res.*, **88**, 2649–2661.

Choi, W., and R. Camassa, 1999: Fully nonlinear internal waves in a two-fluid system. *J. Fluid Mech.*, **396**, 1–36.

Colosi, J. A., R. C. Beardsley, J. F. Lynch, G. Gawarkiewicz, C.-S. Chiu, and A. Scotti, 2001: Observations of nonlinear internal waves on the outer New England continental shelf during the summer Shelfbreak Primer study. *J. Geophys. Res.*, **106**, 9587–9601.

Davis, R. E., and A. Acrivos, 1967: Solitary internal waves in deep water. *J. Fluid Mech.*, **29**, 593–607.

Dorrestein, R., 1979: On the vertical buoyancy flux below the sea surface as induced by atmospheric factors. *J. Phys. Ocean.*, **9**, 229–231.

Drazin, P. G., 1984: *Solitons*. Cambridge University Press, second edition, 40–67 pp.

Duda, T. F., J. F. Lynch, J. D. Irish, R. C. Beardsley, S. R. Ramp, C.-S. Chiu, T. Y. Tang, and Y.-J. Yang, 2004: Internal tide and nonlinear internal wave behavior at the continental slope in the northern South China Sea. *IEEE J. Oceanic Engin.*, **29**, 1105–1130.

Egbert, G. D., A. Bennett, and M. Foreman, 1994: Topex/poseidon tides estimated using a global inverse model. *J. Geophys. Res.*, **99**, 24821–24852.

Egbert, G. D., and R. D. Ray, 2000: Significant dissipation of tidal energy in the deep ocean inferred from satellite altimeter data. *Nature*, **405**, 775–778.

Farmer, D. M., and L. Armi, 1999: The generation and trapping of internal solitary waves over topography. *Science*, **283**, 188–190.

Fratantoni, P., R. Pickart, D. Torres, and A. Scotti, 2001: Mean structure and dynamics of the shelfbreak jet in the Middle Atlantic Bight during Fall and Winter. *J. Phys. Ocean.*, **31**, 2135–2156.

Gasparovic, R., J. Apel, and E. Kasischke, 1988: An overview of the SAR Internal Wave Signature Experiment. *J. Geophys. Res.*, **93**, 12304–12316.

Gerkema, T., 2001: Internal and interfacial tides: Beam scattering and local generation of solitary waves. *J. Marine Res.*, **59**, 227–255.

Grimshaw, R., 1981: A second-order theory for solitary waves in deep fluids. *Phys. Fluids*, **24**, 1611–1618.

— 1985: Evolution equations for weakly nonlinear, long internal waves in a rotating fluid. *Studies in Applied Mathematics*, **73**, 1–33.

— 2002: *Environmental Stratified Flows, Internal Solitary Waves*, volume 3 of *Topics in Environmental Fluid Mechanics*. Springer US, doi:10.1007/b100815, 1–27 pp.

Grimshaw, R., E. Pelinovsky, T. Talipova, and A. Kurkin, 2004: Simulation of the transformation of internal solitary waves on oceanic shelves. *J. Phys. Ocean.*, **34**, 2774–2791.

Haury, L. R., M. G. Briscoe, and M. H. Orr, 1979: Tidally generated internal wave packets in Massachusetts Bay. *Nature*, **278**, 312–317.

Hebert, D., 1998: The available potential energy of an isolated feature. *J. Geophys. Res.*, **93**, 556–564.

Helfrich, K. R., and W. K. Melville, 1986: On long nonlinear internal waves over slope-shelf topography. *J. Fluid Mech.*, **167**, 285–308.

— 2006: Long nonlinear internal waves. *Annual Rev. Fluid Mech.*, **38**, 395–425.

Helfrich, K. R., W. K. Melville, and J. W. Miles, 1984: On interfacial solitary waves over slowly varying topography. *J. Fluid Mech.*, **149**, 305–317.

Henyey, F. S., and A. Hoering, 1997: Energetics of borelike internal waves. *J. Geophys. Res.*, **102**, 3323–3330.

Hibiya, T., 1988: The generation of internal waves by tidal flow over Stellwagen Bank. *J. Geophys. Res.*, **93**, 533–542.

Holloway, P. E., 1987: Internal hydraulic jumps and solitons at a shelf break region on the Australian North West shelf. *J. Geophys. Res.*, **92**, doi:10.1029/JC092iC05p05405, 5405–5416.

Holloway, P. E., E. Pelinovsky, T. Talipova, and B. Barnes, 1997: A nonlinear model of internal tide transformation on the Australian North West shelf. *J. Phys. Ocean.*, **27**, 871–896.

Houghton, R., and J. Marra, 1983: Physical/biological structure and exchange across the thermohaline shelf/slope front in the new york bight. *J. Geophys. Res.*, **88**, 4467–4481.

Hunter, J. K., and J.-M. Vanden-Broeck, 1983: Solitary and periodic gravity–capillary waves of finite amplitude. *jfm*, **134**, doi:10.1017/S0022112083003316, 205–219.

Hüttemann, H., and K. Hutter, 2001: Baroclinic solitary water waves in a two-layer system with diffuse interface. *Exper. in Fluids*, **30**, 317–326.

Inall, M. E., T. P. Rippeth, and T. J. Sherwin, 2000: Impact of nonlinear waves on the dissipation of the internal tidal energy at a shelf break. *J. Geophys. Res.*, **105**, 8687–8705.

Jackson, C. R., 2004: *An Atlas of Internal Solitary-like Waves and their Properties*. Global Ocean Associates, www.internalwaveatlas.com, second edition.

Jeans, D. R. G., and T. J. Sherwin, 2001: The variability of strongly non-linear solitary internal waves observed during an upwelling season on the Portuguese shelf. *Cont. Shelf Res.*, **21**, doi:10.1016/S0278-4343(01)00026-7, 1855–1878.

Kelly, S. M., J. D. Nash, and E. Kunze, 2009: Internal tide energy over topography. *J. Geophys. Res.*, submitted.

Klymak, J. M., and J. N. Moum, 2003: Internal solitary waves of elevation advancing on a shoaling shelf. *Geophys. Res. Let.*, **30**, 2045–2048.

Kropfli, R., and S. Clifford, 1996: The Coastal Ocean Probing Experiment: further studies of air-sea interactions with remote and in-situ sensors. *Geoscience and Remote Sensing Symposium, 1996. IGARSS '96. 'Remote Sensing for a Sustainable Future.', International*, **3**, 1739–1741.

Kundu, P. K., and I. M. Cohen, 2004: *Fluid Mechanics*. Elsevier Academic Press, third edition, 484–486 pp.

Lamb, K. G., 1997: Particle transport by nonbreaking internal solitary waves. *J. Geophys. Res.*, **102**, 18,641–18,660.

— 2002: A numerical investigation of solitary internal waves with trapped cores form via shoaling. *J. Fluid Mech.*, **451**, 109–144.

— 2003: Shoaling solitary internal waves: on a criterion for the formation of waves with trapped cores. *J. Fluid Mech.*, **478**, 81–100.

— 2007: Energy and pseudoenergy flux in the internal wave field generated by tidal flow over topography. *Cont. Shelf Res.*, **27**, 1208–1232.

Lamb, K. G., and V. T. Nguyen, 2009: Energy flux in internal solitary waves with an application to reflectance. *J. Phys. Ocean.*, **39**, 559–580.

Lamb, K. G., and B. Wang, 1998: flows and flat solitary waves for a continuously stratified fluid. *Phys. Fluids*, **10**, 2061–2079.

Lee, C.-Y., and R. C. Beardsley, 1974: The generation of long nonlinear internal waves in a weakly stratified shear flow. *J. Geophys. Res.*, **79**, 453–462.

Linder, C. A., and G. Gawarkiewicz, 1998: A climatology of the shelfbreak front in the Middle Atlantic Bight. *J. Geophys. Res.*, **103**, 18405–18423.

Liu, A. K., Y. S. Chang, M.-K. Hsu, and N. K. Liang, 1998: Evolution of nonlinear internal waves in the East and South China Seas. *J. Geophys. Res.*, **103**, 7995–8008.

Liu, A. K., Y. Zhao, T. Y. Tang, and S. R. Ramp, 2004: Model-data assimilatioin of internal waves in ASIAEX 2001. *IEEE J. Oceanic Engin.*, **29**, 1144–1156.

Long, R. R., 1953: Some aspects of the flow of stratified fluids: I. A theoretical investigation. *Tellus*, **5**, 42–58.

MacKinnon, J. A., and M. C. Gregg, 2003: Mixing on the late-summer New England shelf – solibores, shear and stratification. *J. Phys. Ocean.*, **33**, 1476–1492.

Maxworthy, T., 1980: On the formation of nonlinear internal waves from the gravitational collapse of mixed regions in two and three dimensions. *J. Fluid Mech.*, **96**, 47–64.

Mehta, A., B. Sutherland, and P. Kyba, 2002: Interfacial gravity currents II: Wave excitation. *Phys. Fluids*, **14**, 3558–3569.

Moody, J., and B. Butman, 1984: American continental shelf, bulletin 1611. *U.S. Geological Society*.

Moum, J., J. Klymak, J. Nash, A. Perlin, and W. Smyth, 2007a: Energy transport in nonlinear internal waves: Experimental determination. *J. Phys. Ocean.*, **37**, 1968–1988.

Moum, J. N., D. M. Farmer, E. L. Shroyer, W. D. Smyth, and L. Armi, 2007b: Dissipative losses in nonlinear internal waves propagating across the continental shelf. *J. Phys. Ocean.*, **37**, 1989–1995.

Moum, J. N., D. M. Farmer, W. D. Smyth, L. Armi, and S. Vagle, 2003: Structure and generation of turbulence at interfaces strained by internal solitary waves propagating shoreward over the continental shelf. *J. Phys. Ocean.*, **33**, 2093–2112.

Moum, J. N., M. C. Gregg, R. C. Lien, and M. E. Carr, 1995: Comparison of turbulence kinetic energy dissipation rate estimates from two ocean microstructure profilers. *J. Atmos. Ocean. Tech.*, **12**, 346–366.

Moum, J. N., and J. D. Nash, 2008: Seafloor pressure measurements of nonlinear internal waves. *J. Phys. Ocean.*, **38**, 481–491.

Moum, J. N., and W. D. Smyth, 2006: The pressure disturbance of a nonlinear internal wave train. *J. Fluid Mech.*, **558**, 153–177.

Nash, J. D., M. H. Alford, and E. Kunze, 2005: On estimating internal wave energy fluxes in the ocean. *J. Atmos. Ocean. Tech.*, **22**, 1551–1570.

Nash, J. D., and J. N. Moum, 2005: River plumes as a source of large-amplitude internal waves in the coastal ocean. *Nature*, **437**, 400–403.

Nash, J. D., E. Shroyer, J. Moum, T. Duda, H. Graber, J. Irish, and J. Lynch, 2009: Mesoscale influences on the generation of the internal tide and nonlinear internal waves over new jerseys continental shelf, in preparation.

New, A. L., and R. D. Pingree, 1990: Large-amplitude internal soliton packets in the central Bay of Biscay. *Deep Sea Res.*, **37**, 513–524.

— 1992: Local generation of internal soliton packets in the central Bay of Biscay. *Deep Sea Res.*, **39**, 1521–1534.

Orr, M. H., and P. C. Mignerey, 2003: Nonlinear internal waves in the South China Sea: Observation of the conversion of depression internal waves to elevation waves. *J. Geophys. Res.*, **108**, doi:10.1029/2001JC001163, 3064–3079.

Osborn, T. R., 1980: Estimates of the local rate of vertical diffusion from dissipation measurements. *J. Phys. Ocean.*, **10**, 83–89.

Osborne, A. R., and T. L. Burch, 1980: Internal solitons in the Adaman Sea. *Science*, **208**, 451–460.

Ostrovsky, L. A., and J. Grue, 2003: Evolution equations for strongly nonlinear internal waves. *Phys. Fluids*, **15**, 2934–2948.

Pelinovskiy, E. N., Y. A. Stepanyants, and T. G. Talipova, 1994: Simulation of nonlinear internal wave propagation in horizontally inhomogeneous ocean. *Atmospheric and Oceanic Physics*, **30**, 77–83.

Perry, R., and G. Schimke, 1965: Large amplitude internal waves observed off the northwest coast of Sumatra. *J. Geophys. Res.*, **70**, 2319–2324.

Pineda, J., 1991: Predictable upwelling and the shoreward transport of planktonic larvae by internal tidal bores. *Science*, **253**, 548–549.

Ramp, S. R., T.-Y. Tang, T. F. Duda, J. F. Lynch, A. K. Liu, C.-S. Chiu, F. Bahr, H.-R. Kim, and Y. J. Yang, 2004: Internal solitons in the northern South China Sea part i: sources and deep water propagation. *IEEE J. Oceanic Engin.*, **29**, 1157–1181.

Sandstrom, H., and J. A. Elliott, 1984: Internal tide and solitons on the Scotian Shelf: A nutrient pump at work. *J. Geophys. Res.*, **89**, 6415–6426.

Sandstrom, H., and N. S. Oakey, 1994: Dissipation of internal tides and solitary waves. *J. Phys. Ocean.*, **25**, 604–614.

Scotti, A., R. Beardsley, and B. Butman, 2006: On the interpretation of energy and energy fluxes of nonlinear internal waves: and example from Massachusetts Bay. *J. Fluid Mech.*, **561**, 103–112.

— 2007: Generation and propagation of nonlinear internal waves in Massachusetts Bay. *J. Geophys. Res.*, **112**, doi:10.1029/2007JC004313.

Scotti, A., and J. Pineda, 2004: Observation of very large and steep internal waves of elevation near the Massachusetts coast. *Geophys. Res. Let.*, **31**.

Shanks, A. L., and W. G. Wright, 1987: Internal-wave-mediated shoreward transport of cyprids, megalopae, and gammarids and correlated longshore differences in the settling rate of intertidal barnacles. *J. Exper. Mar. Biol. Ecol.*, **114**, 1–13.

Shepherd, T., 1993: A unified theory of available potential energy. *Atmos.–Ocean*, **31**, 1–26.

Shroyer, E., J. Moum, and J. Nash, 2009a: Energy transformation and dissipation in the evolving NLIW field over New Jersey's continental shelf, in preparation.

— 2009b: Mode-2 waves on the continental shelf: ephemeral components of the nonlinear internal wave field. *Geophys. Res. Let.*, submitted.

— 2009c: Nonlinear internal waves over New Jersey's continental shelf, in preparation.

— 2009d: Observations of polarity reversal in shoaling nonlinear internal waves. *J. Phys. Ocean.*, **39**, 691–701.

Small, J., 2003: Refraction and shoaling of nonlinear internal waves at the Malin shelf break. *J. Phys. Ocean.*, **33**, 2657–2674.

Small, J., T. C. Sawyer, and J. C. Scott, 1999: The evolution of an internal bore at the Malin shelf break. *Ann. Geophys.*, **17**, 547–565.

Smyth, N. F., and P. E. Holloway, 1988: Hydraulic jump and undular bore form on a shelf break. *J. Phys. Ocean.*, **18**, 947–962.

Stanton, T. P., and L. A. Ostrovsky, 1998: Observations of highly nonlinear internal solitons over the continental shelf. *Geophys. Res. Let.*, **25**, 26952698.

Stastna, M., and K. Lamb, 2002: Large fully nonlinear internal solitary waves: The effect of background current. *Phys. Fluids*, **14**, 2987–2999.

Stastna, M., and W. Peltier, 2005: On the resonant generation of large-amplitude internal solitary waves and solitary-like waves. *J. Fluid Mech.*, **543**, 267–292.

Stepanyants, L. A. O. Y. A., 1989: Do internal solitons exist in the ocean? *Reviews of Geophysics*, **27**, 293–310.

Tang, D. J., and Coauthors, 2007: Shallow Water '06. *Oceanography*, **20**.

Tang, D. J., J. N. Moum, J. F. Lynch, P. Abbot, R. Chapman, P. Dahl, T. Duda, G. Gawarkiewicz, S. Glenn, J. A. Goff, H. Graber, J. Kemp, A. Maffei, J. Nash, and A. Newhall, 2007: Shallow Water '06. *Oceanography*, **20**.

Tung, K.-K., T. F. Chan, and T. Kubota, 1982: Large amplitude internal waves of permanent form. *Studies in Applied Mathematics*, **66**, 1–44.

Turkington, B., A. Eydeland, and S. Wang, 1991: A computational method for solitary internal waves in a continuously stratified fluid. *Studies in Applied Mathematics*, **85**, 93–127.

Vanden-Broeck, J., and R. E. L. Turner, 1992: Long periodic internal waves. *Phys. Fluids*, **4**, 1929–1935.

Vlasenko, V., and K. Hutter, 2001: Generation of second mode solitary waves by the interaction of a first mode soliton with a sill. *Nonlinear Processes in Geophysics*, **8**, 223–239.

— 2002: Numerical experiments on the breaking of solitary internal waves over a slope-shelf topography. *J. Phys. Ocean.*, **32**, 1779–1793.

Vlasenko, V., and N. Stashchuk, 2007: Three-dimensional shoaling of large-amplitude internal waves. *J. Geophys. Res.*, **112**, doi:10.1029/2007JC004107.

Williams, G. P., and R. J. Wilson, 1988: The stability and genesis of rossby vortices. *J. Atmos. Sci.*, **45**, 207–241.

Winters, K., P. Lombard, J. Riley, and E. D'Asaro, 1995: Available potential energy and mixing in density-stratified fluids. *J. Fluid Mech.*, **289**, 115–128.

Zhao, Z., V. Klemas, Q. Zheng, and X. Yan, 2003: Satellite observation of internal solitary waves converting polarity. *Geophys. Res. Let.*, **30**, doi:10.1029/2003GL018286.

Zheng, Q., R. D. Susanto, C.-R. Ho, Y. T. Song, and Q. Xu, 2007: Statistical and dynamical analyses of generation mechanisms of solitary internal waves in the northern South China Sea. *J. Geophys. Res.*, **112**, doi:10.1029/2006JC003551, 3021–+.

## Appendix: The Coefficients of the eKdV Equation

The eKdV equation with spatially variable coefficients may be written as

$$\frac{\partial \eta}{\partial t}+\left(c+\alpha\eta+\alpha_1\eta^2\right)\frac{\partial \eta}{\partial x}+\beta\frac{\partial^3\eta}{\partial x^3}+\frac{c}{2Q}\frac{dQ}{dx}\eta=0.$$

Here, the coefficients governing nonlinearity ($\alpha$ and $\alpha_1$) and dispersion ($\beta$) depend upon the vertical structure function and the linear phase speed, both of which are solved for via the Taylor-Goldstein equation (Eq. 1.2). Explicitly, these coefficients are as follows:

$$\alpha = I^{-1}\int_0^H (c-u)^2\phi^2 dz,$$

$$\begin{aligned}\alpha_1 \;=\; I^{-1}\int_0^H \Bigg\{ & \alpha(c-u)\frac{d\phi}{dz}\left(5\frac{d\phi}{dz}^2-4\frac{dT}{dz}\right)-\alpha^2\frac{d\phi}{dz}^2+ \\ & 3\left((c-u)^2\frac{d\phi}{dz}^2\left(3\frac{dT}{dz}-2\frac{d\phi}{dz}^2\right)\right)\Bigg\}dz, \text{ and}\end{aligned}$$

$$\beta = 3I^{-1}\int_0^H (c-u)^2(d\phi/dz)^3 dz,$$

where

$$I = 2\int_0^H (c-u)(d\phi/dz)^2 dz.$$

Note that the coefficient of quadratic nonlinearity depends upon $T$, a higher order correction to the vertical structure function given by

$$\frac{d}{dz}\left[(c-u)^2\frac{dT}{dz}\right]+N^2T=-\alpha\frac{d}{dz}\left[(c-u)\frac{d\phi}{dz}\right]+\frac{3}{2}\frac{d}{dz}\left[(c-u)^2\left(\frac{d\phi}{dz}\right)^2\right].$$

The above is solved with homogeneous boundary conditions ($T(H)=T(0)=0$). Normalization is required since the solution is an arbitrary multiple of $\phi$, and the

additional condition that $T$ be zero at the location of maximum $\phi$ is imposed. The factor $Q$ accounts for slowly varying background conditions and is defined as

$$Q = \left(c^2 I\right)\left(c_0^2 I_0\right)^{-1}.$$

Introducing two new variables, $s = \int_0^x \frac{dx}{c(x)} - t$ and $\zeta = \eta\sqrt{Q(x)}$, transforms the eKdV equation to

$$c\frac{\partial \zeta}{\partial x} + \left(\frac{\alpha}{c\sqrt{Q}}\zeta + \frac{\alpha_1}{cQ}\zeta^2\right)\frac{\partial \zeta}{\partial s} + \frac{\beta}{c^3}\frac{\partial^3 \zeta}{\partial s^3} = 0.$$

This form is then easily solved via numerical integration. In section 2.5 the modelled equation is simplified further by neglecting the quadratic-nonlinear term.